CHAPTER 1

INTRODUCTION

1.1 Introduction

Water is the priceless natural source in the world, covering above 71 % surface of the earth. The availability of pure water is the most important concern for existence of the mankind and animals. This is because the water bodies, like oceans, rivers, canals and lakes are continuously polluted by the humans. As a result, it has a strong impact on human health. Approximately 1.2 billion people, almost one-fifth of the world's population, are facing physical water scarcity (Qu et al., 2013). 88% of the 4 billion annual diarrhea cases are due to the drinking unsafe water and poor sanitation. Each year, around 1.8 million people die because of diarrhea from all over the world (Kamali & Khodaparast, 2015).

Water is the most important constituent for process completion in various industries such as textile, paper and pulp, and paints. The textile industry is one of the largest consumers of dye stuff along with many other additives. During the common pretreatment, a large percentage of the synthetic dyes and additives make their way into the waste stream. This waste stream from the textile industries carries a huge quantity of synthetic dyes as well as different additives such as phenol etc.

which was inserted during the dyeing process (Chan et al., 2011). These contaminants in the wastewater are generally stable to the light, heat and oxidizing agents, and their direct release into the water bodies causes problems for the humans as well as wildlife.

One of the challenges of achieving water security is ensuring that the wastewater treatment meets the specific quality standards. To accomplish this, undesired contaminants must be removed from the wastewater until a certain limit. Over the years, many treatment techniques have been developed and utilized towards the aqueous organic pollutants degradation. Synthetic dyes and phenol are the most common organic pollutants existing in the wastewater stream of textile industries. Many studies suggested that these organic pollutants are highly toxic, carcinogenic, genotoxic, mutagenic and teratogenic (Wang et al., 2015). Upon their direct contact with the human's body they can cause skin allergies, asthma or, in severe cases, may lead to hormonal changes or some permanent injuries (Motahari et al., 2014; Priac et al., 2017).

Different treatment technologies such as biological, physical and chemical processes have been currently utilized for the elimination of these organic pollutants. Unfortunately, these conventional treatment technologies do not show good removal efficiency towards industrial wastewater. Recently, advanced oxidation processes (AOPs) have gained credit as a promising future treatment process, attributed to their ability to completely remove almost all the organic pollutants into harmless and simple products (carbon dioxide and water). These treatment processes consist of UV/H_2O_2, direct ozonolysis and photocatalysis (Carra et al., 2016; Oturan & Aaron, 2014; Prieto-Rodríguez et al., 2013). Among all these processes photocatalysis is the most promising process because of its capability to eliminate the organic pollutants by the light irradiation of semiconductor photocatalyst.

1.2 Heterogeneous Photocatalysis for wastewater purification

Heterogeneous photocatalysis, a subpart of AOP processes is regarded as the most important technique due to the high capability to degrade various organic pollutants even at low concentration (Borges et al., 2016). When a semiconductor photocatalyst was exposed by photon energy, the electron from the valance band (VB) would promote and shifted in the conduction band (CB), generating the equal number of electron-hole ($e^{-}-h^{+}$) pairs. These $e^{-}-h^{+}$ pairs will react with water and oxygen molecules to generate highly active short life oxygen containing intermediates, for example superoxide anion ($\bullet O_2^{-}$) and hydroxyl ($\bullet OH$) radicals (Asghar et al., 2015; Mehrjouei et al., 2015). These intermediate radicals are extremely active reagents, which take part in the degradation reaction. Heterogeneous photocatalysis technique has various benefits (Bethi et al., 2016; Muruganandham et al., 2014), such as:

(1) A wide range of pollutants present in the liquid and gas phase can be entirely mineralized.

(2) The photocatalysts are chemically stable, inert, nonhazardous, obtainable at low cost and reusable.

(3) A photocatalytic reaction can happen because of the light irradiation on the photocatalyst surface without introducing any new chemicals.

(4) Heterogeneous photocatalysis is also known as a green process, as the end products are environmentally harmless.

Titanium dioxide (TiO_2) is the most commonly researched semiconductor against the degradation of organic contaminants (Borges et al., 2016). Nonetheless, the photodegradation performance of TiO_2 is restricted to the ultra-violet (UV) light, as the TiO_2 has a higher band gap (3.2 eV), which only consist of 4–5% of the solar system, while 44% of the visible light is open for utilizing (Zhang et al. 2015). Hence, development of novel semiconductor photocatalysts with smaller energy band is very important. Bismuth ferrite (BFO) with a rhombohedral perovskite structure is a new visible light driven photocatalyst has recently attracted considerable attraction because of its narrow energy band gap (2.0–2.5 eV), high chemical stability, nontoxicity, excellent ferroelectric and ferromagnetic properties (Hao et al., 2014; Lam et al., 2017). In addition to potential electronic and magnetic applications, semiconductor BFO also has a great potential to be utilized as a visible light photocatalyst (Bharathkumar et al., 2015; Li et al., 2016). However, in bulk BFO, the activity is still limited because of the fast $e^{-}-h^{+}$ pairs recombination and lower *CB* band edge position (Humayun et al., 2016). Thus, many researchers are working on the BFO-based photocatalysts for the efficient photogenerated $e^{-}-h^{+}$ pairs separation.

1.3 Problem statement

In the past few decades, the deterioration of environmental pollution has forced people to pay more attention to environmental protection as well as remediation (Wang et al. 2015). Especially for the water pollution, more and more toxic organic compounds were detected in river and lake waters, which were ordinarily discharged from textile and other chemical industries (Oller et al., 2011; Sun et al., 2018). Because of the low biodegradability, many kinds of persistent toxic pollutants could be accumulated in the environment, making it more hurtful to human health and the ecological environment (Boukhatem et al., 2017; Zhang et al., 2014; Rasalingam et al., 2019). As main constituents of numerous industrial chemicals, malachite green (MG) dye and phenol usually could be detected in wastewater discharged from various factories. Because of the high toxicity, these compounds consistently have been regarded as priority pollutants by the Environmental Protection Agency (EPA) (Boruah et al., 2017; Saputra et al., 2013). It was reported that MG dye and phenol were toxic to human organs or tissues even at low concentration, sometimes even causing death for these who were hypersensitive (Mohamed et al., 2016; Elhalil et al., 2016). However, it has always been a great challenge to remove these persistent toxic pollutants from wastewater for eliminating or reducing pollution. Nevertheless, active efforts have been devoted to exploring a more plausible purification method for these contaminants, including but not limited to physical adsorption, chemical oxidation, solvent extraction, membrane filtration, and biological treatment (Yang et al., 2010; Zhang et al., 2015; Jain et al., 2016; Wang et al., 2016). Because of the incomplete removal of contaminants or addition of chemical reagents during treatment, a secondary pollution was ubiquitous in most cases.

Fortunately, the highly efficient semiconductor-based photocatalysis technology may offer a feasible approach, especially for that using photocatalysts driven by visible or solar light could satisfy people on low-cost and no secondary pollution (Miranda-García et al., 2011; Oller et al., 2011; Rizzo et al., 2013). Recently, perovskite BFO has been emerged as one of the utmost auspicious visible light active photocatalyst because of its smaller energy band-gap (2.2-2.7 eV) (Bharathkumar et al., 2015; Fatima et al., 2017), good chemical stability, non-toxic nature, ferroelectric and ferromagnetic characteristics at the room temperature (Lam et al., 2017; Ponraj et al., 2017). However, in bulk BFO the photocatalytic activity is still restricted because of the fast $e^{-}-h^{+}$ pairs recombination and low position of CB (Humayun et al. 2016; Di et al. 2014; Wang et al. 2016). Consequently, many scholars have explored different methods to alter the BFO photocatalyst to reduce the $e^{-}-h^{+}$ pairs recombination rate either by morphological changes, semiconductor coupling or by doping the noble metals on the BFO surface (Li et al. 2013; Wang et al. 2016).

The manipulation of BFO structures is established to be an efficient technique in order to improve the $e^{-}-h^{+}$ pair separation (Liu et al. 2013; Ilic et al. 2015). Hence, distinct BFO structures with numerous morphologies for example nanorods, nanowires, micro cubes and porous thin film with a wide surface area have been successfully synthesized (Cavalcante et al., 2012; Li et al., 2010; Xu et al., 2011). For the first time, in the present research, BFO with coral-like morphology has been synthesized. Coral-like BFO is very helpful for reactant access during the reaction as well as easily separation ability after the reactions.

However, for the coral-like BFO, the photocatalytic activity is still not satisfactory after single modification (1M). Hence, in order to further increase the photocatalytic activity, the double modification (2M) has attracted much attention for the BFO synthesis (Humayun et al. 2016; Wang et al. 2015; Zhang et al. 2015). In this study, the noble metals (NM) such as Pd, Pt and Ag were selected due to their outstanding properties such as an ability to extend light absorption, strong activity in visible light and enhancement in charge carrier separation, which lead to improve the photocatalytic performance. When NM was decorated on the surface of photocatalyst, it was expected that the generated e^{-} in the irradiated semiconductor was readily captured by the NM, which acts as e^- sinks, leaving the h^+ behind on the surface of the semiconductor (Di et al., 2014).

It is a renowned fact that morphology played a vital role in the photocatalytic system. In developing visible light driven noble metals doped BFO photocatalytic system, the photodegradation mechanism is considered to be a vital issue (Yan et al., 2013; Zou et al., 2012). Very few reports are available on noble metal-doped BFO system and all are mainly emphasizing on effective separation of $e^- - h^+$ pairs in BFO using noble metals without any specific morphology of BFO. On the other hand, no report has been seen on noble metal doped BFO with a particular morphology and their application in photocatalysis. Therefore, the current study will focus on the fabrication of highly active NM (Ag, Pd and Pt) doped BFO photocatalysts. Their photocatalytic activity have been evaluated using the visible light degradation of MG dye, phenol and finally on real textile wastewater as well as understanding of the photocatalytic mechanism.

1.4 Research objectives

The current research is focused on developing noble metals doped coral-like BFO nanocomposite for the degradation of MG dye, phenol and real textile wastewater under visible light irradiations. The specific objectives are:

i. To hydrothermally synthesize the noble metals-doped coral-like BFO nanostructures and characterize them using various characterization analyses.
ii. To investigate the photocatalytic performance of noble metal doped coral-like BFO on the degradation of MG and phenol as model pollutant under visible light irradiation.
iii. To elucidate the photodegradation mechanism of synthesized photocatalysts with the help of a radical trapping agents and terephthalic-photoluminescence analyses.
iv. To investigate the kinetic study using L-H kinetic model and the electrical energy consumed during the photocatalytic reaction.
v. To investigate the photocatalytic activity of noble metals-doped BFO towards the degradation of real textile wastewater.

1.5 Research significance

The current study focuses on the novel three dimensional (3D) noble metals-doped BFO photocatalysts synthesis, their characterization, radical scavenger studies as well as kinetic studies towards the photodegradation of industrial wastewater, MG dye and phenol under the visible light irradiation. The wastewater concentration in the solution are also monitored using UV-spectrophotometer and chemical oxygen demand (COD) analyzers. Newly fabricated photocatalysts are investigated through X-ray diffraction (XRD), field emission scanning electron microscopy (FESEM), energy dispersive X-ray (EDX), transmission electron microscope (TEM), X-ray photoelectron spectroscopy (XPS), UV-visible diffuse reflectance spectroscopy (UV-vis DRS), fourier-transform infrared spectroscopy (FTIR), photoluminescence (PL) and magnetic hysteresis (M-H) loop analyses.

The photocatalysts development starts from the synthesis of coral-like BFO using $Bi(NO_3)_3.5H_2O$, $Fe(NO_3)_3.9H_2O$, and urea in dilute aqueous HNO_3 solution using low temperature urea assisted hydrothermal synthesis technique. In the next step, for the first time, different NM such as Ag, Pd and Pt have been doped on the surface of coral-like BFO using a hydrothermal method. These NM have been selected due to their several advantages such as (i) effective charge transfer capability, which can decrease the recombination of $e^{-}-h^{+}$ pairs; (ii) great ability to absorb visible-light, which led an increase in the amount of $e^{-}-h^{+}$ pairs; and (iii) efficient capability to produce a tight heterojunction interface with semiconductors, which facilitates effective transfer of charges at the interface. These NM act effectively for the charge separation in BFO photocatalyst. The effect of different weight percent loadings of NM on the photocatalytic performance of the doped photocatalysts have been investigated. The crystal structure, morphological, optical, physical and magnetic characteristics of the NM-doped BFO nanocomposite were analyzed using XRD, FESEM, EDX, TEM, UV-vis DRS, FTIR, PL and M-H loop analyses. These explicit characteristics have been further connected to the photodegradation of MG dye, Phenol and textile wastewater under visible light irradiation.

In the current study, different process parameters such as effect of light intensity, catalyst dosage, initial pollutant concentration, solution pH, effect of inorganic anions and humic acid have been examined due to their significant influence on the photodegradation reaction. The study of intermediate products formed during the phenol degradation was also performed. To obtain the further insight in the mechanism studies, the role of different highly active radicals for example h^+, H_2O_2, $\bullet OH$ and $\bullet O_2^-$ have been investigated using numerous radical scavengers and terephthalic acid-photoluminescence (TA-PL) tests. To obtain the order of the reaction, rate of the reaction and rate constant of wastewater degradation, a kinetic study has also been performed. Finally, the photocatalytic activity of NM-BFO nanocomposite towards the degradation of real textile wastewater was also executed.

1.6 Organization of the dissertation

This dissertation contains five chapters. Chapter 1 (Introduction) mainly focusses on the environmental problem caused by the industrial wastewater and the possible solution. Additionally, it states different benefits of heterogeneous photocatalysis over traditional treatment techniques. The problem statement, research objectives, along with the research scope, was also debated here.

Chapter 2 (Literature review) states few previously reported relevant information with this project for the development of the photocatalyst. This chapter also focuses on the toxicology effects of synthetic dyes and phenolic compounds. It also present physical, chemical and ferromagnetic properties of BFO and different possible methods to improve its photocatalytic activity.

Chapter 3 (Materials and Methods) explains about the different chemical compounds utilized along with the comprehensive details about the applied research methodology in this research. A step wise explanation of experimental setup for development of photocatalyst, different photocatalyst characterizations and process conditions are defined in this chapter.

Chapter 4 (Results and Discussion) is the core part of the dissertation, which presents, explains, and evaluates the acquired findings in the current research. It consists of different parts such as the synthesis of NM-doped BFO nanocomposite, characterization of NM-doped nanocomposite, and photodegradation of MG dye, phenol and real textile wastewater under visible light irradiation, proposed photodegradation mechanism, different parameter studies, identification of intermediates and kinetic analyses.

Chapter 5 (Conclusions and future recommendations) concludes the present research. A few recommendations for future work were also presented at the end.

CHAPTER 2

LITRATURE REVIEW

2.1 Photocatalysis

The term photocatalysis is stated as “acceleration of a photoreaction in the existence of a photocatalyst” (Wenderich and Mul, 2016). It has been applied since the mid-1970s for the degradation of harmful contaminants from the water and air. In conventional heterogeneous photocatalysis, photoinduced molecular transformation or photochemical process occurs at the photocatalyst surface. This whole procedure could be divided into five different stages: (1) pollutant relocation on the photocatalyst surface, (2) adsorption of pollutants on the photocatalyst surface, (3) adsorbed phase reaction, (4) products desorption and (5) products removal from the surface of photocatalyst (Herrmann, 1999). The steps (1) and (5) are the mass transfer steps, which mainly subjected to the concentration of the reactants/products as well as the particle size and photocatalyst dosage. While step (2), (3) and (4) depend on the reactants/products chemical compatibility with the active sites. Among five stages, one step will act as controlling step so the operational settings can be different in order to attain the optimal activity.

2.1.1 Photocatalysis principle

The main photodegradation reaction happens in the stage (3), where a semiconductor acts as a photocatalytic substrate absorbs energy in the form of photons produces highly reactive radicals which further utilized in pollutants degradation. The photodegradation mechanism on the BFO surface is described by the following equations.

$$\mathrm{BFO} + h\nu \rightarrow \mathrm{BFO}\ (e^-,\ h^+) \tag{2.1}$$

$$\mathrm{BFO}\ (e^-,\ h^+) \rightarrow \mathrm{BFO} + \mathrm{heat/light} \tag{2.2}$$

$$\mathrm{BFO}\ (h^+) + \mathrm{H_2O_{ads}} \rightarrow \mathrm{BFO} + \bullet\mathrm{OH} + \mathrm{H^+} \tag{2.3}$$

$$\mathrm{BFO}\ (h^+) + \mathrm{OH^-}_{\mathrm{ads}} \rightarrow \bullet\mathrm{OH} \tag{2.4}$$

$$\mathrm{BFO}\ (e^-) + \mathrm{O_{2,\ ads}} \rightarrow \bullet\mathrm{O_2}^- \tag{2.5}$$

$$\bullet\mathrm{O_2}^- + \mathrm{H^+} \rightarrow \mathrm{HO_2}\bullet \tag{2.6}$$

$$\mathrm{HO_2}\bullet + \bullet\mathrm{O_2}^- \rightarrow \mathrm{HO_2}^- + \mathrm{O_2} \tag{2.7}$$

$$2\mathrm{HO_2}\bullet \rightarrow \mathrm{H_2O_2} + \mathrm{O_2} \tag{2.8}$$

$$\mathrm{H_2O_2} + \bullet\mathrm{O_2}^- \rightarrow \mathrm{OH^-} + \bullet\mathrm{OH} + \mathrm{O_2} \tag{2.9}$$

$$\mathrm{BFO}\ (e^-) + \mathrm{H_2O_2} \rightarrow \mathrm{OH^-} + \bullet\mathrm{OH} \tag{2.10}$$

$$\mathrm{H_2O_2} + h\nu \rightarrow 2\bullet\mathrm{OH} \tag{2.11}$$

The key part of the interface among the absorbed molecule and photocatalyst is explained in photoreaction equations (2.3)−(2.11). Due to presence of the charge carriers, the photoexcited semiconductor surface is able to attract the e^- acceptors and donors using chemical and electrostatic forces for example hydrogen bonding, van der Waals forces, dipole-dipole interactions and induced dipole-dipole interactions (Sobre et al., 2010).

2.1.1.1 Band gap excitation

When a semiconductor is exposed to the photons of certain wavelength and energy of this photons source is equal or higher than the band gap (E_g) energy (eV) of the semiconductor, e^- would be migrated from the VB to the CB of the semiconductor and h^+ would be left in the VB. The photogenerated charge carrier pair that happens within a semiconductor also acknowledged as an electron-hole ($e^- - h^+$) pairs. The least required irradiated photons energy to produce the $e^- - h^+$ pairs mainly depends on E_g of the semiconductor and it can be estimated by the following equation (Lang et al., 2014).

$$E_g = 1240/\lambda \tag{2.12}$$

where, λ is the photon irradiation wavelength (nm) to produce excitation on the semiconductor surface. The $e^- - h^+$ pairs generation rate is initially directed by the conditions of photons irradiation such as intensity of photons, wavelength of photons and intrinsic characteristics of the semiconductor such as their E_g value, morphology, crystal structure and so on (Ohtani, 2010; Nanakkal and Alexander, 2017; Klubnuan et al., 2016).

After the generation of $e^{-}-h^{+}$ pairs through the light irradiations, several different possible reaction pathways are also presented in Figure 2.1. The formation of $e^{-}-h^{+}$ pairs after the absorption of photons energy equal or greater than the E_g are shown in reaction (1). The surface and bulk properties of a semiconductor have a strong influence on the reactions (2)−(5). Reduction reaction takes place when an e^{-} from the semiconductor is eliminated by an electron acceptor (A) as shown in reaction (2). The oxidation process happened when a free e^{-} transfer from a donor species and combined with a free h^{+} on the surface as mention in reaction (3). When there are no A and D the $e^{-}-h^{+}$ pairs go through fast recombination as shown in reactions (4) and (5). Due to this fast of $e^{-}-h^{+}$ pairs recombination ultimately reduce the photocatalytic activity of semiconductor.

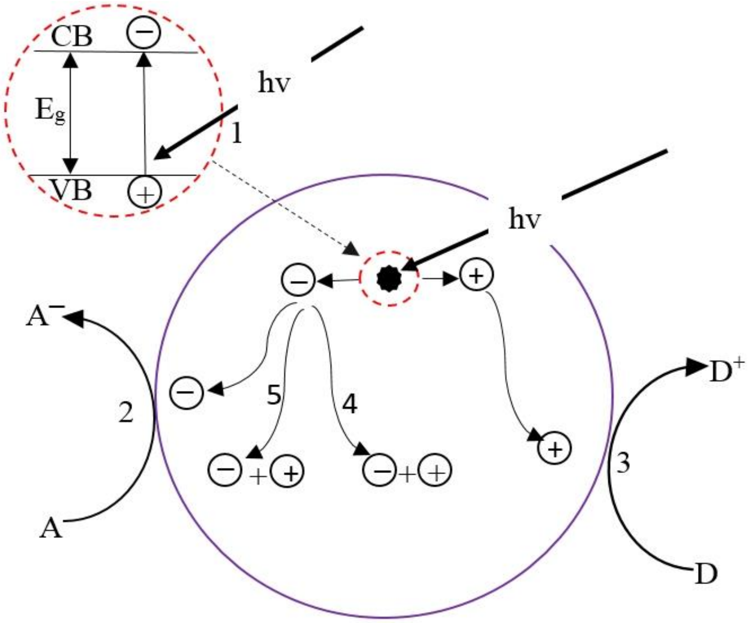

Figure 2.1: Schematic illustration of $e^{-}-h^{+}$ pairs photoexcitation in a semiconductor followed by the redox reactions (Linsebigler et al., 1995).

The E_g energy is the length from the base of *CB* to the top of *VB*. In photocatalysis, the E_g edges knowledge is extremely vital to understand the mechanism of photodegradation. For example, in reduction reactions, the reduction potentials of the selected molecules must be lower than the *CB* edge position of the semiconductor. While, for oxidation reactions, the oxidation potentials of the absorbed molecule should be located comparative to the position of *VB* edge position of the semiconductor. In Figure 2.2, the band edges of many significant semiconductors are presented.

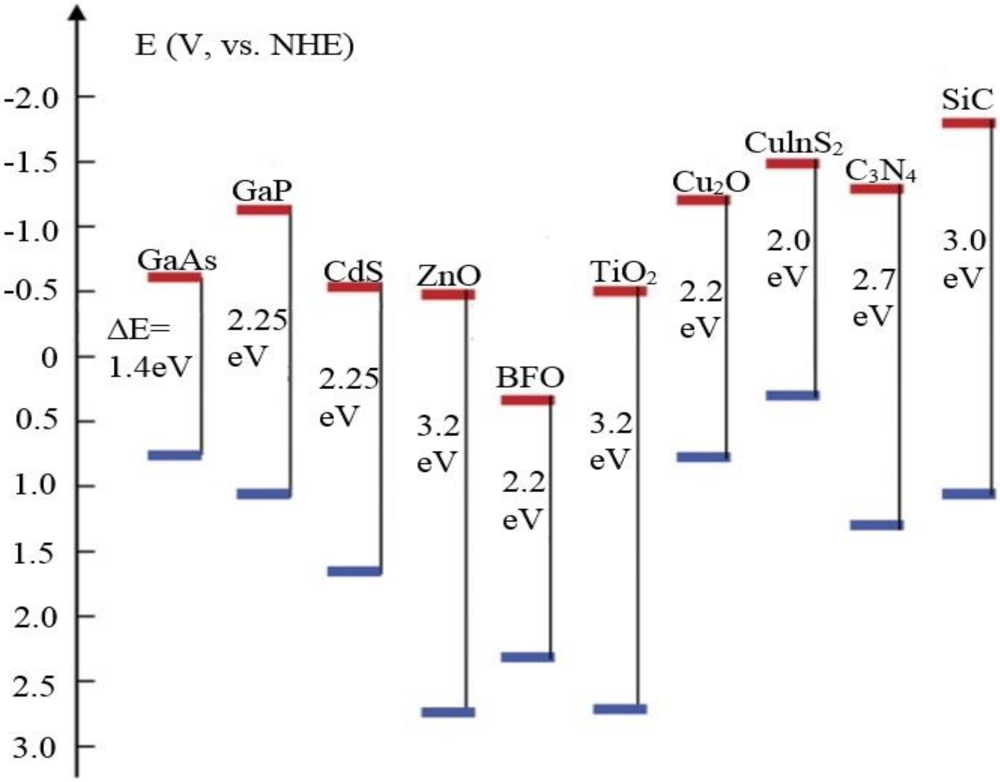

Figure 2.2: Band edge positions and E_g energies for some selective semiconductors (Hui and Zhang, 2014).

2.1.1.2 Electron and hole ($e^{-}-h^{+}$) pair recombination

There is a high risk of $e^{-}-h^{+}$ pairs recombination during the competition of charges transferring to the surface adsorbed species, led to a declined in photodegradation performance. The recombination happens either on the semiconductor surface or volume in the form of light/heat, as displayed in Equation (2.2). When the charge carriers take more time to diffuse on the surface than the $e^{-}-h^{+}$ pairs recombination time, the $e^{-}-h^{+}$ pairs recombination happens itself. The time required for the interfacial migration of e^{-} to the A and the interfacial migration of h^{+} to the D is in a microsecond and ~100 nanoseconds, respectively. However, it is normally believed that the recombination of $e^{-}-h^{+}$ pairs happens in the timeframe of nanosecond and picosecond subjective to the particle size and semiconductor photocatalyst type (Linsebigler et al., 1995).

2.1.1.3 Role of photogenerated $e^{-}-h^{+}$ pairs in photocatalysis

The photoinduced $e^{-}-h^{+}$ pairs in a catalyst must migrate to the particle surface for the interaction with the absorbed species to obtain the higher quantum efficiency. The $e^{-}-h^{+}$ pairs recombination also reduces when the photogenerated e^{-} are transfer to surface (Zhou et al., 2015; Kumar and Rao, 2014; Zhao et al., 2015). These surface transferred e^{-} primarily react with the O_2 to generate $\bullet O_2^{-}$ radical as demonstrate in equation (2.5), which take part in further reactions with hydroperoxyl radical (HO_2•), hydrogen peroxide (H_2O_2) and produced •OH radical (Wang et al., 2015; Bai et al., 2015; Spasiano et al., 2015).

While successful surface migrated photogenerated h^+ can attack the surface absorbed H_2O molecules, and OH^- ions to produce the •OH radicals as shown in Equations (2.3) and (2.4). These generated •OH radicals have very high oxidation capability so they are the mainly responsible for the photodegradation of contaminants (He et al., 2013; Fan et al., 2015a). The •OH radical generation on the surface of semiconductor has been confirmed by a simple TA–PL test using TA as a fluorescent probe. TA has a strong tendency to attack on the produced •OH radicals to form 2-hydroxylterephthalic acid (2HTA). The intensity peak attributed to 2HTA indicating yield of generated •OH radicals (Wang et al., 2015; Zhang et al., 2016; Li et al., 2015; Zhang et al., 2016).

These generated oxidative species during photocatalytic reaction has also been monitored using different radicle scavengers (Pereira et al., 2016; Koltsakidou et al., 2017; Hoong et al., 2016). The photocatalytic reaction decreased because of these radicle scavengers. This decrease in the photodegradation activity was due to the use of scavengers exposed the significance of different reactive oxygen species. Therefore, it is very important to learn the importance of these oxygen species generated by the separated $e^- - h^+$ pairs during the photodegradation process.

2.2 Properties of perovskite $BiFeO_3$

In recent years, BFO is among the most extensively studied multiferroic material because it is the only material which display at the same time magnetic order (Neel Temperature T_N = 370 ^oC) and ferroelectric order (Curie temperature T_C = 830 ^oC) at the room temperature (Han et al., 2015; Yin et al., 2016). BFO with the general formula ABO_3 is a characteristic perovskite compound as shown in the Figure 2.3. In the crystal lattice structure there are two cation sites: in the corner of a unit cell there is a large cation site A (Bi in BFO) and at the center of a unit cell there is a small cation site B (Fe in BFO). At the face of a unit cell the oxygen atoms are present and at the corner oxygen octahedral are linked with the large cation A in the model structure network while the cation B connecting the octahedral sites (Kumar & Kar, 2014; Tanaka & Misono, 2001). The bulk BFO have the rhombohedral distorted perovskite structure in *R3c* space group along with the lattice parameters a = b = 0.558 nm c = 13.9 nm at room temperature as revealed in Figure 2.4 (Gu et al., 2016; Yin et al., 2016).

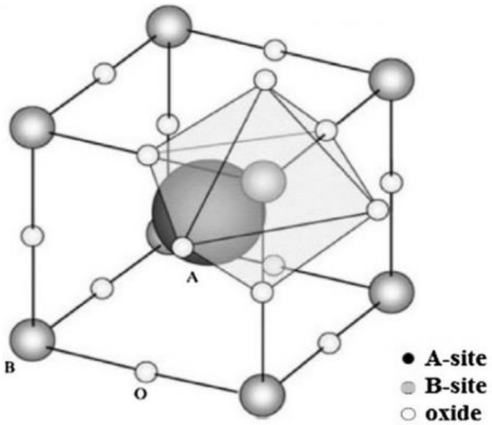

Figure 2.3: Structure of a unit cell of perovskite ABO_3 (Tanaka & Misono, 2001).

The rhombohedral phase was clearly seen in the XRD analysis at the peaks 2θ = 25.1(012), 32.2(104), 32.9(110), 37.8(006), 48.0(202), 53(116), 53.5(122), 56.5(018), 57(214), 57.5(214), 66(208), 67(220), 71(036), 71.5(312), 72(131), 76(128) and 76.5(134) (Yin et al., 2016). When the six unit cell of BFO join together it revealed hexagonal structure ($[001]_{hex}$, $[100]_{hex}$, $[110]_{hex}$ and $[010]_{hex}$ were hexagonal axis as shown in Figure 2.4. The $[111]_c$ was correspond with $[001]_{hex}$ using a single unit cell it revealed a pseudocubic structure in which oxygen ions are filed on the face center.

2016).

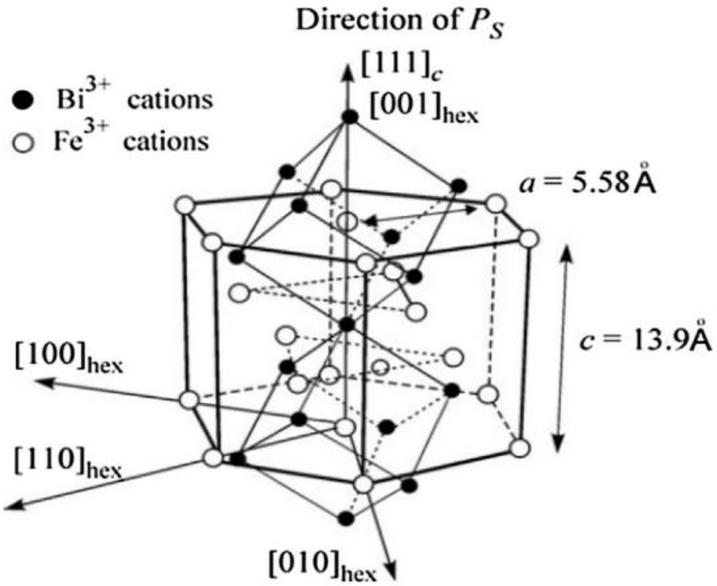

Figure 2.4: BFO structure in terms of hexagonal frame of reference (Zavaliche et al., 2007).

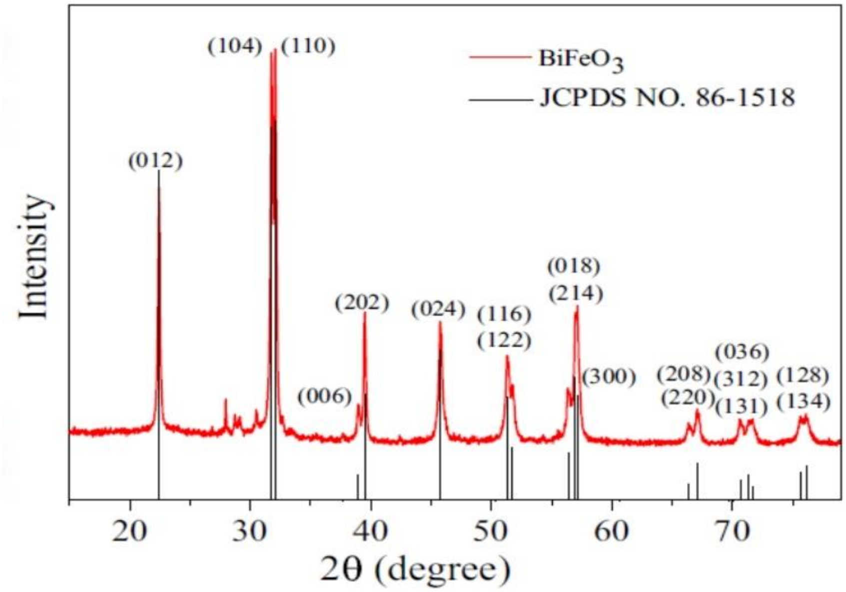

Figure 2.5: XRD pattern of pure BFO with rhombohedral structure (Yin et al., 2016).

Perovskite BFO is the only material which shows simultaneously ferroelectric (at site A) and ferromagnetic (at site B) properties (Gowrishankar et al., 2016). In BFO the origin of ferroelectricity is because of the active $6s^2$ lone pair of e^- in Bi^{3+} ion (A site) while the ferromagnetic properties initiate from the partially filled d orbital in Fe^{3+} ion (Vangaet al., 2015). The displacement of the Bi^{3+} ions comparative to the FeO_6 octahedral give arise to the ferroelectric state with its polarization position beside the c-axis of (i.e., $[111]_c$) rhombohedral and antiferromagnetic ordering along $[111]_c$ was shown in neutron diffraction studies (Singh & Yadav, 2014). The G-type antiferromagnetic order exist in BFO, in which magnetic moments of Fe^{3+} ions aligned ferromagnetic with $[111]_c$ and antiferromagnetic among contiguous [111] as shown in Figure 2.6. (Schwartz, 1997; Zavaliche et al., 2007).

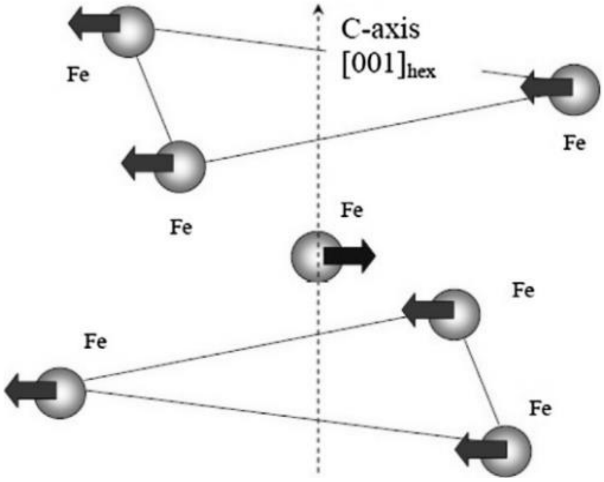

Figure 2.6: G-type antiferromagnetic ordering of the Fe^{3+} magnetic moments in BFO (Schwartz, 1997).

In UV-Vis DRS spectra, the BFO exhibited an absorption edge around 485−560 nm, in visible region confirming to narrow direct E_g energy of about 2.2−2.8 eV at room temperature (Gong et al., 2013; Sati et al., 2014; Han et al., 2015). The band edge in the range of 380−700 nm consist in the visible region, thereby was proposed for their applications in photovoltaic devices such as solar cell, spintronics and sensors (Singh and Yadav, 2014; Liu et al., 2005). BFO has a very high commercial prospective because of its very cheap price, nontoxic, environmental friendly and very easy to recover after photocatalytic reaction (Zaki et al., 2014; Liu et al., 2013; Vanga et al., 2015).

2.2.1 $BiFeO_3$ photocatalytic degradation of organic contaminants

A huge number of highly lethal organic contaminants present in wastewater have been successfully degraded using photocatalysis process. Halogenated hydrocarbons have been easily degraded by BFO photocatalyst in aqueous solution, stoichiometry equation is shown below:

$$C_AH_BCl_C + [A + ((B - 4)/4)]\ O_2 \longrightarrow A\,CO_2 + C\,HCl + ((B - 2)/2]\ H_2O \tag{2.13}$$

Many different other classes of organic pollutants such as dyes, pesticides and aliphatic carboxylic acids can also be degraded using BFO as photocatalysts. Different types of organic pollutants degradations using BFO as photocatalysts are shown in the Table 2.1.

Table 2.1: Examples of numerous organic contaminants elimination via BFO as photocatalyst.

Class of organic	**Example**	**Reference**
Aliphatic aldehyde	Acetaldehyde	(Soltani and Lee, 2016b)
Phenolic compounds	Phenol, Bisphenol A, Phenol Red	(Soltani & Mohammad H. Entezari 2014; Humayun et al., 2016; Dhanalakshmi et al. 2016)
Helophenol	4-chlorophenol	(Q. Zhao et al., 2015)
Volatile organic compounds	Benzene, Toluene	(Soltani & Lee 2016; Kong et al. 2016a)
Dyes	Methyl orange, Rhodamine B, Congo red, Reactive black 5	(Soltani & Entezari 2013; Soltani & Entezari 2013; Li et al. 2016)
Carboxyl group	Oxalic acid	(Yin et al., 2016)
Lignin model pollutants	Guaiacol	(An, Zhang, Zheng, & Wang, 2016)

The complete and efficient degradation of all the organic pollutants in aqueous solution using BFO photocatalysts strongly depends on the formation of strong oxidation species as described in photocatalysis process previously. Nonetheless, during the practical applications of BFO as photocatalysts some drawbacks appeared. The major limitation of BFO as semiconductor photocatalyst was the recombination of photoinduced charge carriers, which restricts the photodegradation efficiency of BFO photocatalyst. This problem was because of the rapid recombination of $e^{-}-h^{+}$ pairs and resulted in the low generation of •OH radicles. As a result, BFO photocatalyst shows lower photodegradation efficiency upon absorption of visible light (Niu et al., 2015; Humayun et al., 2016). Zhang et al., (2016) stated that the lower *CB* band edge position (+0.44 eV vs. NHE) was also one of the major limitations of BFO as a photocatalyst. In the photocatalysis process, the positions of band edge positions are extremely important as it provides information about the generation of reactive oxygen species. Lower band edge position suggests that the BFO is not able to generate the $•O_2^{-}$ radicals. However, it has the potential to generate H_2O_2 molecules, which is also among the reactive oxygen species.

2.3 Improving $BiFeO_3$ photocatalytic activity using morphological modification

Photocatalyst nanostructured materials is a new branch of semiconductors, which gives one of the utmost capacities to improve the photocatalytic performance and competences products in many different industries (Wang et al., 2016; Rezaei et al., 2016). These nanostructures are separated into numerous types such as zero dimensional (0D), one dimensional (1D), two dimensional (2D) and three dimensional (3D). The 3D BFO nanostructures have gained considerable focus because of their different exceptional characteristics and the prospect that they might be utilized in storage density devices, multistate electric devices, spintronics, sensors, solar cell, as well as photocatalysts for organic pollutants present in wastewater and air (Guo et al., 2017; Yan et al., 2013; Zhu et al., 2016). Different kind of 3D BFO nanostructures were synthesized for example cage-like and bones-like structures as shown in figure 2.7.

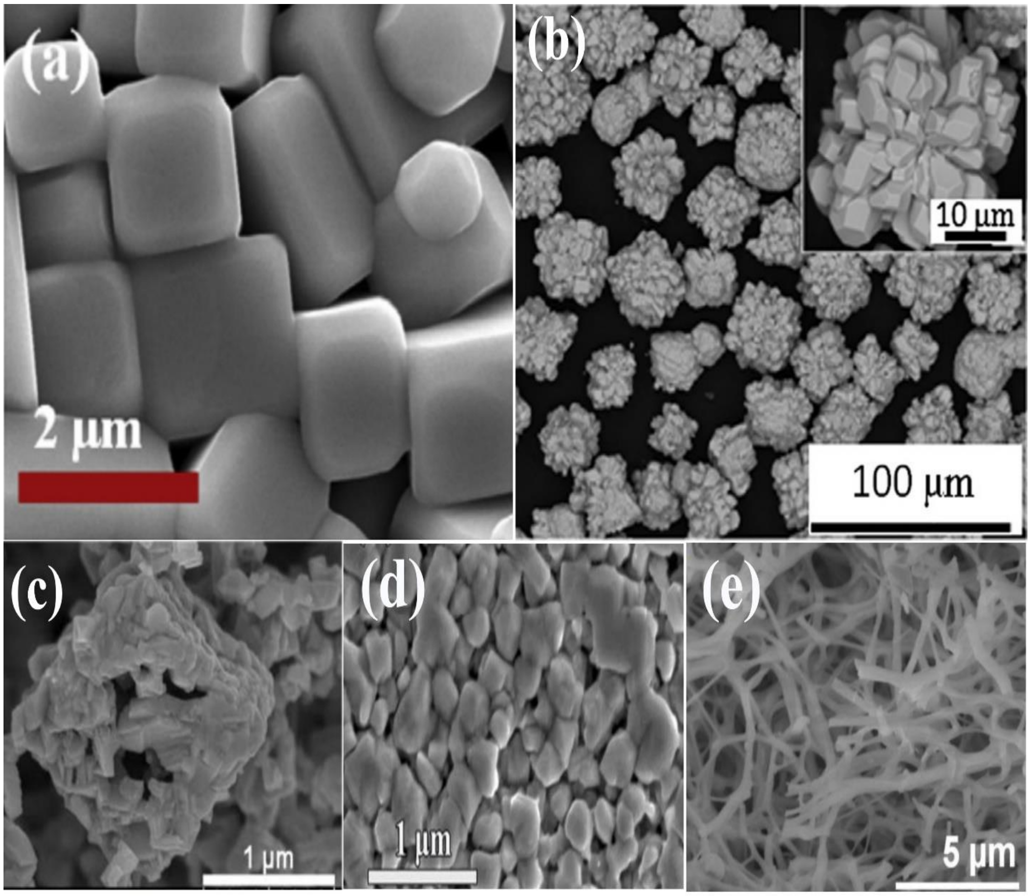

Figure 2.7: BFO 3D structures (a) cube shape (Chauhan et al., 2016), (b) polyhedron-shaped (Pei & Zhang, 2013), (c) cage-like (Dong et al., 2013), (d) thin film of irregular shaped nanoparticles (Tang et al. 2016) and (e) bones-like nanoparticles (Sakar et al., 2016).

The 3D BFO nanostructures have shown great photocatalytic activity. This improvement in the photocatalytic activity was because of their enhanced surface area as compared with the microscale materials, which enhanced their contact area during the photocatalytic reaction. Many researchers also point out many special advantages of these nanostructures over nanoparticles for example improving the light consumption rate and reducing the $e^{-}-h^{+}$ pairs recombination rate (Zhang et al., 2016; Li et al., 2015). In present, research BFO with novel coral-like morphology with improved $e^{-}-h^{+}$ pairs have been synthesized. Coral-like BFO with improved $e^{-}-h^{+}$ pairs was very helpful for reactant access during the reaction.

2.3.1 Synthesis methods of $BiFeO_3$

Pure single phase perovskite BFO have been synthesized using different physical and chemical techniques as reported in literature (An et al., 2013; Gao et al., 2015; Huo et al., 2011; Wang et al., 2013; Xian et al., 2011). Particularly, a great attention has been given to the wet chemical synthesis methods due to the simple procedure, low cost, easy to control and less energy requirement (Liu et al., 2010). A brief summary of BFO synthesis methods is shown in Table 2.2.

Perovskite-type of oxides precursors have been synthesized at high temperature using solid-state reactions (Chen et al., 2007; Kalinin et al., 2002; Thrall et al., 2008; Wang et al., 2013). Equal molar parts of Bi_2O_3 and Fe_2O_3 was typically used to synthesize BFO. Figure 2.8 depicts the phase diagram depending on the Bi_2O_3-Fe_2O_3 system. The phase diagram suggested that the BFO was disconsonant compound, and the phase generation in Bi_2O_3-Fe_2O_3 system could lead to the generation of the contaminations such as $Bi_{25}FeO_{40}$ or $Bi_2Fe_4O_9$ (Palai et al., 2008; Wang et al., 2016b). So for the synthesis of BFO using the conventional solid state reaction method could lead to the different impurities in the BFO at high temperature.

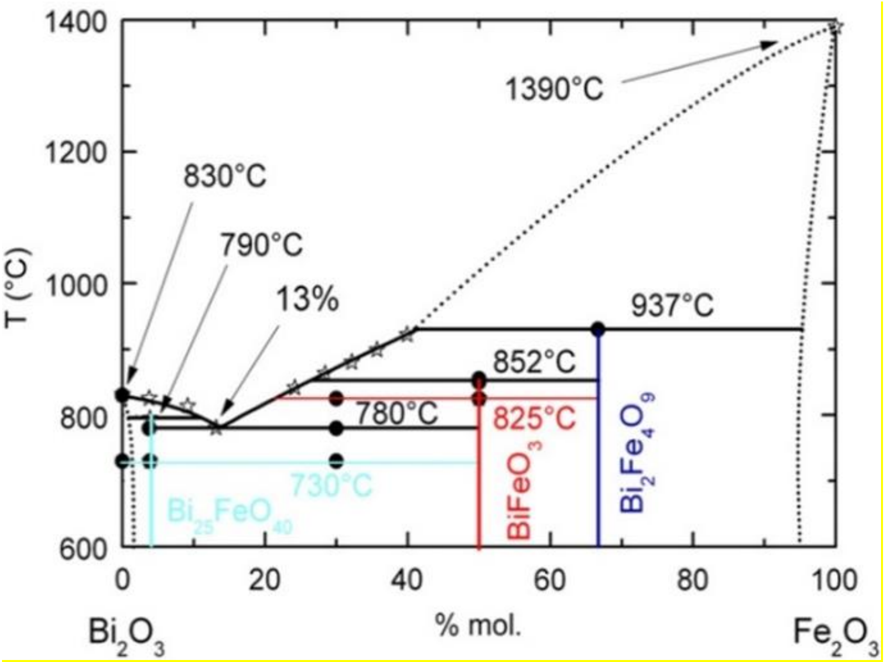

Figure 2.8: Composition phase diagram of BFO (Lu et al., 2017).

Table 2.2: Preparation and different properties of BFO using different synthesis methods.

Synthesis method	**sources**	**Temperature /Time**	**Morphology**	**Surface area (m^2/g)**	**Band gap (eV)**	**Reference**
Hydrothermal	$Bi(NO_3)_3.5H_2O$, $Fe(NO_3)_3.9H_2O$, KOH, PVP	200 °C/5 h	Cubic-shaped	−	1.9	(Gao et al., 2015)
Hydrothermal	$Bi(NO_3)_3.5H_2O$, $Fe(NO_3)_3.9H_2O$, KOH, nitric acid	200 °C/6 h	Irregular agglomerates	4.0	2.4	(Kong et al., 2016)
Hydrothermal	$Bi(NO_3)_3.5H_2O$, $Fe(NO_3)_3.9H_2O$, KOH, PVP, NaOH	200 °C/3 h	Agglomeration shape	3.78	2.2	(Niu et al., 2015)
Hydrothermal	$Bi(NO_3)_3.5H_2O$, $FeCl_3.6H_2O$, acetone, PVP (0.5 g), NaOH (2−4 M)	180 °C/72 h	Cubes-like (2 M NaOH) Plate-like (4 M NaOH)	0.766	−	(Chauhan et al., 2016)
Hydrothermal	$Bi(NO_3)_3.5H_2O$, $FeCl_3.6H_2O$, glycol, ammonia, EDTA, PVP	200 °C/5 h	Honeycomb (EDTA)	12.38	1.97	(Huang et al., 2014)
				3.58	2.06	

			Flower-like (PVP)			
Hydrothermal	$Bi(NO_3)_3.5H_2O$, $Fe(NO_3)_3.9H_2O$, acetone, ammonia, NaOH	180 °C/72 h	Nanocubes	0.874	–	(Dhanalakshmi et al., 2016)
Hydrothermal	$Bi(NO_3)_3.5H_2O$, $Fe(NO_3)_3.9H_2O$, NaOH, acetone, ammonia,	170 °C/24 h	Polyhedron shaped micro-particles	–	2.10	(Hao et al., 2014)
Solvothermal	$Bi(NO_3)_3.5H_2O$, $Fe(NO_3)_3.9H_2O$, glycerol, ethanol, citric acid	160 °C/24 h	Microspheres	15.3	2.1	(Ilić et al., 2015)
Co-precipitation	$Bi(NO_3)_3.5H_2O$, $Fe(NO_3)_3.9H_2O$, acrylamide, EDTA	600 °C/3 h	Nanoparticles	–	2.12	(He et al., 2013)
Co-precipitation	$Bi(NO_3)_3.5H_2O$, $Fe(NO_3)_3.9H_2O$, HNO_3, NaOH	600 °C/2 h	Nanoparticles	–	2.10	(Fatima et al., 2017)

Reverse co-precipitation method	$Bi(NO_3)_3.5H_2O$, $Fe(NO_3)_3.9H_2O$, HNO_3, ammonia,	180 °C/12 h	Spherical particles	–	1.96	(Li et al., 2016)
Sol-gel	$Bi(NO_3)_3.5H_2O$, $Fe(NO_3)_3.9H_2O$, dilute nitric acid, PVP	500 °C/2 h	Oval shaped nanoparticles	–	2.1	(Kuang et al., 2016)
Sol-gel	$Bi(NO_3)_3.5H_2O$, $Fe(NO_3)_3.9H_2O$, tartaric acid, nitric acid	600 °C/2 h	Nanoparticles	–		(Zhang et al., 2012)
Sol-gel	$Bi(NO_3)_3.5H_2O$, $Fe(NO_3)_3.9H_2O$, 2-methoxymethne, nitric acid	600 °C/1 h	Nanowires	–	2.5	(Lotey & Verma, 2014)
Sol-gel	$Bi(NO_3)_3.5H_2O$, $Fe(NO_3)_3.9H_2O$, citric acid, ethylene glycol, HNO_3	500 °C/2 h	Nanoparticles	–	2.35	(Gong et al., 2013)
Sol-gel	$Bi(NO_3)_3.5H_2O$, $Fe(NO_3)_3.9H_2O$, 2-methoxyethanol, citric acid, ethylene glycol, HNO_3	500 °C/2 h	Nanoparticles	–	2.05	(Soltani & Entezari, 2014)

Sol-gel	$Bi(NO_3)_3.5H_2O$, $Fe(NO_3)_3.9H_2O$, 2-methoxyethanol, acetic acid	500 ^{o}C/3 h	Thin film	–	2.28	(Zhang et al., 2015)
Ultrasound	$Bi(NO_3)_3.5H_2O$, $Fe(NO_3)_3.9H_2O$ and ethylene glycol	400-500 ^{o}C/ 0.5 h	Nanoparticles	–	2.17	(Soltani and Entezari, 2013)
Electrospinning	$Bi(NO_3)_3.5H_2O$, $Fe(NO_3)_3.9H_2O$, ethanolamine, glacial acetic acid, PVP, DMF, acetone	550 ^{o}C/2 h	Nanofibers	–	2.19	(Kalinin et al., 2002)
Molten-salt	Bi_2O_3, Fe_2O_3 and NaCl	750 ^{o}C/2 h	Cubic shaped nanoparticles	2.95	2.15	(Palai et al., 2008)
Chemical solution method	$Fe(NO_3)_3.9H_2O$, $Bi(NO_3)_3.5H_2O$, citric acid, ethylene glycol	500-700 ^{o}C/2 h	Nanoparticles	–	2.50	(Singh & Yadav, 2014)
Aerosol spraying	$Bi(NO_3)_3.5H_2O$, $Fe(NO_3)_3.9H_2O$ and glycerol	500 ^{o}C/2 h	Mesoporous hollow spherical	27	2.1	(An et al., 2013)

For pure single phase BFO synthesis wet chemical synthesis methods have gained a lot of attention due to their many advantages over other synthesis methods. Different techniques in this group were co-precipitation (Liu et al., 2010; Xian et al., 2011), sol–gel (Gong et al., 2013), ultrasound (Soltani and Entezari, 2013), hydrothermal (Gao et al., 2015; Wang et al., 2016b), aerosol-spraying (An et al., 2013) and electrospinning (Kalinin et al., 2002). Among all these synthesis methods, hydrothermal synthesis has appeared to be a promising technique to synthesis pure BFO at low temperature (equal to or less than 200 ^{o}C) without any calcination. Low-temperature hydrothermal synthesis is very important for the preparation of pure single phase BFO, due to the low-temperature, it prevents any decomposition in BFO and decreases the impurities formation chances. As the size and shape of the semiconductor material play a vital role in optical, magnetic and electrical properties of semiconductor material so using hydrothermal synthesis method it was probable to control the size and morphology of the material using certain structure-directing agents.

Zou et al., (2012) synthesized three different BFO morphologies using different synthesis methods. Platelet-like BFO was synthesized by hydrothermal synthesis method. Whereas, irregular nanoparticles and microcubes were effectively synthesized via microwave assisted sol-gel synthesis method with the help of citric acid and aqueous ammonia solution respectively. Lotey and Verma, (2014) synthesized BFO nanowires using sol-gel synthesis method. They also studied the calcination effects on the purity of BFO and it was concluded that pure

BFO nanowires were prepared at temperature 550 ^{o}C. Yang et al., (2013) synthesized BFO using hydrothermal synthesis method via KOH as mineralizer (1.5−5 M). The morphologies and phase composition of synthesized products were changed at different concentrations of KOH. At lower KOH concentration $Bi_2Fe_4O_9$ phase was the most dominant phase along with the nanoflakes morphologies. While with the KOH concentration increased from 3.5 M, the morphology was changed from nanoflakes to self-assembled nanostructures along with the few nanoflakes corresponding to the change in the dominant phase from $Bi_2Fe_4O_9$ to $BiFeO_3$. The possible reason for the dominant phase formation of $Bi_2Fe_4O_9$ rather than the $BiFeO_3$ was also explained by them.

2.4 Improving $BiFeO_3$ photocatalytic activity via a co-catalyst loading

As discussed earlier, the fast photogenerated $e^{-}-h^{+}$ pairs recombination and lower *CB* position are the main drawbacks in BFO nanoparticles which leads to the lower photocatalytic activity. To overcome these shortcomings and enhanced the photodegradation activity of BFO, the construction of BFO heterojunctions with other co-catalysts such noble metals doping, coupling with semiconductor metals oxides, metals ion substitutions and fabrication of porous perovskite BFO are widely used (Liu et al., 2017; Zhang et al., 2016; Jia et al., 2017; Subha et al., 2017). Therefore, TiO_2/BFO (Humayun et al., 2016), carbon core/shell nanofibers @ BFO (Liu et al., 2013), alpha (gamma)-Fe_2O_3/BFO (Tseng and Lin 2014), Ag@BFO (Di et al., 2014), Pt/BFO (Niu et al., 2015), La substituted BFO (Dhanalakshmi et al., 2016), Gd/BFO (Guo et al., 2010), Ca substituted BFO (Kumar and Singh, 2016), g-C_3N_4/BFO (Wang et al., 2015; Fan et al., 2015b) and CuO/BFO (Niu et al., 2015) had been successfully synthesized and applied for the degradation of organic contaminants under visible light irradiations.

2.4.1 Noble metal doping

The semiconductor photocatalytic activity generally depends on many factors. In order to obtain good photodegradation activity of a semiconductor the key factor is to enhance the migration of photogenerated $e^{-}-h^{+}$ pairs efficiently. To harvest extra visible light and to improve the separation of $e^{-}-h^{+}$ pairs different NM such as Ag, Au, Pt and Pd has been repeatedly used to doped on the semiconductor photocatalysts which leads to improve their photocatalytic activity (Ozacar, 2016; Ribao et al., 2016; Singhal and Kumar 2017). It is expected that, when NM are doped on semiconductor surface, the photogenerated e^{-} in the *CB* of semiconductor are immediately captured by the noble metals which act as efficient e^{-} sinks, leaving the h^{+} behind on the surface. As a result, amount of photogenerated h^{+} increased on the semiconductor surface which leads to improve the $e^{-}-h^{+}$ pairs separation efficiency as displayed in Figure 2.9. This phenomena is also known as surface plasmon resonance (SPR) (Niu et al., 2015).

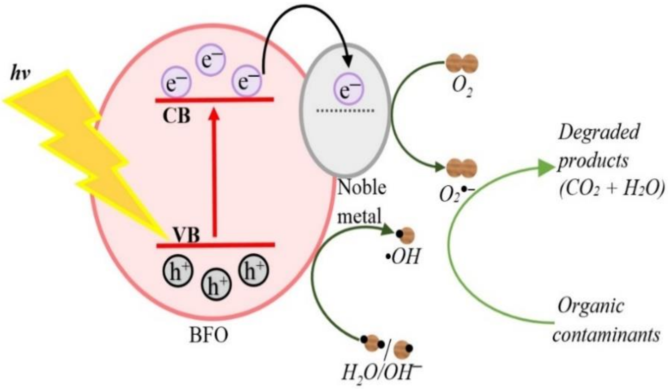

Figure 2.9: Schematic illustration of organic contaminants degradation over NM-doped BFO (Niu et al,. 2015).

When the NM were doped on BFO surface the excited e^- on the CB will be attracted towards the NM because the noble metals have lower fermi levels then BFO and they act as an e^- sink. This stops the $e^- - h^+$ pairs recombination as well as improve the absorption of light properties of the photocatalyst, which leads to the improvement in the photocatalytic efficiency. To increase the quantum efficiency of BFO, different NM such as Pt, Ag and Au have been successfully doped on the surface of BFO (Di et al., 2014; Niu et al., 2015b; Zhang et al., 2015).

Niu et al., (2015) doped Pt on the surface of BFO using impregnation technique and applied for the photodegradation of MO dye. The MO was completely degraded by Pt-BFO after 180 min visible light irradiations. The UV-Vis DRS results showed that the Pt-BFO light absorption capability was good in the visible light region (up to 700 nm). Because of the strong light absorption properties, the photodegradation efficiency of Pt/BFO photocatalyst was improved five times as compared with the pure BFO. M@BFO (M= Au and Ag) were synthesized using sol-gel synthesis method and applied for the photodegradation of RhB dye under the irradiation of visible light. After 240 min visible light irradiation 83%, 77% and 35% RhB were degraded using Au/BFO, Ag/BFO and pure BFO respectively. The noble metals on the BFO surface were described to act as an e^{-} sink, to prolonge the photogenerated charge carriers lifetime and enhance the interfacial charge migration among the noble metals and the BFO and consequently enhanced the photocatalytic performance (Zhang et al., 2015).

2.4.2 Metal ions substitution

Substitution with the metal ions was considered as one of the possible methods to improve the visible light absorption properties of BFO (Huo et al., 2011). In some cases, the substitution of metal ions could also act as e^{-}/h^{+} scavengers, which led to enhance the photogenerated charge carriers lifetime and by substitution decreased the chances of $e^{-}-h^{+}$ pairs recombination (Vanga et al., 2015). Selection of metal ions, preparation methods and operating conditions had a strong impact on the photodegradation performance of metal substituted BFO. Different metal ions such as La (Dhanalakshmi et al., 2016), Gd (Guo et al., 2010), Co (Luo et al., 2013), Nd and Ni (Vanga et al., 2015), Ca and Mn (Pei & Zhang,

2013) have been successfully substituted on BFO photocatalyst and utilized for the visible light degradation of different organic pollutants.

Soltani and Lee, (2016) synthesized Ba substituted BFO (0.5, 1, 2 wt%) through sol-gel synthesis and utilized towards the photodegradation of benzene under visible light irradiations. They found that Ba-substituted BFO had high visible light photocatalytic efficiency than those of the pure BFO on the benzene removal and mineralization. 2 wt% Ba-substituted BFO successfully degraded 97% benzene after 60 min of visible light irradiation, 93% and 82% was the carbon dioxide production rate in COD and TOC, respectively. The higher photodegradation efficiency in the existence of Ba-substituted BFO was credited to effective migration of $e^{-}-h^{+}$ pairs as witnessed in their PL studies. Guo et al., (2010) investigated the activity of Gd-substituted BFO on the photodegradation of RhB under the irradiation of visible light. It was established that Gd-substituted BFO showed enhanced photocatalytic efficiency as compared with the pure BFO. After 240 min of visible light irradiation, almost 95% and 43% RhB was degraded using Gd-substituted BFO and pure BFO, respectively. The reason for improved photodegradation efficiency was that when Gd substituted in the BFO, more surface defects could be formed and enhanced surface area, which was helpful to reduce the $e^{-}-h^{+}$ pairs recombination.

2.4.3 Coupling with semiconductor oxides

The formation of a heterojunction via multicomponent is also an efficient technique, as it helps to extend the light absorption capability as well as reduced the photoinduced $e^{-}-h^{+}$ pairs recombination (Gong et al., 2013a). A heterojunction could be formed by the coupling of a wide E_g semiconductor with the smaller E_g semiconductor material (Singh & Yadav, 2014). The formation of the heterojunction would be helpful to enhance the of $e^{-}-h^{+}$ pairs separation. Various BFO based heterojunctions have been reported in the literature to either improved the light-absorption region or reduce the recombination of $e^{-}-h^{+}$ pairs, for example BFO/TiO_2 (Humayun et al., 2016; Li et al., 2013), Ag/AgCl/BFO (Wang et al., 2016), $(Bi/Fe)_2O_3$/BFO (Kong et al., 2016), CuO/BFO (Niu et al., 2015). Humayun et al., (2016) form a heterojunction between the BFO and TiO_2 through sol-gel synthesis and utilized towards the phenol degradation. After 60 min of light irradiation, the photocatalytic activities were around 30% and 80% for pure BFO and TiO_2/BFO respectively. Such improvement in photodegradation performance was reported because of the effective $e^{-}–h^{+}$ transfer capacity of BFO narrow E_g semiconductor to TiO_2 semiconductor and improved light absorption properties.

Lu et al., (2017) synthesis cubic shaped $SrTiO_3$/BFO photocatalyst and applied for the degradation of RhB. It was observed that photocatalysts E_g values can be easily changed by changing molar ratios between $SrTiO_3$ and BFO. The photocatalytic efficiencies were around 53% and 89% using pure BFO and $SrTiO_3$/BFO respectively, after 240 min of visible light irradiation. This improved efficiency was because of the efficient charge transfer happened among the interface of the heterojunction. Kong et al., (2016) synthesized nanowires shaped heterojunctions among the BFO and $(Bi/Fe)_2O_3$ and applied for the photodegradation of toluene. They observed almost double photocatalytic activity using $(Bi/Fe)_2O_3$/BFO as compared with the pure BFO and this improvement was because of the effective $e^{-}-h^{+}$ pairs separation.

2.5 Photocatalytic reaction parameter

In photodegradation rate of organic containments present in wastewater are strongly affected by different operating parameters such as photocatalyst loading, pH of the solution, initial pollutant concentration and effect of additives. These parameters are important as they affect the photocatalytic processes of the degradation performance of organic contamination in the industrial wastewater. There were limited reports available on BFO, so the following section is mainly reflected the different semiconductor photocatalysts.

2.5.1 Effect of photocatalysts dosage

The dosage of photocatalyst is a vital factor towards the photodegradation of organic contaminants present in wastewater. It was commonly stated that the photocatalytic activity would increase with the rise in the photocatalyst loading until a certain limit (Liu et al., 2013b; Wang et al., 2016; Mahmoodi, 2017). The improvement in the degradation efficiency is because of the enhanced number of actives sites available. At lower photocatalyst loading, the light absorption was the main driving force in the photocatalysis process because of the limited surface area of photocatalyst (Butler et al., 2017; Lamo et al., 2015). However, with increasing in the photocatalyst loading, the quantity of active sites available on the photocatalyst surface also enhanced, which resulted in the improved absorption of photons energy and enhanced dye molecules adsorption on the surface of photocatalyst enhanced the photodegradation efficiency. The photodegradation activity decreased when the photocatalyst loading increased from its optimum value because it produced the light interception by the suspension (Liu et al., 2013; Butler et al., 2017). Sun et al., (2014) reported that the generation of •OH radicals was prevented by the excess amount of photocatalyst, as in photocatalytic system if the amount of primary oxidant decreased it ultimately decrease the photocatalytic activity. Furthermore, increasing the photocatalyst amount beyond the optimum limit may cause the agglomeration of the photocatalyst particles, hence a lot of the active sites became unreachable for photon absorption and decrease the photodegradation performance (Tan et al., 2016).

Nischk et al., (2014) reported the TiO_2 loading effects (0.25−1.0 g/L) on the photodegradation of acid violet 17 (AV-17) under UV light irradiation. When the catalyst dosage was increased, the photodegradation efficiency of AV-17 was initially increased and then decreased. The best amount of TiO_2 was found to be 0.75 g/L. The decrease in the photodegradation efficiency against AV-17 at higher catalyst loading was because of the agglomeration of TiO_2 nanoparticles and scattering of light. Sobana et al., (2015) performed several tests to determine the best dosage of ZnO (0.5 to 3.0 g/L) against the photodegradation of MO dye solution (dye initial concentration = 10 ppm, pH = 6.4) under direct sunlight irradiation. When the ZnO concentration was enhanced from 0.5 to 2.5 g/L the photodegradation performance also improved. Above 2.5 g/L, they witnessed that the light absorption and ZnO surface were the main restrictive factors.

2.5.2 Effect of initial concentration of pollutants

It was a renowned fact that with the increased in the initial concentration of pollutants, the rate of pollutant absorption on the surface of photocatalyst also enhanced. As the photocatalysis was a surface process so the initial pollutant concentration had a strong influence on the degradation process. It is a general perception, as the initial dye concentration improved, the photodegradation performance also increased until a certain limit and beyond that limit further increased in the concentration of dye, the rate of pollutant photodegradation starts decreasing (Mahmoodi, 2017; L. Wang et al., 2016b). As on the surface of the photocatalyst, the degradation reaction mainly happened between the active species and aqueous dye molecules. At the higher initial concentration, the quantity of active sites present on the surface of the photocatalyst decreased because of the competition among dye molecules for the absorption. Since the photocatalyst dosage, light intensity and reaction duration were unchanged so the generated •OH radicals were also constant. Therefore, the limited number of •OH radicals decreased the degradation efficiency at higher dye concentration. Moreover, at higher pollutant concentration light might also be absorbed by the dye molecules instead of the photocatalyst (Sun et al., 2014; Zuo et al., 2013).

Salehi et al., (2017) studied the effects of initial concentration of direct blue (DB) dye ranged between 10−80 mg/L using CuO-ZnO nanoparticles. They observed the decline in the photodegradation activity from 100% to 45% after 120 min UV light irradiation, when the initial DB 71 concentration was enhanced from 10 to 80 mg/L. A decline in the amount of reactive oxidizing species was the main reason for this declined in the photodegradation performance. Yu et al., (2017) examined the effect of MB dye concentration using hydrothermally synthesized rod-shaped g-C_3N_4 photocatalyst. They reported that the degradation performance decrease from 95% to 66% as MB concentration was enhanced from 5 to 40 mg/L. Zheng et al., (2016) witnessed the effect of initial reactive red 120 (RR-120) concentration in the range from 5 to 50 mg/L using Ag-doped AgCl photocatalyst. After 180 min of visible light irradiation, the photodegradation activity and TOC removal were decreased from 95% to 45% and 70 to 25% respectively, as RR-120 concentration was increased. In RR-120 photodegradation •OH radicals were the key reactive species. With the enhanced initial RR-120 concentration led to the decreased photon penetration in the system, which ultimately caused a decreased in the number of •OH radicals generation.

2.5.3 Solution pH

In photocatalysis process the pH can be one of the utmost important parameters, especially in the dyes degradation the understanding of pH effects is extremely problematic task due to its several roles. According to the following reactions it is associated with the ionization state of the photocatalyst surface. Also it has impacts on the products and the reactant dyes.

$$TiOH + H^+ \longrightarrow TiOH^{2+} \tag{2.14}$$

$$TiOH + OH^- \longrightarrow TiO^- + H_2O \tag{2.15}$$

Adsorption of dyes molecules onto the photocatalyst surface was influenced by the change in pH, many researchers reported that the photocatalytic activity have considerable implementations over acidic and basic properties of photocatalysts such as TiO_2, ZnO, g-C_3N_4 etc. For TiO_2 (Degussa P25), it had point of zero charge (pzc) at pH 6.2 (Shetty et al., 2016). Thus, the TiO_2 surface in acidic media ($pH < 6.2$) was positively charged while under the alkaline conditions ($pH > 6.2$) it was negatively charged. Second, when the positive h^+ and hydroxide ion (OH^-) react together it produces •OH radicle. At low pH, the h^+ were consider as the main reactive species, while at natural or higher pH •OH radicles were consider as the predominant species (Das & Srivastava, 2016; Singh et al., 2018). It was reported that the generation of •OH radicles on a photocatalyst were easier in the alkaline conditions, thus it is logical the efficiency of the process was higher under the alkaline conditions (Reza et al., 2015).

High pH was considered favourable for the degradation even when synthetic dyes hinders adsorption on the negatively charged surface (Anirudhan et al., 2016). The negatively charged e^- in the CB plays a crucial role in the photodegradation of dyes at lower pH. Lastly, at lower pH value most of the photocatalysts tend to agglomerate which decrease the available surface area for the dye adsorption leads to the decline in the efficiency (Chanu et al., 2016; Mathubala et al., 2016). Khataee et al., (2015) investigated the solution pH effect on the photodegradation of Acid red 52 over Er/ZnO nanocomposites under visible light irradiations. They stated that the photodegradation rate of Acid red 52 was higher in the acidic conditions. The improvement in the efficiency was because of the presence of two sulphonic groups in Acid red 52, which were strongly attracted towards the positive surface of a photocatalyst in the strongly acidic conditions. Guz et al., (2016) tested the RhB dye photodegradation using various solution pH in the range between pH3−pH13 over g-C_3N_4 under visible light irradiation. The photodegradation was most prominent especially in strongly alkaline conditions (pH = 11). It was due to the higher pH value, the generation of •*OH* radicals were enhanced so, they did take an active part in the dye degradation reaction.

2.5.4 Effects of inorganic species

The existence of inorganic ions in textile wastewater containing dyes contents were common due to the utilization of different inorganic compounds during process completion. The photocatalytic activity might decrease due to the presence of a few cations such as phosphate, copper and iron after a certain concentration limit. One of the main reasons for this decrease in the activity was that these compounds may compete with the dye molecules for the same active site present on the photocatalyst as a result it may deactivate the active site which led to the declined in the photodegradation of dyes molecules. While zinc (Zn), magnesium (Mg) and calcium (Ca) have very small effect on the photocatalytic activities of the synthetic dyes even in their highest oxidation states (Kim et al., 2015; Santiago et al., 2014).

A significant amount of inorganic anions for example nitrate, sulphate, carbonates and chlorides are present in the dyes containing wastewater. The existence of these inorganic anions causes increases mass transfer, colloidal instability and reduce the contact between the photocatalyst and dye molecules

(Eskandarloo et al., 2014; Kango et al., 2013). These CO_3^{2-} and HCO_3^- anions might act as a scavenger for the •OH radicles (Cui et al., 2014; Kango et al., 2013).

$$CO_3^{2-} + \bullet OH \longrightarrow CO_3^{\bullet -} + OH^- \tag{2.14}$$

$$HCO_3^- + \bullet OH \longrightarrow CO_3^{\bullet -} + H_2O \tag{2.15}$$

$$CO_3^{\bullet -} + \bullet OH \longrightarrow HCO_3^- \tag{2.16}$$

The existence of chloride ion also reduce the photocatalytic activity, it was because of the h^+ scavenging ability of Cl^- ion.

$$Cl^- + h^+ \longrightarrow \bullet Cl \tag{2.17}$$

$$\bullet OH + Cl^- \longrightarrow HOCl^{\bullet -} \tag{2.18}$$

$$HOCl^{\bullet -} + H^+ \longrightarrow Cl^- + H_2O \tag{2.19}$$

The active site on photocatalyst surface can be blocked by this synthesized chloride radicle anions. In some other reports the inhibitory effects of phosphate and chloride ions have also been reported (Liu et al., 2016). The inhibiting effect of Cl ion is smaller than the inhibiting effect of CO_3^{2-} ion.

The effect of NO_3^- and SO_4^{2-} on the photocatalytic activity of RR-2 dye using UV light irradiation was reported (Ajmal et al., 2014; Wang et al., 2014). They stated that these inorganic compound enhance the removal of dye in the presence of these inorganic cations. Zhu et al., (2016) also stated similar kind of findings that in the company of NO_3^- enhanced the photocatalytic activity towards the degradation of RhB dye under visible light irradiations (Ma et al., 2014). This improved photocatalytic activities were directly or indirectly were related to the improved •OH radicles generations.

$$NO_3^- + h\nu \longrightarrow NO_2^- + O \tag{2.20}$$

$$NO_3^- + H_2O + h\nu \longrightarrow NO_2^- + 2{\bullet}OH \tag{2.21}$$

$$O + H_2O \longrightarrow 2{\bullet}OH \tag{2.22}$$

2.5.5 Effect of light intensity

The effects of light intensity on the kinetics of the photocatalysis process were reviewed based on the different reports (Ghasemi et al., 2016; Kassahun et al 2017; Friedman et al., 2010; Chong et al., 2010). They stated that at lower light intensity the production of $e^{-}-h^{+}$ pairs was most predominant and the recombination of $e^{-}-h^{+}$ pairs would be negligible. However, at higher light intensity migration of $e^{-}-h^{+}$ pairs contend with the recombination. Therefore, it had very low effect on the degradation rate. Some reported improvement in the photodegradation rate of synthetic dyes was observed with the increase in the intensity of light (Sobaba et al., 2013; Zuo et al., 2014).

Sakthivel et al., (2011) witnessed a linear relation among the photodegradation performance and intensity of light for acid brown 14 at a concentration (20 mg/l, pH=9.41) using ZnO and TiO_2 with catalyst dosage (2.5 g/l). The maximum photodegradation rate for both ZnO and TiO_2 were observed at the light intensity in the range of $1.32-1.37 \times 10^5$ Lux. Kormann et al (2014) studied the relation between the light intensity and degradation rate for the degradation of chloroform using Ag/ZnO photocatalyst. They stated that the •OH radicals were the key reactive agent and the generation of higher •OH radicals were strongly dependent at higher intensity.

Kim et al., (2015) examined the effect of UV light ranged between 12−36 W towards the photodegradation of methyl orange (MO) dye over ZnO photocatalyst. They reported that with the increase in the light intensity the photodegradation performance along with the TOC removal was gradually increased. They further explained that the increase in the photodegradation was not linear but the reliant on the power law, possibly square root dependent, which suggested the degradation reaction was surface controlled to a certain extent.

2.6 Overview of industrial organic pollutants

Wastewater is being contaminated by different sources such as microbes, chemicals, radioactive contaminants and metals particles. Among all the pollutants the organic chemicals such as synthetic dyes and phenolic compounds are among the most hazardous and major source for the aqueous pollution. These chemicals have potential health effects towards eye, kidney, liver damage and increasing risk of cancer. In the following subsections a concise review for the photodegradation of different organic contaminants such as synthetic dyes, phenolic compounds and real textile industrial wastewater using photocatalytic treatment are discussed in detailed.

2.6.1 Synthetic dyes

Numerous industries for example ink, food, paper and pulp, cosmetics and textiles are widely using synthetic dyes as raw materials. Among the synthetic dyes azo class is the largest and most diverse in the colour index list (Pirok et al., 2016). Azo dyes are described by the existence of aromatic rings and sulfonic groups as well as one or more azo bonds, these dyes are being commonly applied in the textile industry (Aravind et al., 2019). Dyes are also often highly carcinogenic, mutagenic and toxic in nature (Zheng et al., 2016). It is an estimation that over 10000 different dyes of this class are synthesized on industrial scale, approximately above 30% of which are used in textile industry and above 25% of these dyes are released to the water bodies during production and application (Rahmatolahzadeh et al., 2017). The discharge of these dyes containing wastewater into the water bodies without any treatment has numerous severe effects on the whole aquatic ecosystem. It is in the dyes nature to resist degradation, they are chemically stable, non-biodegradable and occur as materials that own toxic and mutagenic properties. Hence, a proper treatment is necessary before releasing into the environment. A detailed summary of synthetic dyes degradations using BFO based photocatalyst has been performed and presented in Table 2.3.

Wang et al. (2016) fabricated the Ag/AgCl/BFO composites using a hydrothermal method and analyzed their photodegradation activity towards the elimination of different synthetic dyes such as RhB, MO and methylene blue (MB) at the same time. It was reported that after 35 min of visible light irradiation the photocatalytic activities of 17.7 wt% Ag/AgCl/BFO, pure BFO and Ag/AgCl toward these synthetic dyes were almost 100%, 18% and 70% respectively. Nd and Ni were co-doped on BFO ($Bi_{0.95}Nd_{0.05}Fe_{1-x}Ni_xO_3$) (x= 0.0-0.25) using a sol-gel synthesis method. The prepared composite ($Bi_{0.95}Nd_{0.05}Fe_{1-x}Ni_xO_3$) showed improvement in photodegradation activity towards the degradation of MB because of the improved ferroelectricity, ferromagnetism and ferroelectricity at the same time in a single composite. After 90 min of irradiation under visible light about 95% of the MB was effectively removed from the solution (Vanga et al., 2015). Subhash et al., (2017) used Zr-Ag-ZnO as photocatalyst and check reduction in COD values to confirm the mineralization of reactive red (RR) 120. They observed 96.5 % reduction in COD value after 60 min of light irradiation. It was also confirmed by the passing of the evolved gas (CO_2) through the $Ca(OH)_2$ solution which led to the formation of $CaCO_3$.

Table 2.3: Photocatalytic degradation of different dyes using BFO based nanocomposites in aqueous solution.

Photocatalyst	**Name of the dye**	**Initial concentration of Dye (mg/L)**	**Photocatalyst dose (gL^{-1})**	**Irradiation light source**	**Irradiation time (min)**	**Activity/Reference activity**	**Reference**
Pt/BFO	MO	5	2.5	Visible/ 300 W Xe lamp	210	~100%/ BFO: 15%	(Nui et al., 2016)
CuO/BFO	MO	5	0.25	Visible/300 W Xe lamp	270	70%/ BFO: 25%	(Niu et al., 2015)
g-C_3N_4/BFO	MO	5	1.0	Visible/ 500 W	90	80%/BFO alone: 27%	(Wang et al., 2019)
BFO-PVP	MO	5	0.1	Visible/500 W Xe lamp	180	70%/ pure BFO: 39%	(Wang et al., 2016)
At 150 ^{o}C Hydrogenated BFO	MO	5	3.0	Visible/ 300 W Xe lamp	120	80%/ BFO alone: 22%	(Wang et al., 2018)
Ag/BFO	RhB	5	0.5	Visible/200 W xenon lamp	420	80%/BFO alone: 55%	(Di et al., 2014)
AgCl/Ag/ BFO	RhB	10	1.0	Visible light irradiation	25	99%/Ag/AgCl: 70%	(Wang et al., 2016)

BFO/Bi_2WO_6	RhB	5	1.0	Visible light irradiation	75	59%/BFO: 18%	(Chaiwichian et al., 2017)
BFO/TiO_2-nanotubes	RhB	5	1.0	Visible/500 W Xe lamp	150	85%	(Zhao et al., 2015)
g-C_3N_4/BFO	RhB	10	1.0	Visible/ 300 W Xe lamp	150	92%/BFO alone: 15%	(Fan et al., 2015a)
Gd/BFO	RhB	5	0.3	Visible/300 W Xe lamp	270	85%/ Pure BFO: 23%	(Zhang et al., 2016)
BFO/TiO_2	MB	20	–	Visible light irradiation	150	~80%	(Zhao et al., 2016)
Nd and Ni co-substituted BFO	MB	3.2	0.1	Visible/150 W mercury lamp	90	95%/ BFO alone: 85%	(Vanga et al., 2015)
La-Mn/BFO	CR	10	1.0	Visible/A 300 W xenon lamp	120	96%/BFO alone: 70%	(Fatima et al., 2017)
N-doped graphene/BFO	CR	10	0.25	Visible/A 300 W xenon lamp	120	90%/ $BiFeO_3$ alone: 25%	(Li et al., 2016)

2.6.2 Phenolic compounds

Phenol and its byproducts have been widely applied as raw materials in different industries for example textile, plastic, petrochemical, phenolic resin synthesis, paint, paper-manufacturing and iron smelting (Monlau et al., 2019). The release of the wastewater containing phenolic compounds even in a small amount are harmful to organisms and lot of phenolic compounds has been listed as most hazardous compounds by European Commission and US Environmental Protection Agency (Chowdhury et al., 2017). Phenol is highly toxic and mutagenic compound and it may be absorbed through skin. Naturally, it is found in some foods, animal and human wastes. The one largest application of phenol is as an intermediate in the synthesis of phenolic resins and bisphenol A (Meng et al., 2016; Yin et al., 2016). Several recent research work on the degradation of phenol and its derivatives using BFO based photocatalysts have been summarized in the Table 2.4.

A heterojunction between TiO_2 and BFO was synthesized using a sol-gel synthesis and applied towards the photodegradation of phenol under visible light irradiation. In comparison with BFO and TiO_2, the novel photocatalyst showed improved photocatalytic activity. The findings in their paper suggested that the higher performance was due to the efficient $e^{-}-h^{+}$ pairs separation in TiO_2/BFO photocatalyst (Humayun et al., 2016). BFO/graphene oxide (BFO/GO) heterojunction was synthesized using ultrasonic synthesis technique and utilized towards the photodegradation of bisphenol A. It was reported that after 70 min of visible light irradiation 98% and 72% of the bisphenol A was degraded using BFO/GO and pure BFO, respectively. This improved photocatalytic activity in BFO/GO was due to the enhancement in the surface area which lead to the higher capturing of bisphenol A on the surface of the photocatalyst. Also in BFO/GO nanocomposites, the GO act as e^{-} acceptor and shrink the recombination rate of $e^{-}-h^{+}$ pairs during the reaction (Soltani and Lee, 2016). Kong et al., (2016b) prepared the $(Bi/Fe)_2O_3$/BFO heterojunction using facile hydrothermal process. $(Bi/Fe)_2O_3$/BFO not only reused for five photodegradation cycles towards the toluene.

It can be observed from Tables 2.2, 2.3 and 2.4 that all the reported BFO-based photocatalysts had either irregular or 1D morphologies. Besides, only one report on Pt-BFO (Niu et al., 2015) and 2 reports on Ag-BFO (Kaur et al., 2017; Najot et al., 2016) photocatalysts were available in the literature. Hence, it is essential to synthesis BFO material with 3D morphology, as it could be more helpful to improve the $e^{-}-h^{+}$ pairs separation efficiency. For the first time, in the present research NM-doped BFO with 3D coral-like morphology has been synthesized using two-steps hydrothermal synthesis method. The as-synthesized NM-BFO nanocomposite were applied towards the degradation of MG dye, phenol and real textile wastewater. The effects of various process parameters were also investigated in order to optimize the process conditions. Finally, the photocatalytic activity under direct sunlight was also studied.

Table 2.4: Photodegradation of phenol and its derivatives by BFO based nanocomposites in aqueous solution.

Photocatalyst	**Name of the pollutant**	**Initial Concentration of pollutant (mg/L)**	**Photocatalyst dosage (g/L)**	**Irradiation source**	**Time (mint)**	**Activity/Reference : Activity**	**Reference**
CuO/BFO	Phenol	5	0.25	UV-Vis/300 W Xe lamp	150	60%/under visible light: 40%	(Niu et al., 2015)
TiO_2/BFO	Phenol	10	1.25	Visible/300 W Xe lamp	60	80%/ BFO alone: 35%	(Humayun et al., 2016)
La/BFO	Phenol	20	1.0	Visible/300 W halogen lamp	180	96%/ BFO alone: 25%	(Meng et al., 2016)
Impure BFO	Phenol	50	0.7	direct solar light	300	97.3% removal of phenol	(Soltani and Entezari, 2014)
O_3/Vis/$BiFeO_3$	Phenol	10	0.2	Visible/500 W Xe lamp	60	85%/ O_3/BFO alone: 25%	(Yin et al., 2016)
Ni/Co-BFO	4-Nonylphenol	10	0.2	LED visible light irradiations	90	75%/ BFO alone: 48%	(Ramezanalizadeh & Manteghi, 2017)

BFO/TiO_2nanotubes	4-Chalorophenol	5	1.0	Visible/500 W Xe lamp	180	84%	(Zhao et al., 2015)
Graphene/BFO	Tetrabromobisphenol	20	0.5	Visible light irradiation	240	97%/ BFO alone: 50%	(An et al., 2013)
BFO/GO	BPA	50	0.5	Visible/55 W lamp	70	98%/BFO alone: 72%	(Soltani and Lee et al., 2016)
g-C_3N_4/BFO	Guaiacol	50	0.5	Visible/500 W halogen lamp	60	95%/ BFO alone: 25%	(An et al., 2016)
La/BFO	Phenol red	3.5	0.01	Visible/150 W Xenon lamp	120	90%/BFO alone: 42%	(Dhanalakshmi et al., 2016)
Ba/BFO	Benzene	100	5	Visible/55 W fluorescent lamp	50	95%/ BFO alone: 65%	(Soltani and Lee, 2016)

2.6.3 Real textile wastewater

Immense amount water and chemicals are used during the textile industrial process, for each ton of textile product around 21–377 m^3 of water is used (Sahunin et al., 2016) and consumption of different chemicals usually varies form 10% to above 100% of the weight of the cloth (Jorfi et al., 2016). According to an estimation annual production of dyes are approximately 7×10^5 tons and out of which 280,000 tons of dye stuff has been released into water bodies only through the textile wastewater (Eren, 2012). That is the main reason that textile wastewater contain very high values of COD (150–10,000 mg/L), BOD (100–4000 mg/L), colour content (50–2500) and pH (6-11) (Kalra et al., 2011). Additionally, even releasing of very minor concentration (1 mg/L) of textile wastewater into water bodies are not acceptable and it might generate several toxic chemicals after some time (Koltsakidou et al., 2017).

Kurade et al., (2012) synthesized CuO/TiO_2 and applied it for the reactive orange 16 followed by real textile wastewater. After 3 h of UV-Vis light irradiation, 100% and 78% degradation were observed for reactive orange 16 and real textile wastewater. While after 5 hr of light irradiations 100%, 75% and 72% degradation were recorded in colour, COD and turbidity, respectively. Whereas, the pH was changed from 7.8 to 7.3. $Ce-TiO_2$ photocatalyst was synthesized and applied for photodegradation of textile wastewater using H_2O_2 as additive. 1 wt% $Ce-TiO_2$

photocatalyst showed best photocatalytic activity permitting a 40%, 55% and 42% of TOC, colour and COD removal, respectively (Touati et al., 2016). The CuO-Cu_2O/MCA photocatalyst was prepared and applied for the real textile wastewater treatment under the irradiation of UV-Vis light. It was stated that after 60 min irradiation around 56% and 49% COD and TOC were removed, respectively (Hu et al., 2016).

Danwittayakul et al., (2015) synthesized ZnO/ZTO composites and applied for the photodegradation of MB followed by the real textile wastewater under direct sunlight irradiation. After 3 h of direct sunlight irradiation the photodegradation efficiencies were 100% and almost 50% of MB and real textile wastewater, respectively. After 3 h of light irradiation 75%, 63% and 49% removal were observed in COD, turbidity and TDC, respectively. Whereas pH was changed from 8.2 to 7.4. Jorfi et al., (2016) synthesized UVA/MgO nanoparticles and utilized for the photodegradation of Acid red 73 followed by real textile wastewater under visible light irradiations. After 60 min of visible light irradiation 100% Acid red 73 was degraded. In case of real textile wastewater, after 300 min of visible light irradiation, 100%, 98.3% and 86.9% degradation efficiency were observed for colour, COD and TOC respectively.

2.7 Summary of literature review

Principle and mechanism of heterogeneous photocatalysis were studied in detail to improve the understanding of the process. Among various heterogeneous photocatalysts, BFO is an excellent candidate for industrial photocatalytic applications due to the smaller energy band gap, chemical stability, non-toxicity, inert in nature, superior magnetic and ferroelectric properties. However, the high rate of $e^{-}-h^{+}$ pair recombination and the lower CB position in the pure BFO semiconductor restricts its application to photocatalysis. Numerous attempts have been made in the literature to rectify these problems, including noble metals doping, substitution of metal ions and coupling with other semiconductor materials. The effect of several process parameters such as light intensity, photocatalyst dosage, initial dye concentration, solution pH, humic acid and inorganic anions have been described as they could significantly influence the degradation efficiency of organic contaminants. At last, the photocatalytic applications of BFO based photocatalysts toward the degradation of synthetic dyes followed by phenolic compounds have been reviewed in detailed.

Chapter 3

MATERIALS AND METHODS

This chapter discusses the methodology of experimental work applied in present study. The methodology and experimental set-up of present research are illustrated in the Figure 3.1.

3.1 Materials

All the materials applied in present research were analytical grade and applied without further treatment as tabulated in Table 3.1. Distilled water was used throughout the research.

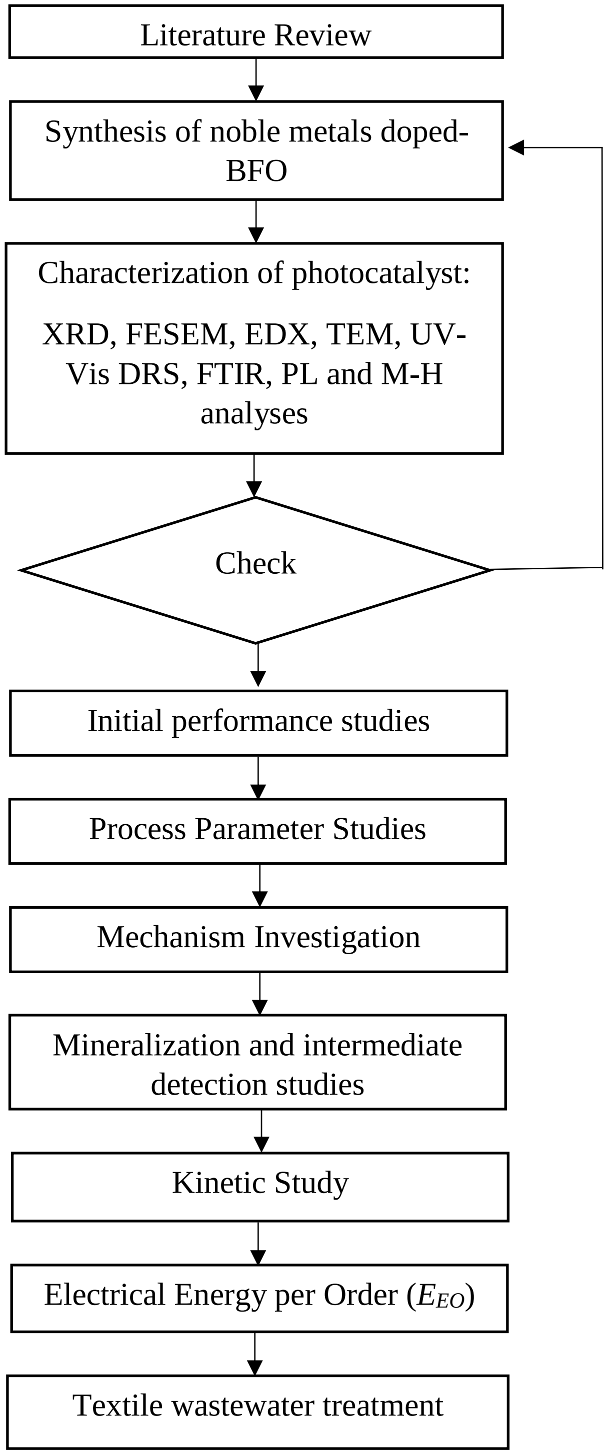

Figure 3.1: Flow chart of overview of research methodology.

Table 3.1: List of materials used for the synthesis of NM-doped-BFO nanocomposite and photodegradation of synthetic dye and phenol.

Materials/Chemicals	**Supplier**	**Purity (%)**	**Purpose of Use**
Bismuth nitrate ($Bi(NO_3)_3.5H_2O$)	ACROS organic	98	Used as precursor in BFO synthesis
Ferrous nitrate ($Fe(NO_3)_3.9H_2O$)	GENE chemicals	99	Used as precursor in BFO synthesis
Urea (CH_4NO_2)	R & M chemicals	98.8	Used for the synthesis of BFO
Nitric acid (HNO_3)	Chemical soln	65	Used for the synthesis of BFO
Potassium hydroxide (KOH)	R & M chemicals	99	Used as a solvent in the synthesis of BFO
Palladium chloride ($PdCl_2$)	Sigma Aldrich	99.7	Pd source in the synthesis of Pd-doped BFO
Silver nitrate ($AgNO_3$)	Sigma Aldrich	99.5	Ag source in the synthesis of Ag-doped BFO
Platinum hydrochloride ($PtH_2Cl_6.6H_2O$)	Sigma Aldrich	99.9	Pt source in the synthesis of Pt-doped BFO
Ethanol (C_2H_5OH)	Chemical soln	99.8	Used for the washing of the photocatalysts
Sodium hydroxide (NaOH)	R & M chemicals	99	Used for pH adjustment
Hydrochloric acid (HCl)	Chemical soln	70	Used for pH adjustment
Potassium iodide (KI)	Sigma Aldrich	99	Used in radical scavenger study
Benzoquinone ($C_6H_4O_2$)	Sigma Aldrich	98	Used in radical scavenger study

Catalase	Sigma Aldrich	10000 units/mg	Used in radical scavenger study
Isopropanol (C_3H_8O)	Sigma Aldrich	99	Used in radical scavenger study
Malachite green	R & M chemicals	85	Used as model pollutant
Phenol	R & M chemicals	99	Used as model pollutant
Humic Acid	Sigma Aldrich	70%	Used as Model pollutant

3.2 Equipment

3.2.1 Teflon-lined autoclave reactor

A Teflon lined autoclave reactor was applied for the hydrothermal synthesis of photocatalysts. The maximum operating temperature and pressure of the autoclave reactor was 200 ^{o}C and 100 bar, respectively. A pressure release valve, pressure gauge and thermocouple were also installed on the reactor. The inside pressure of the autoclave reactor was calculated with the help of pressure gauge, while the temperature was measured using the thermocouple situated at the center of the reactor. The Teflon liner was tightly closed to the stainless steel chamber. A magnetic stirrer was also applied to confirm the homogenization of the reaction mixture.

3.2.2 Ultraviolet-Visible absorption spectroscopy (UV-Vis)

The change in the concentration of organic pollutants was calculated using UV-Vis spectrometer (*HACH DR6000*). The pollutant sample were poured into the cuvette and the adsorption were calculated at a specific wavelength. A fraction of light energy during the analysis were absorbed by the organic pollutant molecules which incur the transfer of electron from smaller energy level to the higher energy level (Kalsi, 2007). The light intensity passing through the organic pollutant will ultimately be decreased. Hence, the change in the absorption of the organic pollutant was measured. Beer-Lambert law explained that the absorption is directly proportional to the solution concentration as presented in the equation 3.1 (Fuwa & Valle, 1963; Sassaroli & Fantini, 2004).

$$A = \varepsilon bC \tag{3.1}$$

Where, A is the absorbance at particular wavelength (Abs), ε is the molar absorptive co-efficient (mg/L/cm), b is the path length (cm) and C is the concentration (mg/L). Therefore, the absorption is directly proportional to the concentration as there is a linear relationship between both of them.

The MG dye and phenol were first scanned to find their maximum absorbance wavelength (nm). The calculated wavelength for MG and phenol were 616 nm and 270 nm, respectively (Kadi et al., 2016; Prince et al., 2015; Saikia et al., 2015; Sharma et al., 2017; Turki et al., 2015).

3.2.3 Visible light irradiation apparatus

Figures 3.2 depicts the schematic apparatus diagram, respectively. The photodegradation of model pollutants were carried out in an acrylic black box under the irradiation of compact fluorescent lamp (CFL). The acrylic black box was used to prevent the solution of model pollutant from other light sources, except the CFL. The CFL was the light source with the light power of 105 W and had an intensity of about 1.02×10^4 lux striking on the surface of model pollutants as measured using digital lux meter (UT383BT).

Many researchers (Lam et al., 2018; Jaffari et al., 2019a) reported that the CFL contains the irradiation of both UV and visible spectrum. UVA and UVC radiometers (Series 9811, Cole Parmer, USA) were used to calculate the UV light portion of the CFL lamp. The UV portion was 0.81 mW cm^{-2}, while the UV flux of the solar light is in the range of 2−3 mW cm^{-2} (Lam et al., 2018; Jaffari et al., 2019b), so it can be presumed that photodegradation reaction was mostly because of the visible light. The aqueous solution of MG dye was used as model pollutant which was poured into a 250 mL glass beaker under the irradiation of visible light for photodegradation experiments.

Two fans were applied to control the black box temperature due to the heat produced by the light irradiation. The air pump was applied to pump the air throughout the experiment. The air flow rate of 2 L/min was adjusted with the help of rotameter which was connected to the air pump. The mixture of organic pollutants and photocatalyst was stirred very well with the help of magnetic stirrer. All the photodegradation experiments were duplicated to enhance the accuracy of the experimental works.

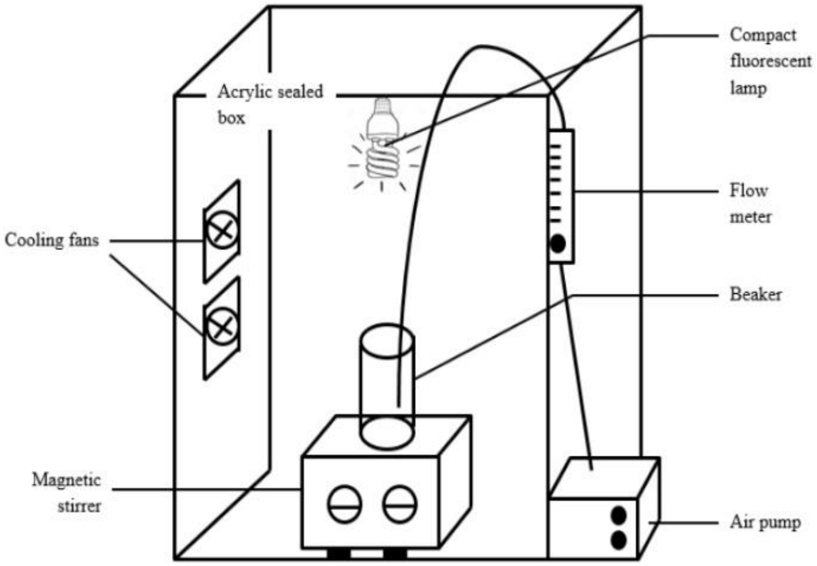

Figure 3.2: Schematic illustration of visible light apparatus.

3.2.4 Sunlight irradiation apparatus

The photodegradation of organic pollutants were also carried out under the irradiation of sunlight. UVA and UVC radiometers were used to calculate the UV light portion of the sunlight. The UV portion was 3.27 mW cm^{-2}, so it can be presumed that photodegradation reaction was mostly because of the UV-Vis light irradiation. The model pollutant was poured into a 250 mL glass beaker under the irradiation of direct sunlight using photodegradation experiment. After attaining the adsorption desorption equilibrium, the suspension were exposed to the direct sunlight. Magnetic stirrer was used to perform stirring at constant speed of 500 rpm. All the photodegradation experiments were duplicated to improve the accuracy of the experimental works.

3.3 Synthesis of photocatalyst

3.3.1 Synthesis procedure of pure BFO

In present research, pure BFO was synthesized using urea-assisted hydrothermal synthesis method (Wei et al., 2012). In pure BFO synthesis, 25 mL aqueous solution of $Bi(NO_3)_3.5H_2O$ (5 mM), $Fe(NO_3)_3.9H_2O$ (5 mM), HNO_3 (0.002 L) and urea (100 mM) in distilled H_2O was prepared using magnetic stirrer. The prepared suspension was vigorously stirred till it was converted into an brownish red solution. Then, this suspension was inserted dropwise into a 20 mL KOH solution (10 M) under constant stirring. Afterwards, this whole mixture was shifted into an autoclave reactor at 125 ^{o}C for 15 h. At the end of the hydrothermal reaction the autoclave was permitted to cool down naturally. Then, the prepared product was washed with H_2O and ethanol for many times before drying in an oven at 80 ^{o}C for 4 h.

3.3.2 Synthesis procedure of NM-doped BFO

The NM-doped BFO photocatalysts were synthesized using hydrothermal synthesis method (Zhang et al., 2017). In the NM-doped BFO synthesis, a certain amount of NM precursors were mixed separately in 30 mL of methanol and the mixture was placed in the ultrasonic system with 40 kHz/100 W for 15 min at room temperature. The amount of NM changed from 0.5 wt% − 4 wt%, which corresponded to the 0.5wt%, 1wt%, 2 wt%, and 3wt%, respectively. Afterwards, as-synthesized 1 g of coral-like BFO was mixed in the above mixture and ultrasonicate further for 20 min. Then, the mixture was shifted into a Teflon lined reactor for 240 min at 100^{o}C. The autoclave was permitted to cool down naturally at the end of hydrothermal reaction. The prepared products were collected, washed and dried at 80^{o}C in an oven for 4 h for further characterization. The synthesized samples were denoted as *x* wt% NM-BFO nanocomposite (*x* = 0.5, 1, 2, 3 and 4).

3.4 Analytical and characterization techniques

3.4.1 X-ray diffraction (XRD)

XRD technique is widely applied to observe the crystal structure and crystallinity of the newly synthesized photocatalysts. The XRD measurement was executed at 40 kV and 30 mA with the scanning rate of 0.01^{o}/s (Cu Kα radiation =

1.5406 Å) in the range from 20° to 80° with the integrated software (X' Pert HighScore). The obtained diffraction peaks in XRD spectrum were matched with the database of Powder Diffraction File (PDF), circulated by the International Center for Diffraction Data (ICDD) for identifying the phase and crystallinity of the photocatalysts.

3.4.2 Field Emission Scanning Electron Microscopy (FESEM)

FESEM is applied to visualize the surface morphology of photocatalyst with highly magnified optical images. The sample preparation for FESEM analysis was started by the spreading the sample on top of the carbon tape, which was fixed on the aluminum sample stub. Before the test, sample stub was placed inside the auto fine coater (JFC-1600) for the platinum coating. The photocatalyst morphology and particle size were witnessed using FESEM (Quanta FEG 450) operating at 5 kV and high vacuum with a magnification of 25 kX.

3.4.3 Energy Dispersive X-ray Spectroscopy (EDX)

EDX is a chemical microanalysis method used for quantitative, qualitative and elemental mapping examination. Octane Silicon Drift Detector (SDD) was used at high voltage of 15 kV using Mn Kα as source of energy. The elemental mapping and composition of the NM-doped BFO nanocomposite were measured by INCA Energy 400 software along with the image taken by Quanta FEI 450 instrument.

3.4.4 Transmission Electron Microscopy (TEM)

TEM was mainly applied to double confirm the shape of the synthesized NM-doped BFO nanocomposite. The sample preparation for TEM analysis started by scattering a small amount of the photocatalyst in ethanol followed by sonication for 10 min. Afterwards, a droplet of the sample was placed on Cu grid covered with amorphous carbon film. The prepared sample must be dried before analysis. In present research, TEM is conducted on JEOL, JEM 2010 instrument with an accelerating voltage of 200 kV.

3.4.5 X-ray Photoelectron Spectroscopy (XPS)

XPS is the most widely used surface analysis technique because it can be applied to a wide range of materials and provided chemical state information from the surface of the samples. In this study, XPS spectra of 2 wt% Pd-BFO nanocomposite were recorded using PHI Quantera II Physical Electronics in MIMOS Berhad, Technology Park Malaysia. Typically, the surface of sample was excited by mono-energetic Al kα x-rays causing photoelectrons to be emitted from the sample surface. Then the energy of the emitted photoelectrons was measured by an electron energy analyzer. By using the binding energy and photoelectron peak intensity, the elemental identity and chemical state of Pd-BFO powders were detected.

3.4.5 Photoluminescence (PL) analysis

The PL spectroscopy has been widely applied to investigate the electronic structure, photochemical and optical characteristics of metal oxides semiconductors in the field of photocatalysis. The sample preparation for PL measurement was started by placing the small amount of powder photocatalyst on the glass slide before placing it on the spectrophotometer. The PL spectra were investigated in the range from 400 nm to 600 nm via a spectroflurometer (Perkin Elmer S55), at room temperature at 325 nm excitation wavelength.

3.4.6 Fourier Transformed Infrared (FTIR) Spectroscopy

FTIR spectroscopy was applied to find the functional group and type of chemical bond of the NM-doped BFO. The photocatalysts were mixed and well-grinded with the KBr. Then this mixture was converted into a thin pellet under high pressure. The FTIR analysis was performed by FTIR (Perkin Elmer Lambda 35) in the range 400−4000 Cm^{-1}.

3.4.7 UV-Vis Diffuse Reflectance Spectroscopy (UV-Vis DRS)

UV-Vis DRS was applied to measure the optical properties and E_g energies of noble metals doped BFO. DRS were investigated via UV-Vis spectrophotometer (Perkin Elmer Lambda 35) in the range from 200 to 800 nm. Barium sulfate ($BaSO_4$) were used as reference in current analysis. with the help of UV-Vis DRS spectra, the E_g energy can be calculated from a graph $((F(R)hv)^{1/2}$ vs photon energy (hv) through Kubelka-Munk (K─M) function and E_g equation (Guy & Ozacar, 2016; Kaur et al., 2016).

$$F(R) = \frac{(1-R)^2}{2R} \tag{3.2}$$

$$E_g = \frac{h_c}{\lambda} \tag{3.3}$$

where $F(R)$, R, E_g, h_c, c, λ are the K–M function, reflectance (%), band gap energy (eV), Planck's constant (4.135667×10^{-15} eVs), speed of light (3×10^8 m/s) and wavelength (nm) of onset absorption, respectively.

3.5 Photocatalytic activity of the photocatalyst

3.5.1 Photocatalytic activity of the photocatalyst under visible light irradiation

The photocatalytic activities of as-synthesized pure BFO and NM-doped BFO nanocomposite were assessed by the photodegradation of aqueous MG dye and phenol solution. The experimental procedure was as follows: 0.1 g catalyst was inserted in 10 mg/L MG dye or 5 mg/L phenol. During all the photocatalytic tests, air was constantly passed from the aqueous suspension with a flow rate of 2 mL $\min^{-1}$. The solution was constantly agitated using a magnetic stirrer for 30 min in the dark to attain adsorption-desorption equilibrium. Afterwards, the solution was exposed under visible light from a fixed distance of 12 cm above the aqueous suspension surface. After specific time intervals, the samples were taken from the system and the catalyst was separated using a small magnetic bar. The residual MG dye or phenol concentrations in the aqueous solution were monitored via an UV-vis spectrophotometer (*Hach* DR6000) at the maximum absorbance wavelength of 616 nm and 270 nm, respectively. All the photodegradation experiments were duplicated to improve the accuracy of the experimental works. Moreover, the photodegradation efficiencies of as-synthesized photocatalysts and commercially available TiO_2 were also compared.

$$\text{Degradation efficiency} = \frac{C_o - C_t}{C_o} \times 100 \tag{3.4}$$

where, the photodegradation efficiency were expressed in terms of percentage (%), C_o was the initial pollutant concentration (mg/L) and C_t was the concentration of the pollutants at particular time (t) (min) (mg/L).

3.5.2 Photocatalytic activity of the photocatalyst under direct sunlight irradiation

The photodegradation experiment was carried out using direct sunlight as a source of energy. The experiment was performed at ambient temperature. The experimental conditions and procedure for the photodegradation under direct sunlight was exactly the same as photodegradation under CFL light irradiation. After attaining the adsorption desorption equilibrium the experimental set-up was placed under direct sunlight between 11 a.m. and 3 p.m. the average sunlight intensity during this period was 1.817×10^5 Lux. After certain intervals of time, a certain volume of samples were acquired from the beaker after filtration and centrifuged the organic pollutants concentrations were calculated via UV-vis spectrophotometer (*Hach DR6000*) at a particular wavelength. All the photodegradation experiments were duplicated in order to achieve more accuracy in the readings. The photodegradation efficiencies were calculated using Equation (3.6).

3.6 Photoelectrochemical measurements

The photoelectrochemical experiments were carried out on a conventional electrochemical potentiostat (*Gamry Interface 1000*) in a three-electrode quartz cell. Ag/AgCl electrode and Pt wire were applied as reference and counter electrode, respectively, while the fluorine-doped tin oxide (FTO) glass coated with samples was utilized as a working electrode. The 0.5 M sodium sulfate (Na_2SO_4) solution was used as an electrolyte. The 105 W lamp (Hazzle, Malaysia) offered a source of visible light irradiation. The photocurrent density measurement was calculated under the light irradiation (30 sec on/off cycle) at a bias potential of 0.4 V vs Ag/AgCl. Electrochemical impedance spectroscopy (EIS) was conducted in the frequency ranged from 10^4 to 0.1 Hz.

3.7 Detection of active species

3.7.1 Reactive oxidation species (ROS) identification

It was well-known fact that the production of reactive radicals species (•OH, $\bullet O_2^-$, H_2O_2 and h^+) played the most vital role in the photodegradation of organic contaminants (Xu et al., 2013; Soltani and Entezari, 2014; Lam et al., 2018). Therefore, it was necessary to find the role of different reactive radicals responsible for the MG degradation. The role of different radicals such as •OH, $\bullet O_2^-$, H_2O_2 and

h^+ in the photodegradation reaction were evaluated by inserting 2 mM of numerous trapping agents in the 250 mL beaker containing 100 mL solution of organic pollutant along with 1 g/L photocatalyst dosage, 10 mg/L substrate concentration and at natural solution pH. For reveling ROS, benzoquinone (BQ) was used to rectify the importance of $\bullet O_2^-$ radicals, isopropanol (IPA) was applied to identify •OH radicals, catalase was used to determine the role of H_2O_2, while potassium iodide (KI) was used to find the role of h^+ during photodegradation.

3.7.2 Hydroxyl (•OH) radicals investigation

The generation of •OH radicals over the NM-doped BFO nanocomposites was estimated by using the following method (Bharathkumar et al., 2015): terephthalic acid (TA) with the concentration (5×10^{-4} M) was dissolved in 100 mL dilute NaOH solutions of the concentration (2×10^{-3} M). The 1 g/L photocatalysts were added to the solution and perform stirring in the dark for 30 min. Then, suspension was irradiated under visible light using the same photocatalytic conditions. The TA react with the •OH radicals and convert into 2-hydroxyterephthalic acid (2HTA). The TA-PL analysis was conducted at room temperature using fluorescence spectrometer (PerkinElmer LS-55) at excitation wavelength of 315 nm.

3.8 Operating parameters

3.8.1 Effect of photocatalyst dosage

The effect of catalyst dosage on photodegradation of MG dye was studied using a fixed amount of MG dye concentration 10 mg/L and at natural solution pH of pH5.45. The catalyst loading was varied in the range from 0.5 g/L to 2.5 g/L. The selection of photocatalyst dosage range was based on the different research reports available in literature (Davididou et al., 2017; Lourdes et al., 2017; Mohammad et al.,2017; Zhang et al., 2014).

3.8.2 Effect of pollutants concentration

The effect of pollutants concentration on photodegradation of MG dye and phenol were studied using 100 mL of aqueous solution. The initial organic pollutants concentrations were ranged between 5−80 mg/L (5, 10, 20, 40 and 80 mg/L). The selection of initial pollutant concentration range was based on the literature reports (Asghar et al., 2015; Jia et al., 2017; Zhang et al., 2014). The photocatalytic reactions were performed using a constant photocatalyst dosage of 1 g/L and at natural solution pH of pH 5.45 and pH 5.4 for MG and phenol, respectively.

3.8.3 Effect of solution pH

The influence of solution pH on the photodegradation of organic pollutants were investigated on the pH range from pH 3.0 to 9.0 (Hadjltaief et al., 2015; Bhattacharjee et al., 2014; Huang et al., 2008). Dilute HCl and NaOH were applied to fix the pH. The pH range was chosen based on the different conditions, for example, acidic (pH 3), natural (pH 5.44 and 5.4 for MG and phenol, respectively), neutral (pH 7) and alkaline (pH 9) media. The experiment was performed using a HANNA Instruments HI2550 pH/ORP & EC.TDS/NaCl Meter. The photocatalytic reactions were carried out using 1.5 g/L photocatalyst dosage and 5 mg/L initial organic pollutant concentration.

3.8.4 Effect of inorganic anions

The effect of anions on photodegradation of MG dye were studied using 100 mL of aqueous solution. The influence of several inorganic anions (Cl^-, CO_3^-, HCO_3^- and $H_2PO_4^-$) on the photodegradation of MG dye was witnessed. The salt concentration of 20 mM was chosen as per research performed by Dugandzic et al., (2017). The experiment was carried out using 1.5 g/L photocatalyst dosage, 5 mg/L initial substrate concentration and at pH 7.0.

3.8.5 Effect of humic acid

The effect of humic acid on the MG dye photodegradation was studied using 1.5 g/L photocatalyst dosage, initial MG dye concentration of 5 mg/L and at pH 7.0. The concentration of humic acid was changed in the range between 0 mg/L to 10 mg/L (0, 2, 5, 7 and 10 mg/L). The selection of humic acid concentration range was based on the different research reports available in the literature (Oskoei et al., 2016; Valencia et al., 2013).

3.9 Photocatalyst reusability studies

The reusability of Pd-doped BFO nanocomposite was also studied by consecutive six cycles of experiments. The solution pH and MG dye concentration were retained constant at 10 mg/L and pH 7.0, respectively. After 150 min of light irradiation, the dye solution was collected and centrifuged to separate the photocatalyst. The photocatalyst was then washed using distilled H_2O for several times, dried at 120^oC for 4 h and then again placed in the fresh MG solution under the same conditions for the successive run.

3.10 Real textile wastewater quality testing

Real textile wastewater was taken from Penfabric Sdn Bhd at Butterworth, Penang, Malaysia and stored in a refrigerator at 4 ^{o}C. The textile wastewater was pre-characterized and some specific parameters such as Ammoniacal nitrogen (AN), colour, total suspended solids (TSS), biochemical oxygen demand (BOD_5), turbidity, chemical oxygen demand (COD) and pH were examined.

3.10.1 Biochemical Oxygen Demand (BOD_5)

BOD_5 was calculated to measure the extent to which the oxygen in the specimen can help the microorganism according to the dilution method (Association, Association, Federation, & Federation, 1915). The specimen was diluted with the dilution factors and poured into the 300 mL BOD bottle. Initial dissolved oxygen (DO_0) was calculated using DO meter (EUTHECH DO 2700). Afterwards, the BOD bottle was sealed immediately with parafilm to prevent the air from entering the bottle. Then, the BOD bottle was stored in the BOD incubator (VELP SCIENTIFICA FOC 225E) at 20 ^{o}C for 5 days. After 5 days incubation, the final dissolved oxygen was calculated. The BOD_5 was calculated using the Equation (3.6).

$$BOD_5 = \frac{DO_0 - DO_5}{Dilution\ Fraction} \tag{3.6}$$

where DO_0 was initial DO (mg/L), DO_5 was the final DO after 5 days of incubation (mg/L).

3.10.2 Chemical Oxygen Demand (COD)

The degree of mineralization of MG dye and phenol were studied by using the COD analyzer. For the sample preparation, 2 mL of distilled water as a blank sample and 2 mL of dye/phenol samples were dropped into HR COD digestion reagent vials and mixed gently. The COD reactor was preheated to 150 ^{o}C and placed these COD vials for 2 h. then, the vials were naturally cool down to room temperature and proceeded for the testing with UV-Vis spectrophotometer (HACH DR6000). The blank sample was set as zero and COD values of MG dye and phenol sample were obtained.

3.10.3 Ammoniacal Nitrogen

NH_3-N was applied to calculate the NH_4^+ ions concentration present in textile wastewater by ammoniacal nitrogen compounds according to Nessler method in APHA 2005 (Joseph & Thiripuranthagan, 2015). Those compounds contain the mineral stabilizer, polyvinyl alcohol dispersing agent and Nessler reagent. A dilute sample with the volume of 25 ml was prepared. Three drops of mineral stabilizer were then added into the dilute sample and mixed gently. Then, three drops of polyvinyl alcohol dispersing agent were added and again mixed gently. Next, 1 mL of Nessler compound was added into the sample and homogeneous mixture was prepared for the calculations. The blank sample was used to adjust the zero in UV-Vis spectrophotometer (HACH 6000) at 425 nm wavelength under 380 Nitrogen Ammonia Nessler program.

3.10.4 Colour

Colour test was applied to calculate the pollutant level in textile wastewater according to the method 8025 Platinum-Cobalt (Pt-Co) standard method by Hach Company. Before the measurements, sufficient dilution was required to ensure that the results were within the range of spectrophotometer. Two empty glass vials were filled with the specimen and distilled water, respectively. The results were obtained using UV-Vis spectrophotometer (*HACH DR6000*) at the wavelength 465 nm. A blank sample was used to adjust the zero and the tested colour value was obtained in Pt-Co scale.

3.10.5 Turbidity

Lovibond Turbicheck turbidity meter was used to check the turbidity of the specimen without diluting the solution. The meter was needed to be calibrated with the standard solution before use. After calibration, the specimen was filled in the sample cell until the marked line and wiped with the clean towel. The turbidity of the specimen was measured in Nephelometric Turbidity Units (NTU).

3.10.6 Suspended Solids

The amount of suspended solids present in the specimen was calculated using suspended solid measurement. Before starting the measurements one blank sample using distilled water was applied for zeroing purpose. Then direct measurements were taken using UV-Vis spectrophotometer (*HATCH DR6000*).

3.11 Kinetic studies

The kinetic profile of the MG dye and phenol photodegradation over NM-doped BFO nanocomposite were investigated with the help of L-H model (Di et al., 2014; Lam et al., 2018; Patil et al., 2016). A fixed amount of MG dye and phenol solution was withdrawn from the reaction mixture and their concentrations were checked as a function of time. In the L-H kinetic model, it was assumed that the surface coverage of substrate, which was in relation with the concentration in the bulk solution had strong effects on the degradation rate (Lam et al., 2010). The photocatalytic degradation rate was calculated by fitting the experimental values in the Equation (3.7).

$$\ln\left(\frac{C_0}{C}\right) = kt \tag{3.7}$$

where C_o and C are the initial and final substrate concentration (mg/L) with respect to the time (t) and k is the rate constant (1/min).

CHAPTER 4

RESULTS AND DISCUSSIONS

The results of the present research were presented in this chapter. The first section of this chapter discusses the important characterizations of the as-synthesized noble metals loaded on coral-like BFO nanocomposites (NM-BFO, NM = Ag, Pt and Pd). The synthesized nanocomposites were applied in the photodegradation of MG dye under the visible light irradiation. The photocatalytic mechanism of the synthesized nanocomposites was also proposed. In the next section, several key process parameters such as intensity of light irradiation, photocatalyst dosage, initial concentration of pollutants, solution pH, effect of inorganic anions were investigated to evaluate the degradation performance of Pd-BFO nanocomposites. The next section consists of the photocatalytic comparison with the commercially available photocatalyst such as TiO_2. Apart from that, visible light degradation of phenol using 2 wt% NM-BFO was also studied. With the help of COD analyses, the mineralization extents of MG dye and phenol were investigated. The intermediate products generated during phenol degradation was identified using HPLC analysis. The obtained data of Pd-BFO nanocomposites was then fitted through the L-H kinetic models. The electrical energy required by the Pd-BFO nanocomposite was estimated via electrical energy per order (E_{EO}) and compared with the pure BFO as well as commercial TiO_2. The synthesized Pd-BFO nanocomposite was also applied towards the photodegradation of real-textile wastewater using the optimized process parameters. In the last part, direct sunlight irradiation was applied towards the photodegradation of MG dye as well as phenol using several photocatalysts.

4.1 Characterization of photocatalysts

Characterization of the synthesized nanocomposites is the most essential during the photocatalysis studies, as it exposes the phase structure, chemical, morphological, optical and magnetic characteristics of the photocatalysts. The outcomes of these techniques can deliver suitable causes for higher or lower photocatalytic performances. Therefore, the as-synthesized NM-BFO nanocomposites were characterized by the XRD analysis to study the crystal structure and phase purity. FESEM and TEM were performed to examine the morphology. HRTEM was used to study the crystal lattice. The elemental composition was performed using EDX analysis. The optical properties were checked using UV-vis DRS and PL analyses. The functional groups present on the photocatalysts were studied by FTIR, while the M-H loop was utilized to investigate the magnetic properties of the photocatalysts.

4.1.1 XRD analysis

The crystal structure of the pure BFO and NM-BFO nanocomposite with numerous loadings were investigated through XRD technique and the findings are exhibited in Figure 4.1. The XRD pattern exhibited sharper peaks, which indicated high degree of crystallinity. All the diffraction peaks were labelled and well consistent with rhombohedral perovskite structure with the *R3c* space group (JCPDS NO. 86−1518) (Bharathkumar et al., 2015; Soltani & Entezari, 2013). The calculated analogous lattice parameters of BFO were $a = b = 0.55774$ nm and $c = 1.38667$ nm, respectively. The diffraction peaks located on 22.6^o, 32.2^o, 32.4^o, 39.9^o, 45.8^o, 51.9^o, 52.4^o, 56.7^o, 58.1^o, 67.2^o, 67.8^o, 71.1^o and 71.5^o were indexed to the (012), (104), (110), (202), (024), (116), (122), (018), (214), (208), (131), (128) and (134) crystal plane, respectively. Moreover, the diffraction peaks for NM such as Pt and Pd were also detected over the NM-BFO nanocomposites. Pt-BFO nanocomposites exhibited the diffraction peaks located at 38.8^o (111) and 46.0^o (200), which revealed the existence of metallic Pt (JCPDS NO. 05-0681) (Alamelu & Ali, 2018; Hsieh, Chen, & Wu, 2015). In the case of Pd-BFO nanocomposites, the diffraction peaks appeared at 40.1^o (111) and 46.7^o (200) were the indication of the presence of metallic Pd (JCPDS PDF card 88-2335) (Meng & Zhang, 2017; Ni et al., 2016). The intensities of these peaks became stronger with the rise in the noble metals loadings. However, in case of Ag-BFO nanocomposite, the XRD patterns were almost alike to that of the pure BFO and no new peak for Ag was witnessed, which might be because of the lower contents of metallic Ag, as presented in the past literatures (Kaur et al., 2017; Navjot et al., 2017). Furthermore, no noticeable shift in the diffraction peaks was observed because of the variation in the crystal lattice of BFO.

Kaur et a., (2017) synthesized Cu and Ag-loaded BFO nanocomposites using hydrothermal synthesis method followed by photo-deposition technique and characterized their crystal structure with the help of XRD. Based on the XRD results, the synthesized Cu and Ag-loaded BFO nanocomposites well agreed with the standard data of rhombohedral perovskite structure of BFO and no peak for either Cu or Ag were detected in the XRD spectra. Niu et al., (2015) synthesized Pt-BFO nanocomposite via hydrothermal synthesis method and applied towards the photodegradation of methyl orange (MO) dye. The synthesized Pt-BFO photocatalyst was characterized by XRD for studying the phase and crystal structure. They stated that the peaks in the XRD pattern can be attributed to the diffraction of (012), (104), (110), (202), (024), (116), (122), (018), (214), (208), (131), (128) and (134) crystal plane of the perovskite BFO. The peak for metallic Pt was not found in the XRD patterns.

Alamelu and Ali, (2018) synthesized Pt-TiO_2 and applied as the visible light photocatalyst towards the photodegradation of RhB dye and 4-nitrophenol. The synthesized Pt-TiO_2 were characterized via XRD technique, and the results stated that the pure TiO_2 had the anatase (101) and rutile (110) phase. The XRD patterns of Pt-TiO_2 nanocomposites depicts two new peaks at 38.7^o and 46.0^o matching to the (111) and (200) crystal planes, respectively. Ni et al., (2016) synthesized Pd-loaded g-C_3N_4 nanosheet using sol-gel synthesis method and the crystal structure of synthesized material was investigated via XRD technique. For the pure g-C_3N_4, the main dominating peaks appeared at 13.1^o and 27.6^o corresponding to the (002) and (100), respectively. While in the case of Pd-g-C_3N_4, two new peaks at 40.1^o and 46.1^o were observed, suggesting the successful reduction of Pd^{2+} on the surface of g-C_3N_4.

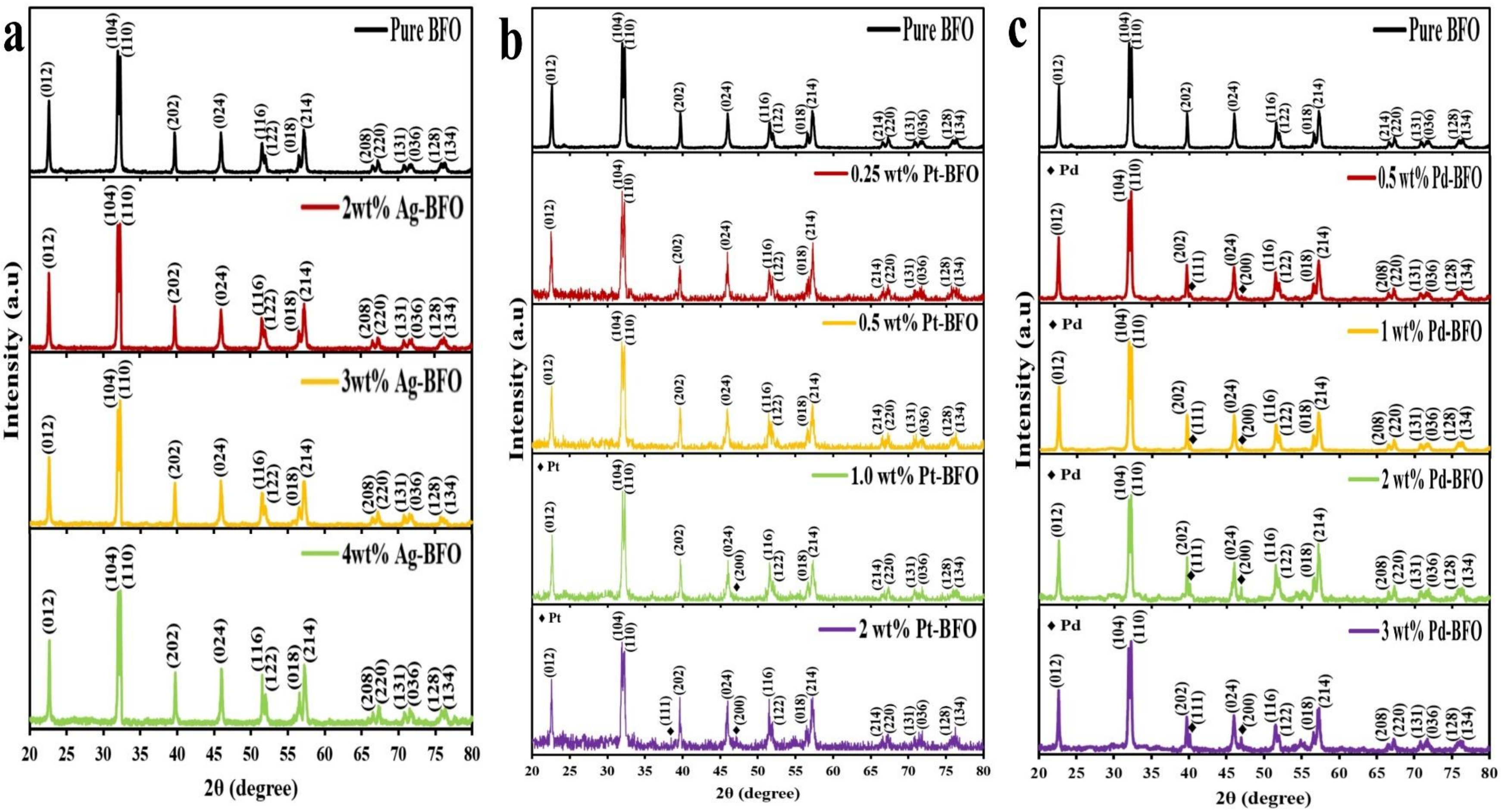

Figure 4.1: XRD patterns of NM-loaded BFO for different NM loadings **a** Ag-BFO, **b** Pt-BFO and **c** Pd-BFO nanocomposite.

4.1.2 FESEM analysis

The morphologies of pure BFO and 2 wt% NM-BFO nanocomposites were witnessed through FESEM technique and the findings are presented in Figure 4.2. Figure 4.2a depicts the FESEM image of pure BFO with high yield generation of coral-like BFO structure. The surface of the coral-like structure was uniform and smooth with an average diameter of around 110-130 nm. The FESEM image exhibited that the nanostructures were interconnected with each other and form a 3D coral-like structure. As can be seen from Figures 4.2 b-d, the nanocomposite still maintain their coral-like shape after the loading of NM such as Ag, Pt and Pd on the surface of BFO. It indicated that the loading of different NM was not able to alter the coral-like BFO morphology. However, there were visible small nanoparticles connected on the surface of the coral-like BFO.

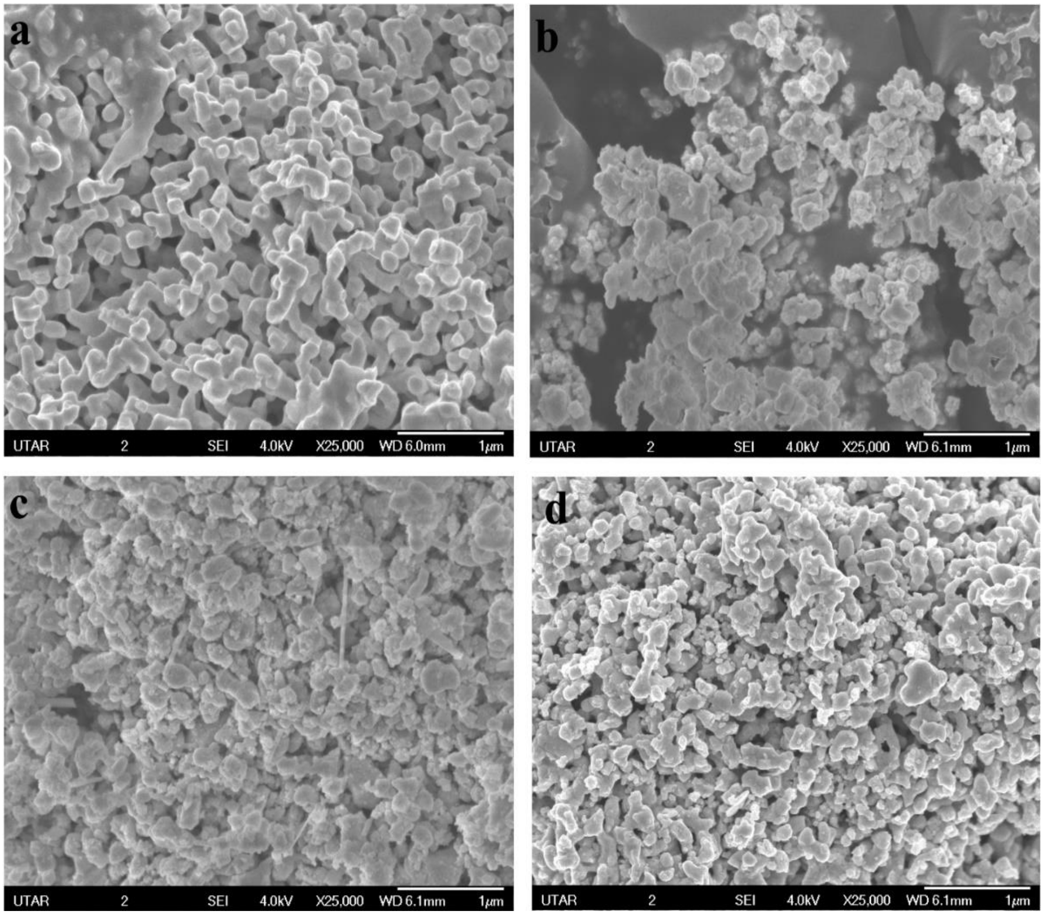

Figure 4.2: FESEM images of **a** pure BFO, **b** 2 wt% Ag-BFO, **c** 2 wt% Pt-BFO and **d** 2 wt% Pd-BFO nanocomposite.

The FESEM images for Pd-BFO with the different Pd wt% loading contents are displayed in Figure 4.3. Figure 4.3a depicts the FESEM of 0.5 wt% Pd-BFO nanocomposite. It was observed that the Pd nanoparticles didn’t produce any modification in the morphology of the coral-like BFO, and the Pd nanoparticles were homogeneously dispersed on the entire BFO surface. With increasing the Pd loading contents, coral-like BFO was covered with more Pd nanoparticles and the surface of BFO became rough. Further increasing the Pd contents to 3 wt%, the surface of coral-like BFO nanocomposites became rougher as witnessed in Figure 4.3 d.

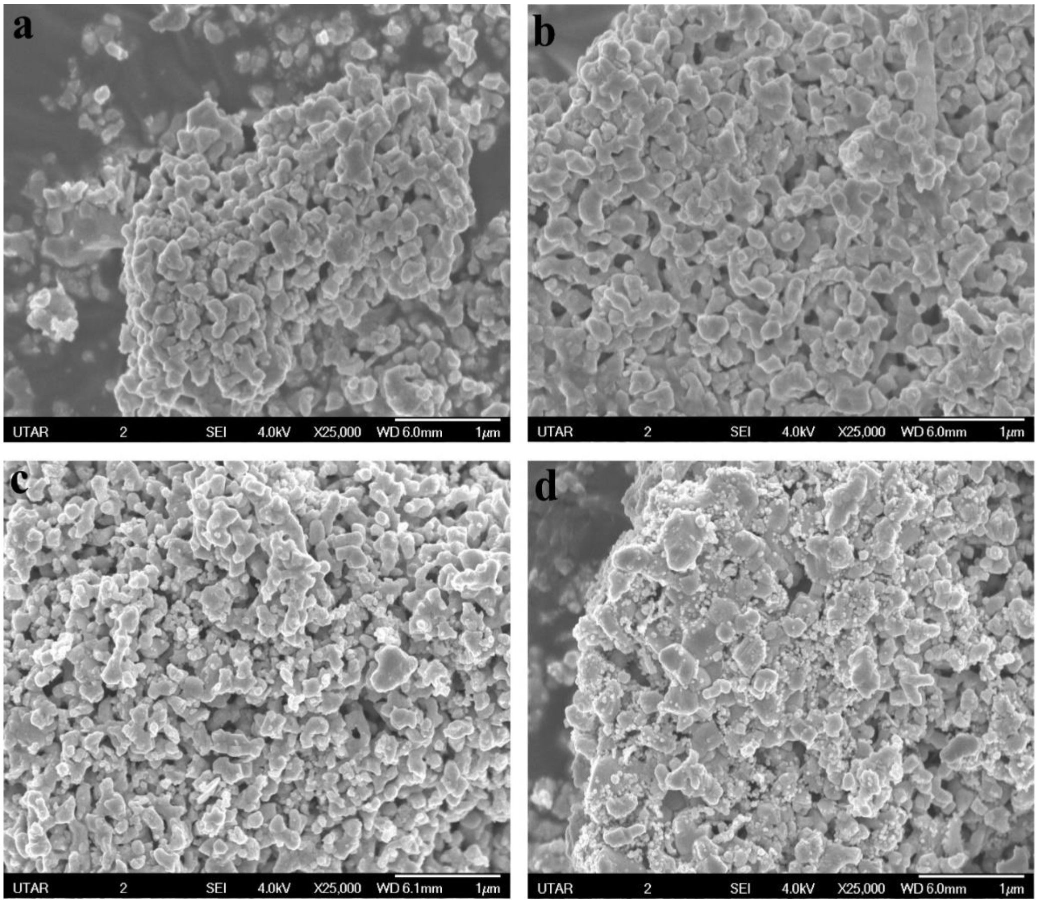

Figure 4.3: FESEM images of **a** 0.5 wt% Pd-BFO, **b** 1 wt% Pd-BFO, **c** 2 wt% Pd-BFO and **d** 3 wt% Pd-BFO nanocomposites.

4.1.3 EDX analysis

To investigate the elemental composition present in the pure BFO and 2 wt% NM-BFO nanocomposite, EDX analysis was recorded in the binding energy region from 0 to 15 keV as exhibited in Figure 4.4. The elements Bi, Fe and O were clearly observed in the spectra of the pure BFO. The presence of C was because of the applied carbon tape. Figures 4.4b-d shows the EDX analysis of 2 wt% NM-BFO nanocomposite. The presence of NM were clearly witnessed in the spectra of NM-BFO nanocomposites. Table 4.1 shows the atomic percentages of the different elemental compositions of as-synthesized nanocomposite. From the EDX findings, the weight percentages of elemental Ag, Pt and Pd on the BFO were determined as 2.01, 2.01 and 2.35, respectively.

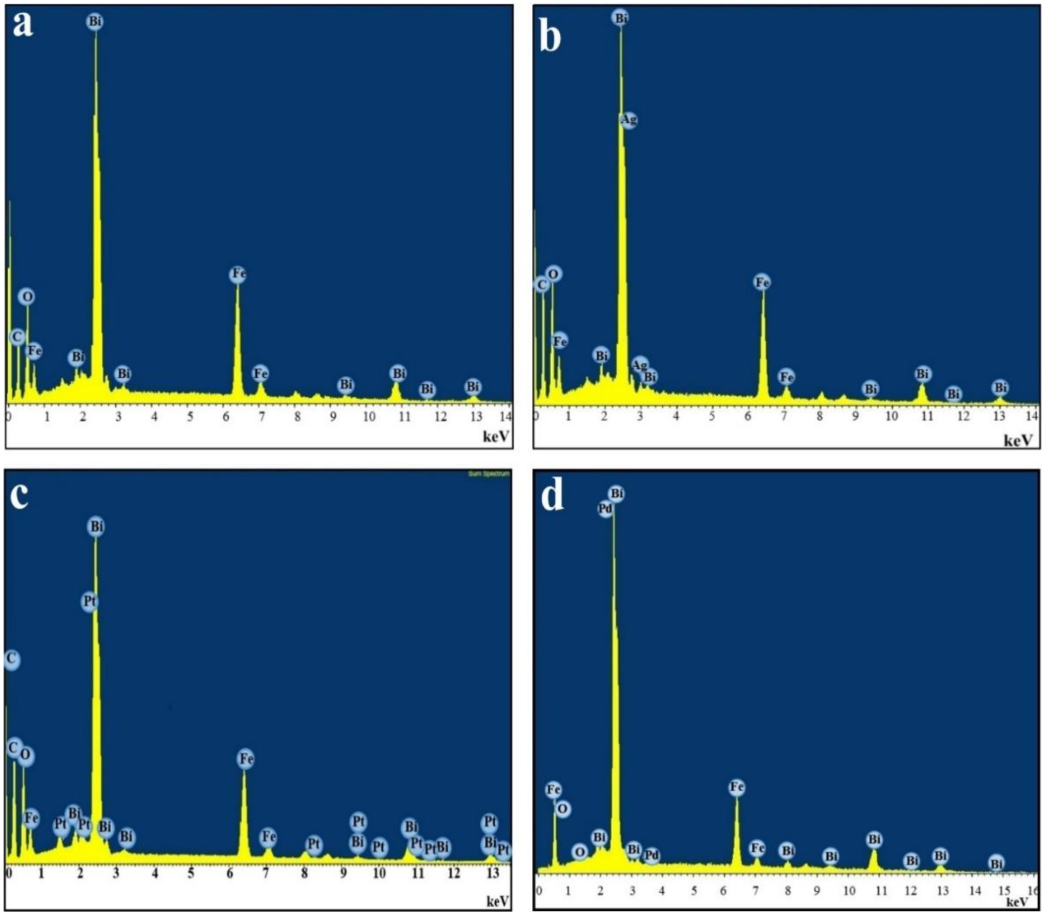

Figure 4.4: EDX analysis **a** Pure BFO, **b** 2 wt% Ag-BFO **c** 2 wt% Pt-BFO and **d** 2 wt% Pd-BFO nanocomposie.

Table 4.1: Elemental compositions of pure BFO and 2 wt% NM-BFO nanocomposite.

Sample	**Elements weight (%)**						
	Bi	**Fe**	**O**	**Ag**	**Pt**	**Pd**	**Total**
Pure BFO	58.71	14.30	26.99	0	0	0	100
Ag-BFO	57.79	14.07	26.13	2.01	0	0	100
Pt-BFO	57.86	14.02	26.11	0	2.01	0	100
Pd-BFO	57.85	11.26	28.54	0	0	2.35	100

Moreover, the EDX mapping analysis can be used to investigate the presence of different elements in the selected region by showing different colour images. Figure 4.5 displays the elemental mapping analyses of 2 wt% NM-BFO nanocomposite. The EDX mapping showed a well distribution of the Bi, Fe and O elements in all of the 2 wt% NM-BFO nanocomposite. Besides, Ag, Pt and Pd elements were scattered throughout the 2 wt% Ag-BFO, 2 wt% Pt-BFO and 2 wt% Pd-BFO nanocomposite, respectively. This is another confirmation for the uniform spreading of all the elements in the synthesized photocatlysts.

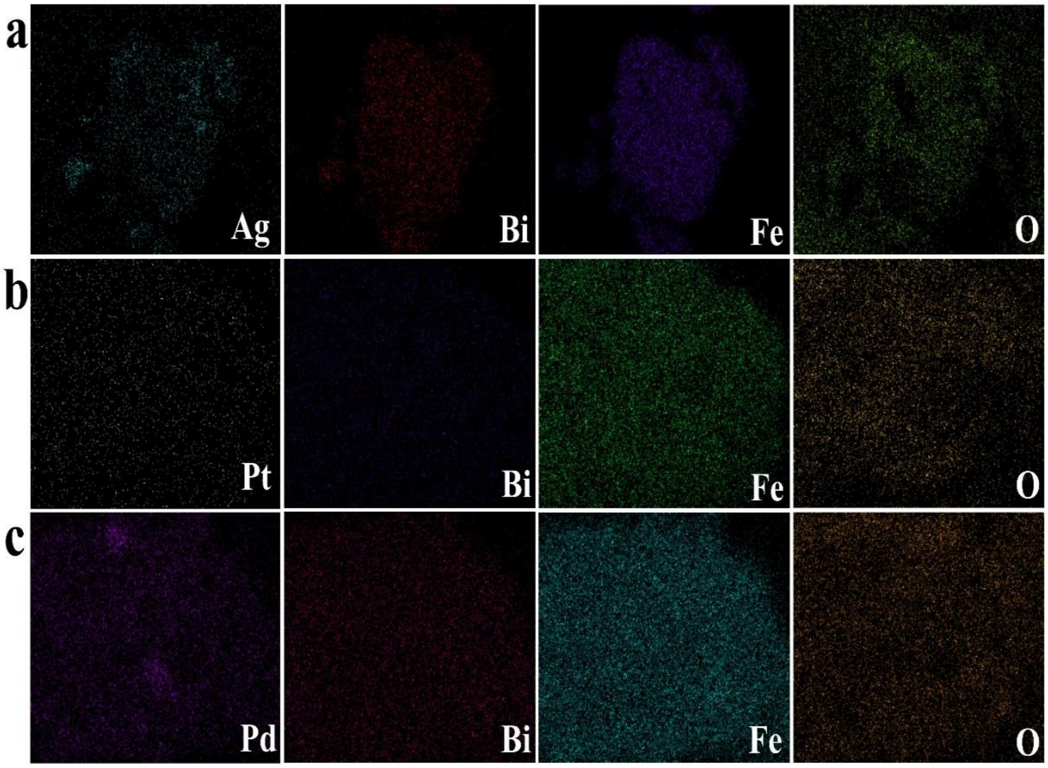

Figure 4.5: EDX mapping of **a** 2 wt% Ag-BFO nanocomposite **b** 2 wt% Pt-BFO nanocomposite and **c** 2 wt% Pd-BFO nanocomposite.

4.1.4 TEM analysis

To double confirmed the existence of NM nanoparticles on the coral-like BFO surface, TEM analysis was also executed on 2 wt% NM-BFO nanocomposite. Figure 4.6 displays the TEM images of the 2 wt% Ag-BFO, 2 wt% Pt-BFO and 2 wt% Pd-BFO nanocomposites. It can be observed that the doping of various NM didn't alter the coral-like morphology. The TEM images in Figures 4.6 a, c and e evidently same with the FESEM findings in terms of morphologies and dimensions. Moreover, spherical-shaped nanoparticles of various NMs were homogeneously dispersed on the entire coral-like BFO surface. Figures 4.6b, d and f depict the magnified TEM images of 2 wt% Ag-BFO, 2 wt% Pt-BFO and 2 wt% Pd-BFO nanocomposite, respectively. The magnified image of 2 wt% Ag-BFO nanocomposite in Figure 4.6b suggested that the metallic Ag were in the size ranging from 20 to 30 nm. For the 2 wt% Pt-BFO nanocomposite (Figure 4.6d), the Pt nanoparticles showed the particle were in the size ranging from 17 to 30 nm. On the other hand, the Pd nanoparticles diameter in the 2 wt% Pd-BFO nanocomposite (Figure 4.6f) were measured to be 15-25 nm.

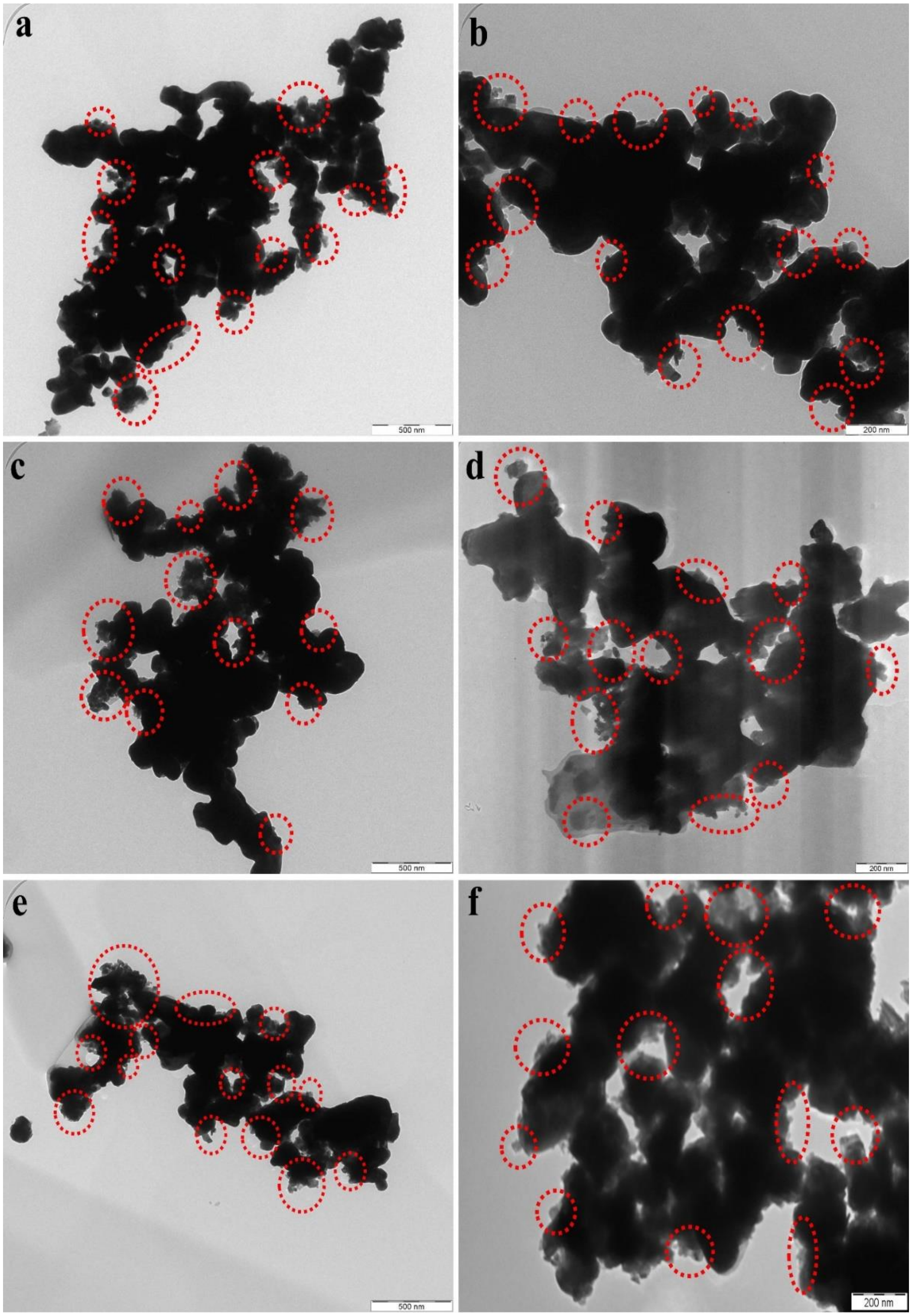

Figure 4.6: High and low magnification of TEM images of (a–b) 2 wt% Ag-BFO nanocomposite, (c–d) 2 wt% Pt-BFO nanocomposite and (e–f) 2 wt% Pd-BFO nanocomposite, respectively.

4.1.5 X-ray Photoelectron spectroscopy (XPS)

Chemical states and elemental chemical compositions of the 2 wt% Pd-BFO microcomposite were investigated using XPS analysis. The XPS spectrum for Bi *4f* is presented in Figure 4.7a. Two peaks appeared at 164.1 and 155.8 eV could be acknowledged as the binding energies of Bi $4_{f7/2}$ and Bi $4_{f5/2}$, respectively, confirming the form of bismuth (Bi^{3+}) in the Pd-BFO microcomposite (Zhao et al., 2015; Soltani & Lee., 2016). Figure 4.7b depicts the narrow scan XPS spectrum of Fe 2_p. Two peaks centered at 710.8 and 724 eV could be attributed to the Fe $2_{p3/2}$ and Fe $2_{p1/2}$ respectively, showing the interaction of a spin-orbital. Another peak around 718.8 eV, 8 eV above the main $2_{p3/2}$ peak could be associated as a typical Fe oxidation state (Yamashita et al., 2008; Lam et al., 2014). The presence of the satellite peak specified that the element Fe could be in the Fe^{3+} valance state on the microcomposite. The O 1_s spectrum in Figure 4.7c displayed that the two binding energies positioned around 529.6 and 530.6 eV could be credited to the oxygen-metal bond and surface adsorbed O_2, respectively (Deng et al., 2018). Moreover, the binding energies at 336.7 and 341.8 eV could be assigned to the metallic Palladium (Pd^0) as exhibited in Figure 4.8d (Seifvand et al., 2016; Meng & Zhang., 2017). The XPS findings further realized the presence of metallic Pd on the microcomposite, which was well consistent with the XRD findings.

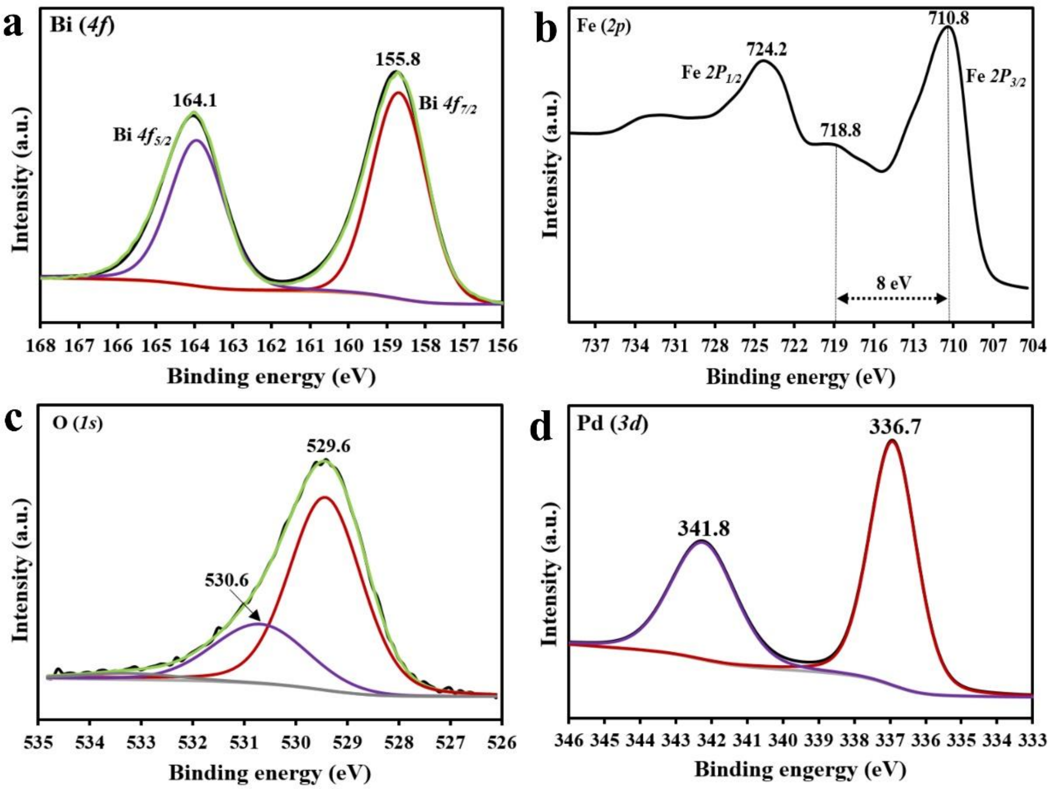

Figure 4.7. XPS spectra of 2 wt% Pd-BFO microcomposite (a) Bi 4f peaks, (b) Fe 2p peaks, (c) O 1s peaks and (d) Pd 3d peaks.

4.1.5 UV-vis DRS analysis

The optical characteristics of pure BFO and 2 wt% NM-BFO nanocomposite were investigated using UV-vis DRS spectra and the findings were displayed in Figure 4.8a. As compared with the pure BFO, the 2 wt% NM-BFO nanocomposites have prolonged their visible light absorption capabilities up to 800 nm. It was witnessed that the 2 wt% NM-BFO nanocomposites led to a red shift in the optical absorption edges. This phenomenon suggested that the NM-BFO nanocomposites can absorb more visible light, which would be beneficial in their photocatalytic activities (Wang et al., 2016a; Zhang et al., 2015). The E_g energies of the fabricated nanocomposite can be estimated by a graph between $((F(R)hv)^{1/2}$ vs $E(hv)$ via K–M function and E_g equations (Guy and Ozacar, 2016; Lam et al., 2018).

$$F(R) = (1-R)^2/2R \tag{4.1}$$

where $F(R)$, R, E_g, h_c, c and λ are *K-M* function, reflectance (%), energy band-gap (eV), Planck constant (4.135667×10^{-15} eVs), velocity of light (3×10^8 m/s) and onset absorption wavelength (nm), respectively. The calculated E_g values were 2.50, 2.30, 2.20 and 2.08 eV for pure BFO, 2 wt% Ag-BFO, 2 wt% Pt-BFO and 2 wt% Pd-BFO nanocomposites, respectively as shown in Figure 4.8b. The findings suggested that the E_g value of BFO can be simply tuned by adding the noble metals on the surface of BFO, which resulted in the improvement of visible light absorption as compared to that of pure BFO. The E_g values of pure BFO, which was determined in the current study was well consistent with the E_g values of BFO stated in the past literature (Di et al., 2017; Ilic et al., 2016; Lotey & Verma, 2014). Based on these findings, the reflectance properties suggested that the 2 wt% NM-BFO nanocomposites can be more effective in the visible light photocatalysis compared with that of the pure BFO.

The UV-vis DRS of different wt% Pd-loaded on BFO nanocomposites were also studied and results were displayed in Figure 4.9a. For comparison purposes, the UV-vis DRS spectrum of pure BFO was also included. The results presented that the loading of Pd had a strong influence on the light absorption properties of

BFO. It was also witnessed that the Pd-BFO nanocomposites also led to a red shift in the optical absorption edges. The E_g values were also calculated by plotting a tangent to the curve between $(F(R)hv)^{1/2}$ vs E_g as revealed in the Figure 4.9b. The estimated E_g values of the pure BFO, 0.5 wt% Pd-BFO, 1 wt% Pd-BFO, 2 wt% Pd-BFO and 3 wt% Pd-BFO nanocomposites were 2.50, 2.25, 2.18, 2.08, and 2.21 eV, respectively. The decrease in the E_g values can be credited to the Pd dopant, which might result in the improved visible light photodegradation activity. However, further increasing in the Pd loadings to 3 wt% led to an increase in the E_g value. This phenomenon could be credited to the excess amount of Pd nanoparticles on the surface of BFO, which reduced the penetrating ability of the incoming radiation, possibly scattering it (Michael et al., 2014).

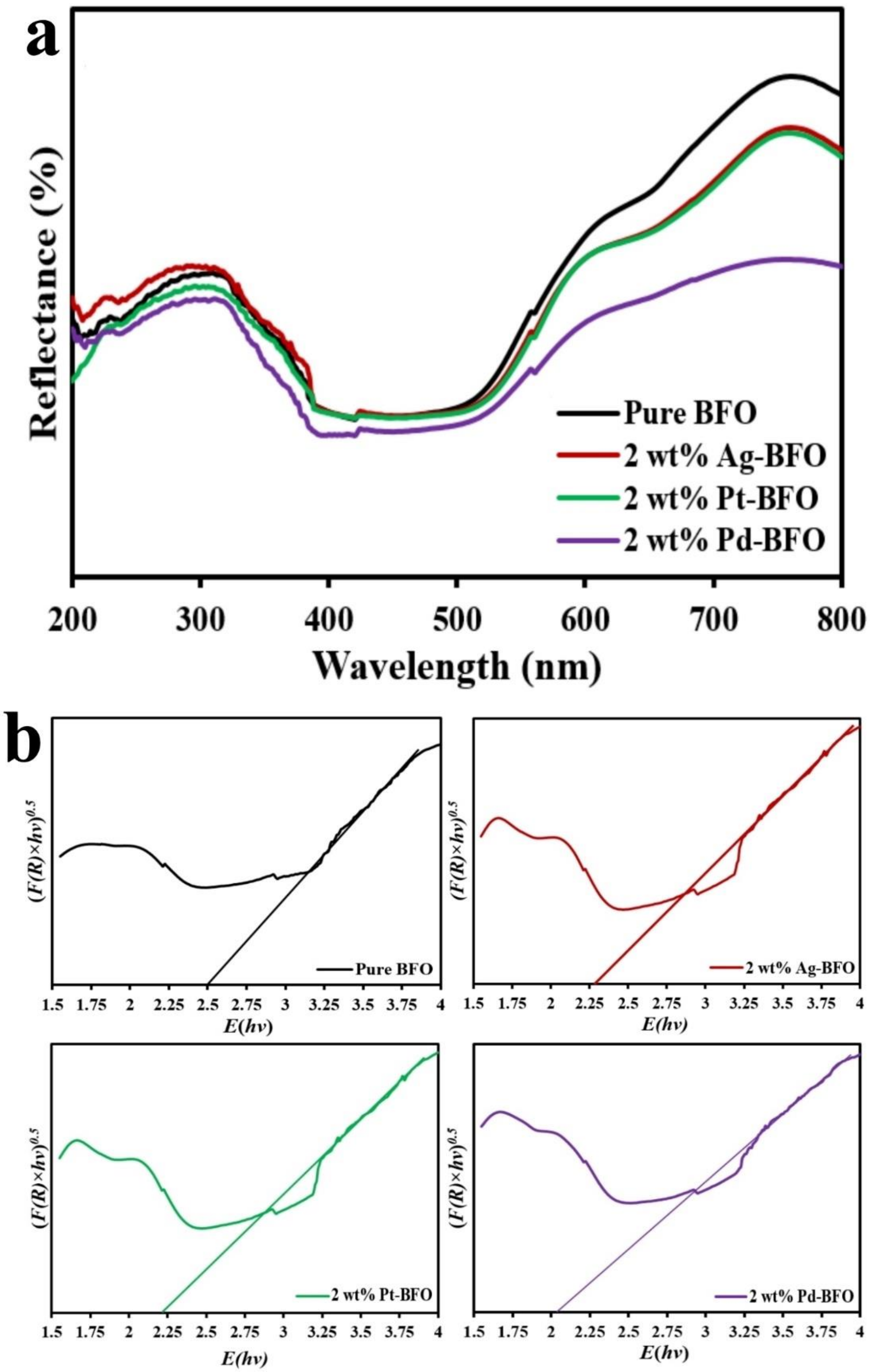

Figure 4.8: **a** UV–vis DRS spectra for pure BFO and 2 wt% NM-BFO nanocomposites and **b** plot of $(F(R)h\nu)^{1/2}$ vs the photon energy (E_g) of pure BFO and NM-BFO nanocomposites.

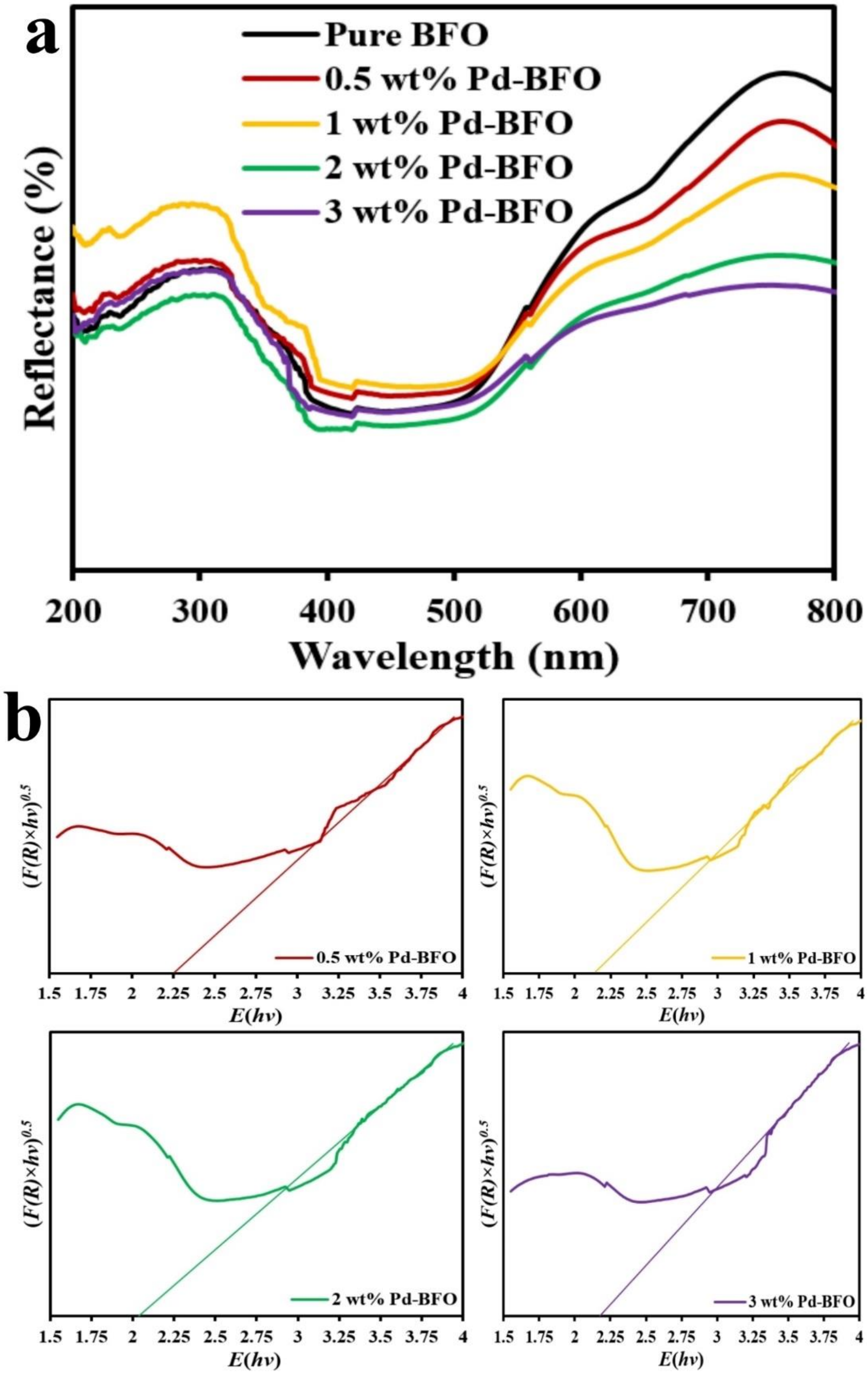

Figure 4.9: **a** UV–vis DRS spectra for pure BFO and Pd-BFO nanocomposites using various Pd wt% loadings and **b** plot of $(F(R)h\nu)^{1/2}$ vs the photon energy (E_g) of different wt% Pd-BFO nanocomposites.

4.1.6 PL analysis

The PL technique has broadly applied to study the charge carrier trapping, migration efficiency and to understand the lifetime of $e^{-}-h^{+}$ pairs in photocatalysts (Lotey & Verma, 2014; Wang et al., 2016a). Figure 4.10 depicts the PL spectra of pure BFO and 2 wt% NM-BFO nanocomposites at 325 nm excitation wavelength. It was observed that the PL intensities of NM-BFO nanocomposites displayed a dramatic decrease than those of the pure BFO. This phenomenon could be discussed by the existence of different noble metals on coral-like BFO can act as an e^{-} trapping site, which can capture the e^{-} and ultimately enhanced the $e^{-}-h^{+}$ pair separation efficiency (Song et al., 2018; Wang et al., 2018). Among the different 2 wt% NM-BFO nanocomposite, the PL spectrum of 2 wt% Pd-BFO nanocomposites exhibited the lowest intensity, indicating the highest $e^{-}-h^{+}$ pairs separation efficiency. Therefore, the PL results suggested that the 2 wt% Pd-BFO nanocomposites could have good heterojunction interfaces between Pd and BFO for interfacial charge carrier transfer during the photocatalytic reaction.

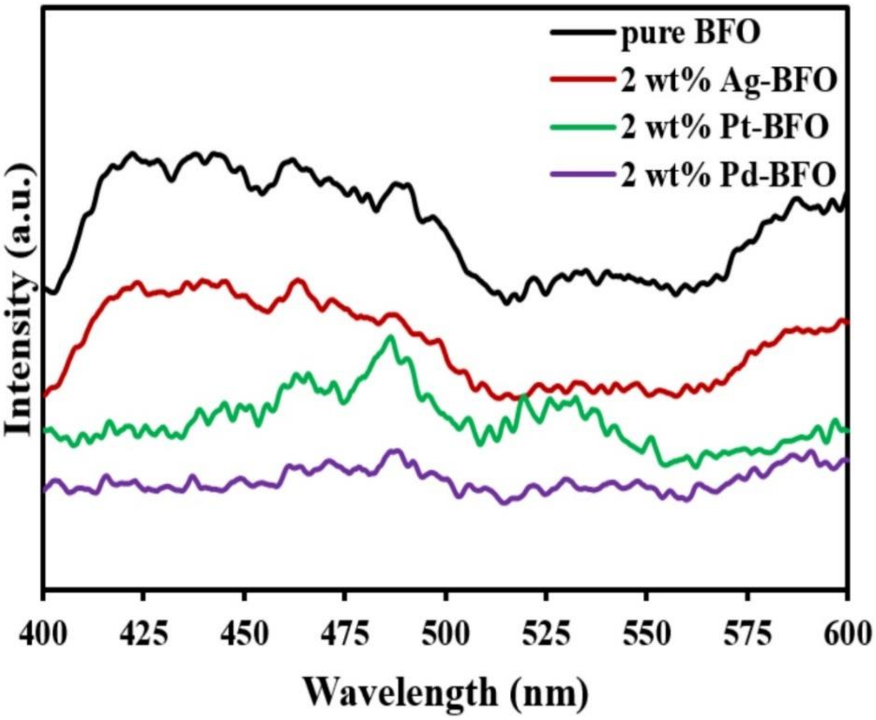

Figure 4.10: PL spectra of pure BFO and 2 wt% NM-BFO nanocomposites.

Figure 4.11 displays the PL spectra of pure BFO and various Pd loadings on BFO nanocomposites. It was witnessed that the pure BFO had the highest emission intensity, while 2 wt% Pd-BFO nanocomposite showed the least intensity among all nanocomposites. Tao et al., (2016) stated that a lower emission intensity would suggest a lower e^{-}–h^{+} recombination rate, whereas higher emission intensity would be helpful in fast e^{-}–h^{+} recombination. As presented in Figure 4.10, all the Pd-BFO nanocomposites exhibited the same PL shapes as shown in Figure 4.9. Additionally, the PL intensities of Pd-BFO nanocomposites were varied by the altering of Pd loading contents. It can be seen that the loading of Pd nanoparticles had a strong tendency to act as an e^{-} trapping site, which accelerates the interfacial charge migration, hence, enhance the lifetime of photogenerated e^-–h^+ pairs (Song et al., 2018; Wang et al., 2018; Wei and Gao, 2015). On the other hand, when Pd loading was enhanced from the optimum contents such as 3 wt% Pd-BFO nanocomposite, the PL intensity again increased. This phenomenon can be credited to the production of Pd clusters, which led to weaken the Pd attachment with the coral-like BFO and eventually, improved the of e^-–h^+ pairs recombination (Jaffari et al., 2019; Zhao et al., 2017).

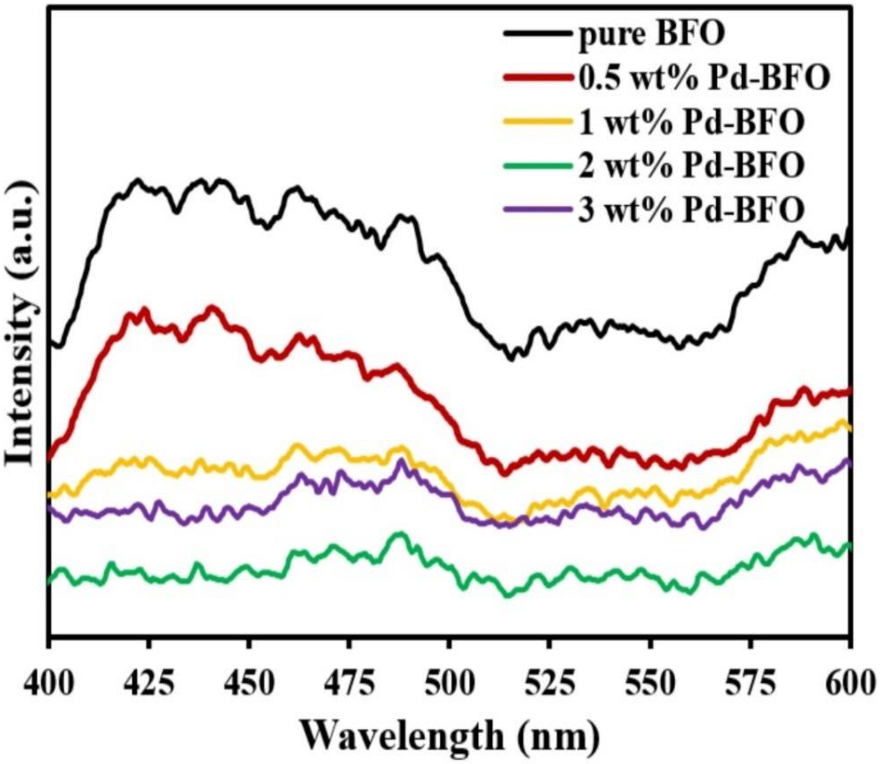

Figure 4.11: PL spectra of pure BFO and Pd-BFO nanocomposites at varied wt% Pd loadings.

4.1.7 FTIR analysis

The functional groups of pure BFO and 2 wt% NM-BFO were also studied using FTIR analysis and results were shown in Figure 4.12. In FTIR spectra, the characteristic peaks around 452 cm^{-1} and 556 cm^{-1} could be related with the Fe-O-Fe bending and Fe-O stretching vibration of the FeO_6 octahedral perovskite structure, respectively, which confirmed the synthesis of BFO (Wang et al., 2014; Chen and Ting, 2017; Ramezanalizadeh and Manteghi, 2017). Apart from the main characteristic peaks of BFO, the weak intensities around 2867 and 2933 cm^{-1} can be credited to the symmetric and asymmetric stretching of the C−H bond, respectively (Shahini & Ashkarran, 2018). In the case of Pt-BFO nanocomposite, the weak-to-medium bands in the region 600–720 cm^{-1} were also found accredited to the presence of metallic Pt (Jaffari et al., 2019; Tahir et al., 2017). As for the Ag-loaded BFO nanocomposite, an intense peak around 590–800 cm^{-1} could be credited to the metallic Ag vibration (Jaffari et al., 2019; Xu et al., 2013), while no additional peak for Pd was identified in the spectrum of Pd-BFO nanocomposite. Gao et al., (2017) synthesized YVO_4/g-C_3N_4/Ag nanoparticles using hydrothermal followed by a photodeposition method and characterized the crystal structure and functional groups using XRD and FTIR analyses, respectively. The FTIR spectra detected the presence of metallic Ag at the bend located around 620-670 cm^{-1}. However, their XRD patterns were also unable to identify the Ag crystal phase, which they attributed to the small Ag contents. Moreover, the absorption bands around 3410 cm^{-1} and 1610 cm^{-1} could be allocated to the bending of the –OH group and H_2O molecules strongly adhered to the photocatalyst surface (Abou et al., 2017; Shahini & Ashkarran, 2018). The presence of –OH groups could be helpful for the pollutant degradation as they can seize the h^+ and eventually generate •OH radicals with high oxidation ability.

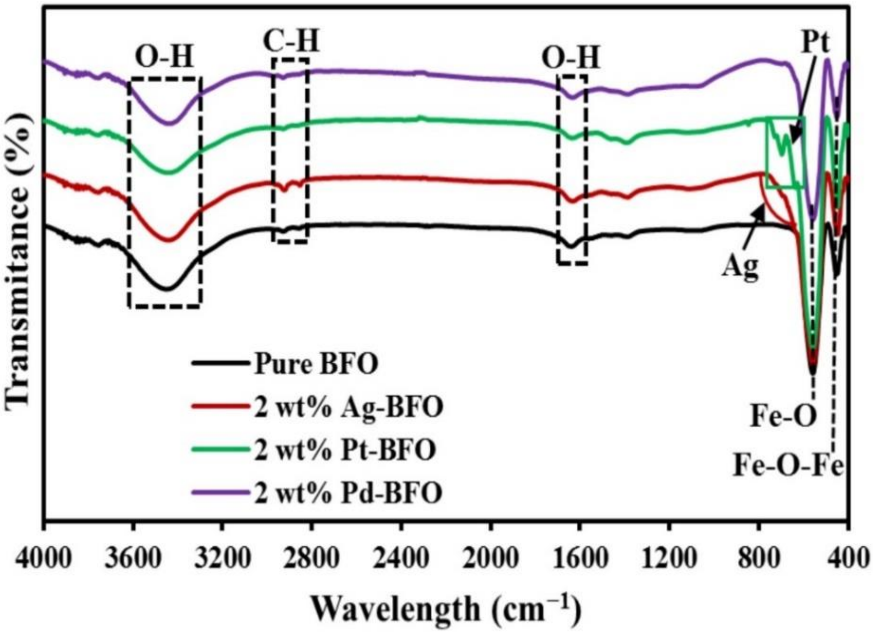

Figure 4.12: FTIR spectra of pure BFO and 2 wt% NM-BFO nanocomposites.

Figure 4.13 displays the FTIR spectra of pure BFO and different wt% loading contents of Pd-BFO nanocomposites. The FTIR spectra of Pd-BFO nanocomposites were almost identical to that of the pure BFO. However, with the closer look, the FTIR peak intensities showed a decrease in the main characteristic bands with the increase in Pd loading contents, implying that the BFO framework was partially altered by Pd loading (Meng & Zhang, 2017). Two small bends around 2867 and 2933 cm^{-1} were also appeared, which can be credited to the symmetric and asymmetric stretching of C−H bond, respectively (Shahini &

Ashkarran, 2018). The peaks appeared at 1610 cm^{-1} and 3410 cm^{-1} were credited to the absorbed H_2O molecules and O−H stretching mode of OH^- groups on the Pd-BFO nanocomposites, respectively (Jaffari et al., 2019; Quek et al., 2018).

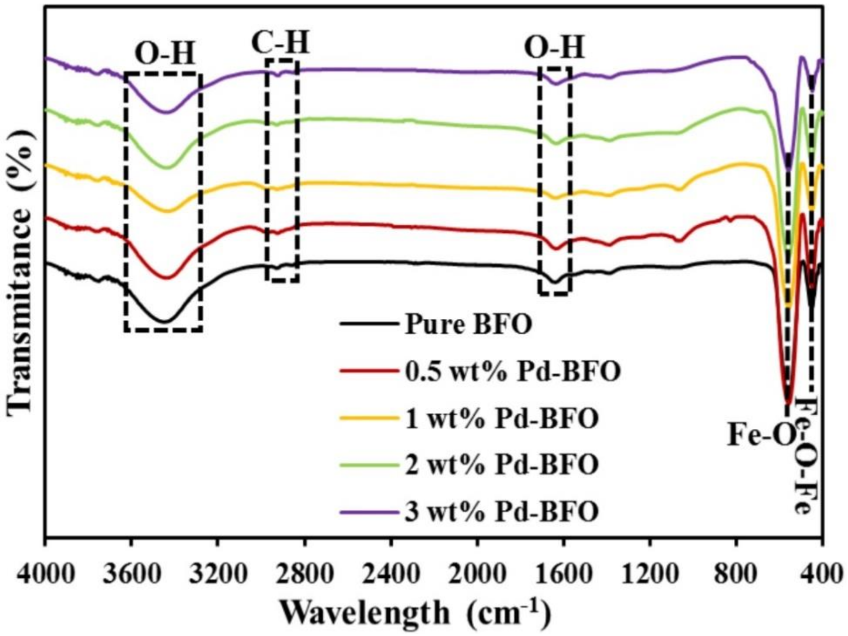

Figure 4.13: FTIR spectra of pure BFO and Pd-BFO nanocomposites at different wt% Pd loadings.

4.1.8 Magnetic hysteresis (M-H) loop

The magnetic hysteresis (M-H) loop was applied to study the magnetic properties of pure BFO and 2 wt% NM-BFO nanocomposites. Figure 4.14 presents the M-H loop for the pure BFO and 2 wt% NM-BFO nanocomposites. The saturation magnetization values for pure BFO, 2 wt% Ag-BFO, 2 wt% Pt-BFO and 2 wt% Pd-BFO nanocomposites were around 4.84, 2.30, 2.78 and 4.06 emu/g, respectively. The magnetic properties of NM-BFO nanocomposites were weakened than those of the pure BFO catalyst, which might be due to the incorporation of metallic noble metals on the BFO surface. However, the M-H loop values of NM-BFO nanocomposites were still found to be higher than those of the other doped BFO literature reports (Chandra & Manoj, 2015; Cheng et al., 2017; Gong et al., 2013b). The magnetic properties of NM-BFO nanocomposites can have the practical application during the recycling test. The magnetic separation of 2 wt% Pd-BFO nanocomposite was investigated by placing a small magnet near a glass bottle containing the nanocomposite as displayed in Figure 4.15. The suspended particles were attracted near the magnet, which revealed its convenient magnetic separation after used. This magnetic separation technique will be very useful during the recycling studies.

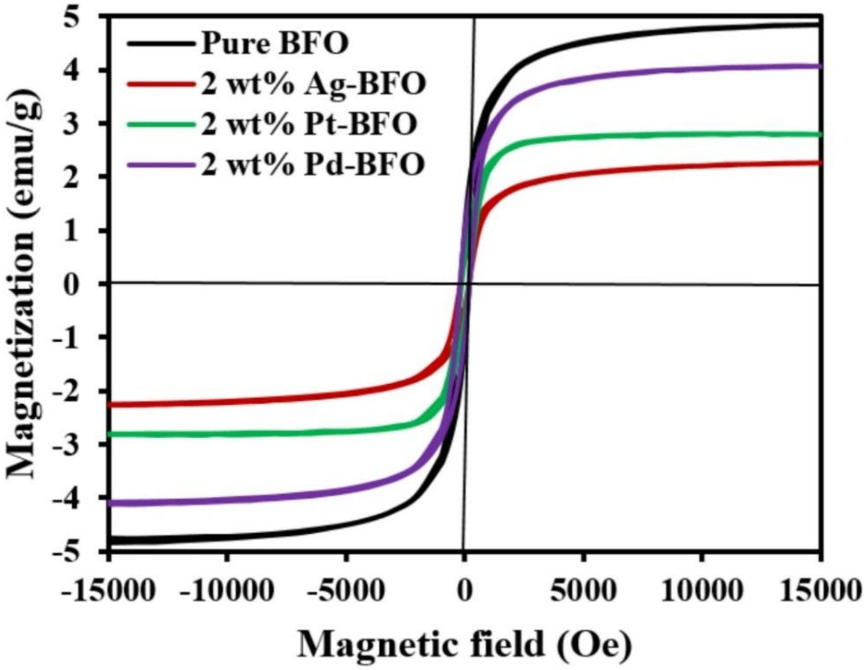

Figure 4.14: Room temperature M−H loop on pure BFO and 2 wt% NM-BFO nanocomposites.

Figure 4.15: separation of 2 wt% Pd-BFO nanocomposite with the help of an external magnetic field.

4.1.9 Characterizations of recycled Pd-BFO nanocomposite

The stability of reused Pd-BFO nanocomposite was also analyzed. Figure 4.16 clearly shows that the XRD pattern of recycled Pd-BFO nanocomposite was almost unchanged, suggesting the high structural crystallinity. Moreover, the coral-like Pd-BFO morphology was well maintained under the microscopic image as recorded in Figure 4.17. Figures 4.18a-d depict the results of EDX mapping on recycled Pd-BFO nanocomposite. The results demonstrated that the Pd, Bi, Fe and O elements were dispersed on the Pd-BFO. Thus, the synthesized magnetic Pd-BFO nanocomposite can be regarded as a promising candidate of recyclable and stable catalysts in eliminating the environmental organics during the practical applications.

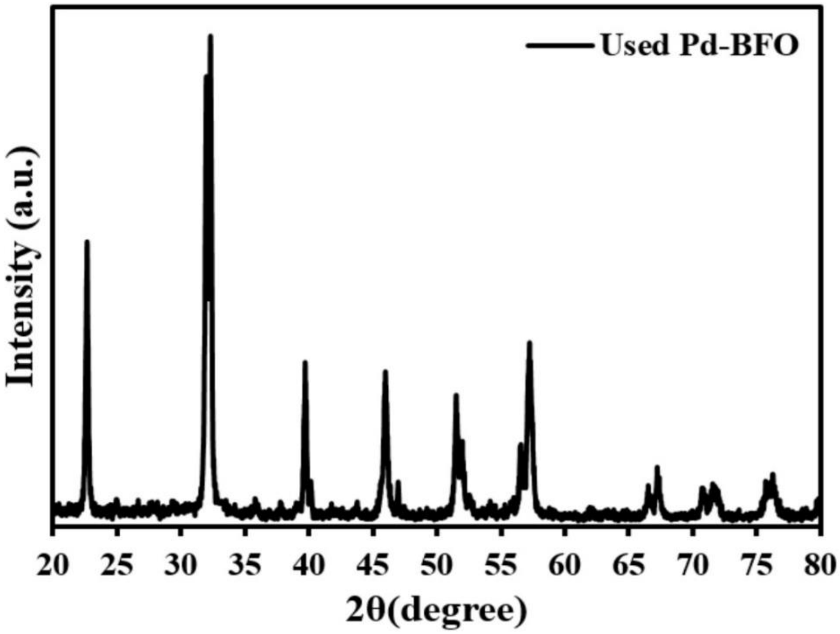

Figure 4.16: XRD pattern of recycled 2 wt% Pd-BFO nanocomposite.

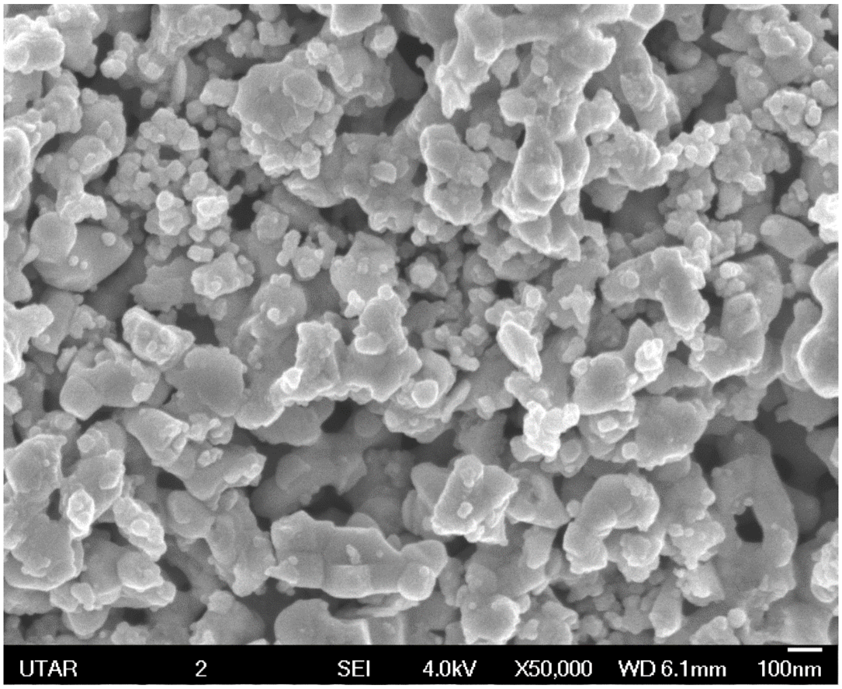

Figure 4.17: FESEM image of recycled 2 wt% Pd-BFO nanocomposite.

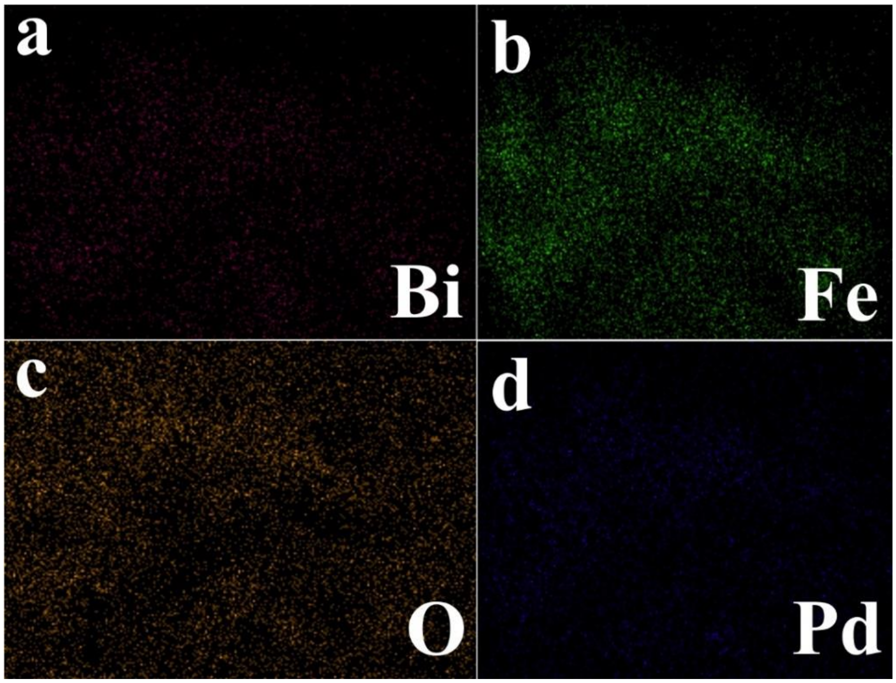

Figure 4.18: EDX mapping of recycled 2 wt% Pd-BFO nanocomposite **a** Bi, **b** Fe, **c** O and **d** Pd.

4.2 Photodegradation of malachite green (MG) dye using NM-doped BFO photocatalysts under visible light

The photoactivities of the as-synthesized coral-like BFO and 2 wt% NM-BFO nanocomposites were investigated by degradation of MG dye in aqueous solution using photocatalyst dosage of 1 g/L, initial MG concentration of 10 mg/L and at natural solution pH under visible light irradiation. The comparative studies using 2 wt% NM-BFO nanocomposites were also performed in order to validate the photocatalytic activities. Figure A-1 shows the results of photolysis and dark adsorption studies. The results stated that the MG dye concentration was hardly reduced when it was irradiated under visible light in the absence of the photocatalyst. It suggested that the MG dye was stable during the photolysis experiment. On the other hand, under dark adsorption conditions, the MG dye was 12.3%, 13.5% and 15.7% removed using 2 wt% Ag-BFO, 2 wt% Pt-BFO and 2 wt% Pd-BFO nanocomposites, respectively. The results presented that the as-synthesized NM-BFO nanocomposites did not showed removal efficiencies in the absence of light irradiation. Similar findings on photolysis and dark absorption were also stated in the literature (Kaur et al., 2016; Navjot et al., 2017; Niu et al., 2015b).

Compared with the above stated experiments, the photodegradation of MG dye was highly improved in the presence of pure BFO and 2 wt% NM-BFO nanocomposites under visible light irradiation. Figure 4.19 depicts the photocatalytic activities of pure BFO and 2 wt% NM-BFO nanocomposites towards the degradation of MG dye. The MG dye degradation efficiency reached to 72.2% over pure BFO after 240 min of light irradiation. Among the 2 wt% NM-BFO nanocomposites, the Pd-BFO nanocomposite presents the best degradation efficiency of 96.4% in 240 min, which was approximately 1.33 times greater than that of the pure BFO. The Pt-BFO and Ag-BFO nanocomposites also showed the high MG dye degradation efficiencies of around 94.8% and 82.8%, respectively.

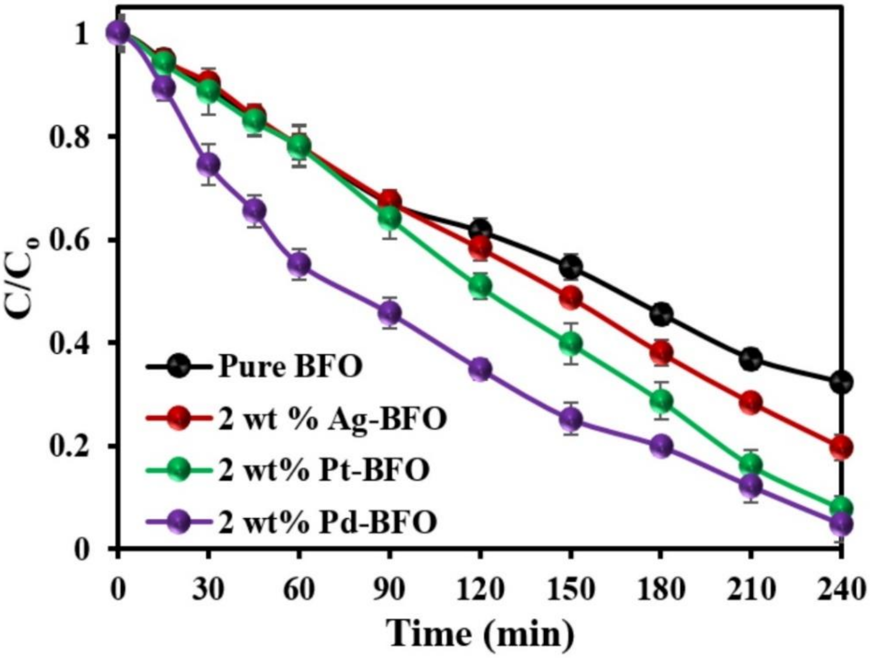

Figure 4.19: Photodegradation of MG dye over pure BFO and 2 wt% NM-BFO nanocomposite ([MG] = 10.0 mg/L; photocatalyst dosage = 1.0 g/L; pH = 5.45).

The photodegradation performance of the nanocomposites highly depended on different factors such as band gap energy, crystallinity and phase purity, morphology and the photogenerated $e^{-}-h^{+}$ pairs separation efficiency (Guy and Ozacar, 2016; Quek et al., 2018; Lam et al., 2018). It can be clearly seen that the 2 wt% NM-BFO nanocomposites exhibited enhanced photocatalytic activities than those of the pure BFO. Taking the results of EDX, EDX mapping, UV-vis DRS and PL characterizations into account, it can be established that the excellent photocatalytic activities of 2 wt% NM-BFO nanocomposite were associated with the high dispersion of NM nanoparticles on BFO surface, smaller E_g values and lower photogenerated $e^{-}-h^{+}$ pairs recombination (Caux et al., 2017; Dong et al., 2016; Patil et al., 2016). As discussed in the DRS analysis, the loading of NM on coral-like BFO surface can enhance the light absorption abilities to the higher wavelength, which led to a decline in E_g values. The decreased band gap energy values of 2 wt% NM-BFO nanocomposites were highly benefitted to the improved absorption of the visible light (Benyounes et al., 2015; Jaffari et al., 2019b). Besides, the presence of NM on BFO surface can also cause an improvement in the migration of photogenerated $e^{-}-h^{+}$ pairs, which instigated enhancement in the photocatalytic activities. The photocatalytic activity findings were in accordance with the PL analysis (Figure 4.9). The 2 wt% Pd-BFO nanocomposite with the lowest PL intensity showed the highest photodegradation performance among other nanocomposites. Moreover, the improved migration of photogenerated $e^{-}-h^{+}$ pairs would cause more h^{+} to react with the hydroxyl ions (OH^{-}) to generate the •OH radicals. The –OH group was also witnessed on NM-BFO nanocomposite surface using the FTIR analysis (Figure 4.11). The generated •OH radicals are an extremely strong oxidizing agent, which has a high tendency to degrade a large number of hazardous organic pollutants into small nonhazardous or less hazardous chemical compounds (Bharathkumar et al., 2015; Chen et al., 2019; Gou et al., 2018). Hence, the generation of •OH radicals might be an important factor for improved photocatalytic activities. In summary, the improved photocatalytic activities of 2 wt% NM-BFO nanocomposites over pure BFO was the collective efforts of decreased band gap energy values, enhanced separation of photogenerated $e^{-}-h^{+}$ pairs and the large quantity of •OH radicals generations.

4.2.1 Effect of NM loadings

The photocatalytic activities of NM-loaded BFO nanocomposites with various NM loadings were also investigated for the degradation of MG dye under visible light irradiation. The effect of various NM loadings towards the MG dye degradation was performed using constant photocatalyst dosage of 1 g/L, initial MG dye concentration of 10 mg/L and at natural solution pH under 105 W visible light.

Figure 4.20 depicts the photodegradation performance of the Ag, Pt and Pd-loaded BFO nanocomposites with various wt% NM loadings towards the degradation of MG dye under visible light irradiation. The photocatalytic results revealed that all the NM-BFO nanocomposites exhibited higher degradation efficiencies compared with the pure BFO. The photocatalytic activities of the NM-BFO nanocomposites first improved with increasing the NM loadings until the optimum value and then declined with the further enhancing the NM loadings. The optimum loadings of Ag, Pt and Pd on the coral-like BFO were recorded at 3 wt%, 0.5 wt% and 2 wt%, respectively.

The enhanced photodegradation performance were credited to the appropriate loadings of metallic NM on the BFO surface, which can increase the separation efficiency of photogenerated $e^{-}-h^{+}$ pairs. Moreover, the greater photodegradation can also credited to the longer life time of the photogenerated $e^{-}-h^{+}$ pairs, which was helpful to generate large number of reactive oxygen species such as $\bullet O_2^{-}$, $\bullet OH$ radicals and H_2O_2 to participate in the MG dye degradation reaction (Guo et al., 2018; Sun et al., 2018; Zhang et al., 2018). Meng and Zhang, (2017) reported that the Pd-Bi_2MoO_6 nanocomposites with 2 wt% Pd loadings exhibited the highest photocatalytic activity towards the phenol degradation. Niu et al., (2016) also discovered that the 3 wt% Ag-loading were the appropriate amount on the surface of g-C_3N_4 semiconductor.

On the other hand, when further increasing in NM contents more than the optimum level, the photocatalytic performance decreased to some extent. This phenomenon can be associated with the higher contents of metallic NM on the BFO surface, which might reduce the quantity of active sites on the BFO surface. As presented in the FESEM image (Figure 4.3), the tendencies of Pd nanoparticles in the aggregated form on the coral-like BFO surface were higher at excessive Pd loadings. For instance, Wang et al., (2017) synthesized nanofiber shaped Ag-TiO_2 nanocomposite and applied towards the degradation of RhB dye. Their findings also suggested that the higher Ag loading caused a decrease in the contact between the Ag-TiO_2 photocatalyst and RhB dye solution, which consequently led to a decline in the generation of reactive oxygen species. Similar findings were also stated in the literatures (Xiao et al., 2017; Zheng et al., 2017; Wen et al., 2018). Therefore, appropriate metallic NM loadings should be introduced on the BFO surface to improve the photodegradation activity.

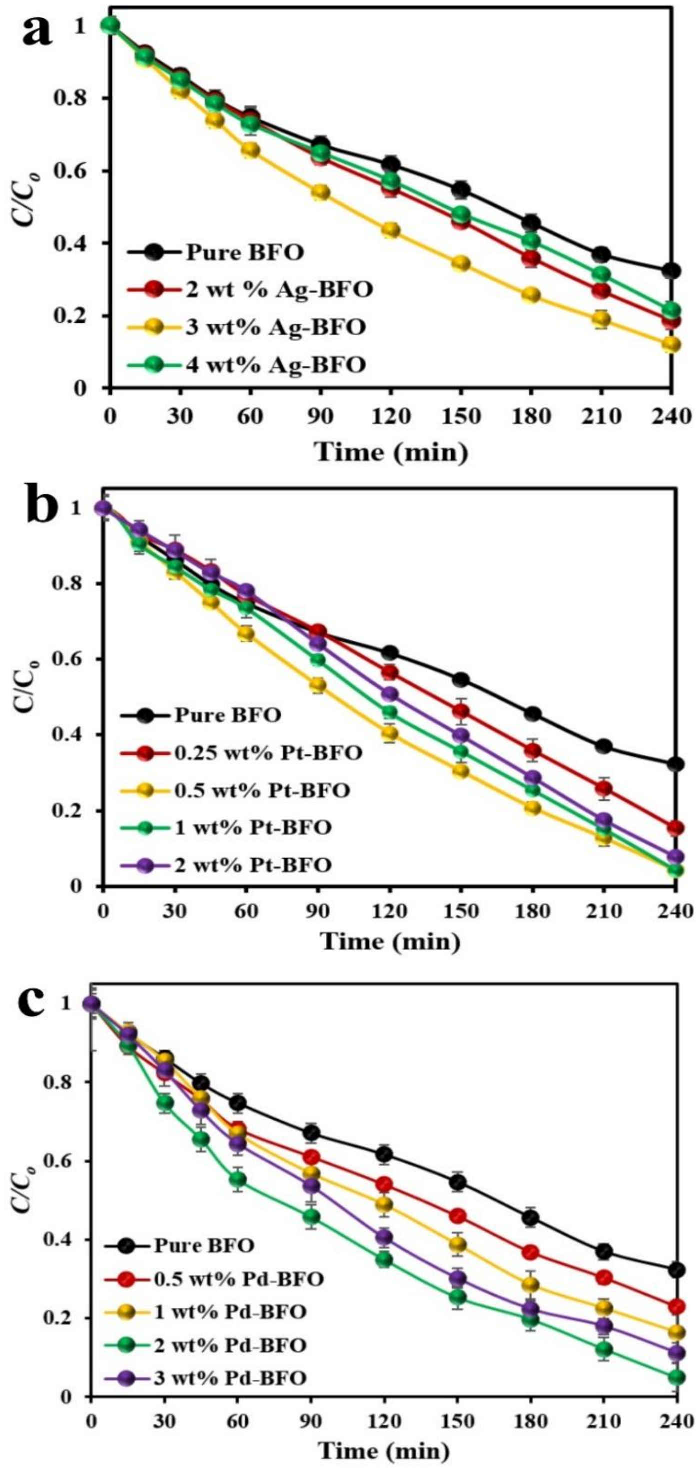

Figure 4.20: Photodegradation of MG dye over NM-BFO nanocomposites with various NM loadings of **a** Ag **b** Pt and **c** Pd (Light intensity = 105 W; [MG] = 10.0 mg/L; photocatalyst dosage = 1.0 g/L; pH = 5.45).

4.3 Photodegradation mechanism for the NM-doped BFO nanocomposite

4.3.1 Photoelectrochemical measurements

The photogenerated $e^{-}-h^{+}$ pairs separation and transfer efficiency were investigated using photoelectrochemical measurements. Figure 4.21 presents the photocurrent response for pure BFO and 2 wt% NM-BFO nanocomposite. Generally, a higher photocurrent intensity suggested a better $e^{-}-h^{+}$ pairs separation efficiency under visible light irradiation. As shown in Figure 4.21, 2 wt% Pd-BFO nanocomposite presents a higher photocurrent intensity than those of the pure BFO, 2 wt% Ag-BFO and 2 wt% Pt-BFO nanocomposite. This higher photocurrent intensity proved that the Pd-BFO nanocomposite possessed a higher photocatalytic ability, which can be credited to the better e^{-} scavenging ability of metallic Pd as compared with Ag and Pt (Meng & Zhang, 2018; Zhang 2019).

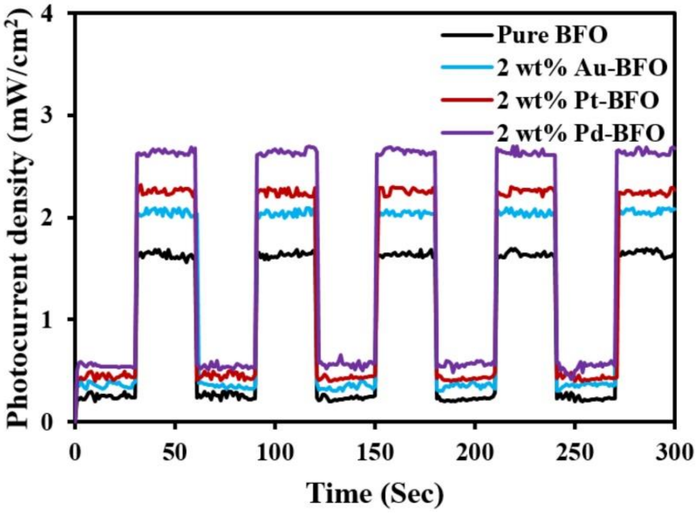

Figure 4.21: Transient-photocurrent curves for the pure BFO and 2 wt% NM-BFO microcomposite in 0.5M Na_2SO_4 electrolyte solution under visible light irradiation.

The electrochemical impedance spectroscopy (EIS) Nyquist plot was performed to further demonstrate the charge transfer behaviour. Figure 4.22 shows a significant decrease in the arc radius after the incorporation of metallic Pd on the surface of BFO as compared with the other photocatalysts. Generally speaking, a smaller arc radius means a lower resistance to the charge transfer with accelerated e^{-} transfer (Rasalingam et al., 2019; Mohamed et al., 2016). Hence, the Pd-BFO nanocomposite presents the most effective $e^{-}-h^{+}$ pairs separation efficiency. In other words, the Photoinduced current measurement and EIS Nyquist plots suggested that the 2 wt% Pd-BFO nanocomposite had the lowest $e^{-}-h^{+}$ pairs recombination rate, which promotes the photocatalytic abilities of Pd-BFO nanocomposites.

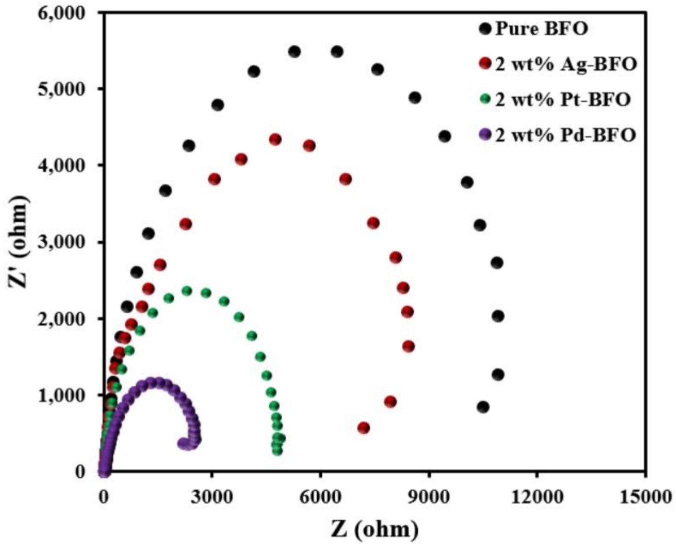

Figure 4.22: EIS Nyquist plot of pure BFO and 2 wt% NM-BFO nanocomposite.

4.3.2 Role of reactive species

Normally, the photocatalytic reaction involved different active oxidizing species such as h^+, $\bullet OH$, $\bullet O_2^-$ radicals and H_2O_2 to effectively degrade the organic pollutants (Chen et al., 2018; Gao et al., 2018; Bai et al., 2019). Therefore, numerous experiments were executed with and without radical scavengers under visible light to determine the role of reactive species in the MG dye degradation process over 2 wt% Pd-BFO nanocomposites. In the radical scavenger experiments, IPA was added to the system as $\bullet OH$ scavenger, BQ was utilized to scavenge the $\bullet O_2^-$, KI was applied as a scavenger for h^+ and catalase were applied as scavenging agents for H_2O_2. The MG dye degradation efficiency would be suppressed as a consequence of scavenging. The extent of decline in the photodegradation efficiency produced by these trapping agents would eventually tell the significance of their respective active species. The radical scavenger experiments were performed using light intensity of 105 W, photocatalyst dosage of 1.0 g/L, initial MG dye concentration of 10 mg/L and at natural solution pH.

Figure 4.23 depicts the MG dye photodegradation efficiencies after introducing different scavengers in the photocatalytic system. The results displayed that the degradation efficiencies were clearly suppressed in the existence of different scavengers. As displayed in Figure 4.18, when KI was inserted into the reaction mixture, the efficiency of MG dye decreased from 95.6% to 41.4%, suggesting that the h^+ was one of the main active species. The MG dye degradation efficiency was also restrained from 95.6% to 44.2% in the presence of catalase, signifying the importance of H_2O_2 in the photocatalytic process. Similarly, when IPA was introduced in the system, the removal efficiency was also inhibited to the 53.4%, showing that the •OH radicals were also important for the MG degradation. However, the addition of BQ exerts little influence on the MG degradation, which revealed that $\bullet O_2^-$ radical had the minor effect on the degradation process. These results clearly stated that MG degradation via Pd-BFO nanocomposites was mainly happened because of the collective efforts of •OH radicals, h^+ and H_2O_2.

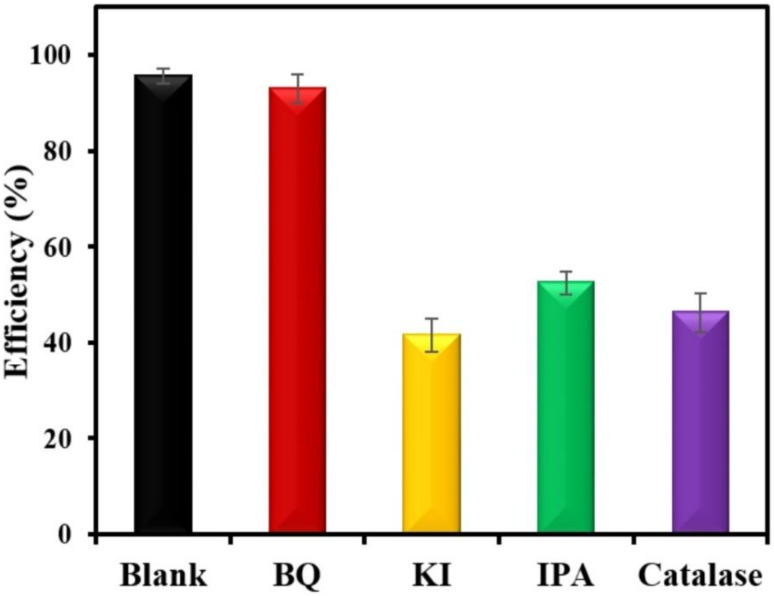

Figure 4.23: Radical scavenger study for active species during the photodegradation of MG dye using Pd-BFO nanocomposite. (Light intensity = 105 W; [MG] = 10.0 mg/L; photocatalyst dosage = 1.0 g/L; pH = 5.45).

4.3.2 Hydroxyl (•OH) radical generation analysis

According to the above-stated results, •OH radical was one the main active species for the MG dye degradation. Therefore, the production of •OH radicals on the visible light irradiated Pd-BFO nanocomposites was further established by the TA-PL test. The terephthalic acid has the ability to react with the •OH radicals in the aqueous solution and converted into the 2-hydroxyterephtalic acid (2-HTA), which was a highly fluorescent product. In the TA-PL experiment, the emergence of the peaks about 425 nm exposed the presence of 2HTA, which was formed by the chemical reaction among the TA and •OH radicals produced by the photocatalysts. Hence, the peak intensity represented the amount of •OH radical generation in the system. The experiment procedure was almost similar to the photocatalytic experiment except the MG dye was replaced with the terephthalic acid solution with the concentration of 5×10^{-4} M.

Figure 4.24 a presents the PL results of different pure BFO and 2 wt% NM-BFO nanocomposites excited at 315 nm. All the NM-BFO nanocomposites displayed higher PL intensities as compared to the pure BFO, which suggested that the loading of NM nanoparticles on the surface of BFO was a good route to improve the e^- and h^+ production, which resulted in the enhanced •OH radical generation. Moreover, the 2HTA intensities of NM-BFO nanocomposites were also varied with the different NM loadings. The 2 wt% Pd-BFO nanocomposite generate the highest peak intensity of 2HTA. This could be attributed the effective photogenerated

$e^{-}-h^{+}$ pair separation as well as the maximum production of •OH radicals. These results were also well matched with the PL spectra and NM-BFO photocatalytic activities. In addition, the 2HTA spectral changes with the irradiation time for the case of 2 wt% Pd-BFO nanocomposites (Figure 4.24b). Progressive enhancement in the PL intensities was recorded with increasing irradiation time, suggesting that the fluorescence was produced by the chemical reaction between the formed •OH radicals and TA during photo-illuminated reactions (Bharathkumar et al., 2015; Jaffari et al., 2019). Hence, these results further proved that •OH radicals were indeed generated and partook in the MG photodegradation.

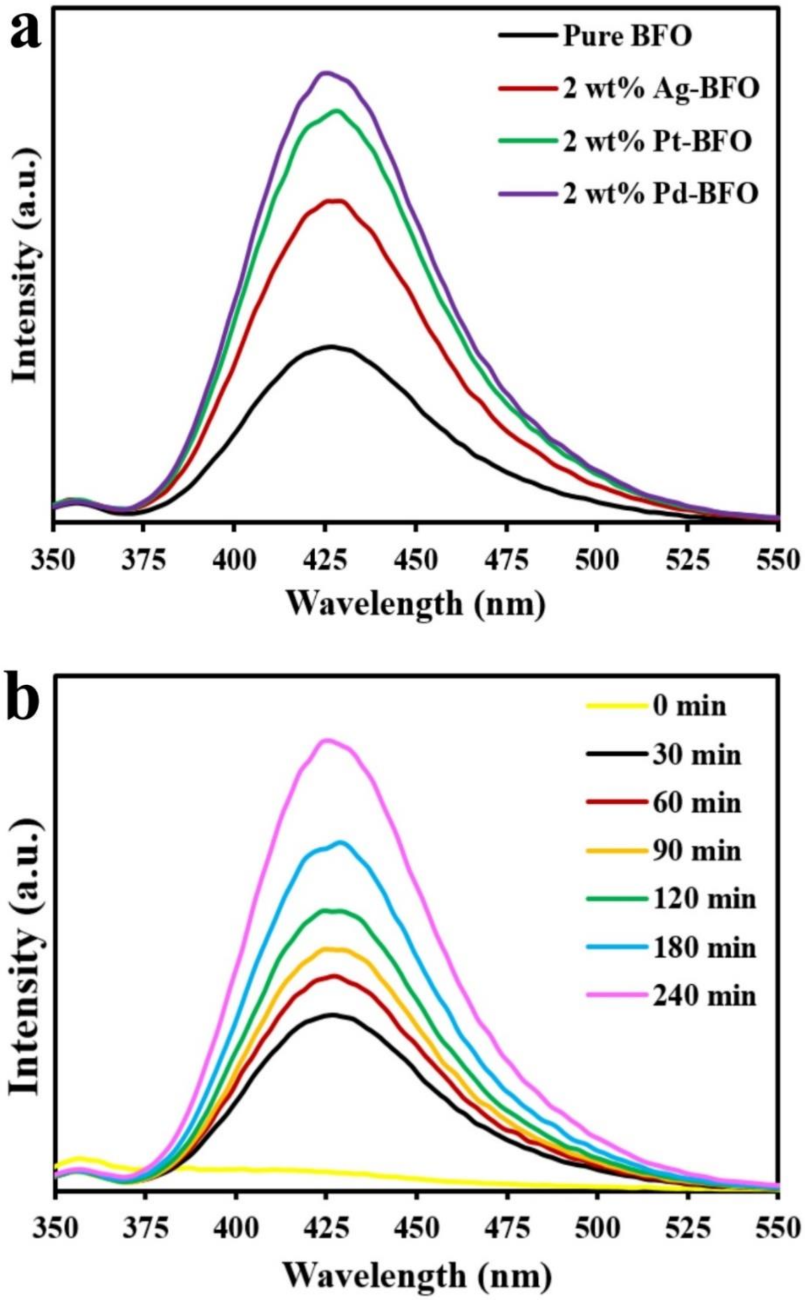

Figure 4.24: **a** TA-PL spectra of the TA solution at 315 nm excitation wavelength over pure BFO and 2.0% NM-BFO nanocomposite and **b** TA-PL spectral changes with the irradiation time for the case of 2 wt% Pd-BFO nanocomposite.

4.3.3 Proposed photodegradation mechanism

A possible mechanism for the separation of photogenerated $e^{-}-h^{+}$ pairs and photodegradation reaction over 2 wt% NM-loaded BFO nanocomposites were exhibited in Figure 4.25. Under visible light irradiation, the e^{-} of BFO was excited and moved from *VB* to *CB*, leaving the equal amount of h^{+} in the *VB*. The presence of NM on the surface of BFO would trapped the e^{-} form *CB* of BFO and inhibits the $e^{-}-h^{+}$ pairs recombination. The NM was acting as trapping agents to generate more H_2O_2 and meanwhile, the h^{+} present in *VB* of BFO react with the H_2O molecules and produce another highly reactive •OH radical. Ultimately, the H_2O_2 and •OH radicals attacked on the organic pollutants and mineralize them to the CO_2 and H_2O molecules.

According to the photodegradation experiments, 2 wt% Pd-BFO nanocomposite exhibited the highest photocatalytic activity compared with the other NM-loaded BFO nanocomposites. When the metallic Ag, Pt and Pd nanoparticles contacted with the semiconductor BFO, they will induce bending of the energy level in BFO at the interface and a heterojunction will be formed to facilitate the e^{-} capture. As a result of this heterojunction the free e^{-} will be transfer among Ag and BFO or Pt and BFO or Pd and BFO because of the difference in their work functions (ϕ_m). Pd had the highest ϕ_m of 5.62 eV (Kong et al., 2013; Tan et al., 2015), followed by Pt which is 5.60 eV (Guy & Ozacar, 2016), while the Ag has the lowermost value of 5.49 eV (He et al., 2014; Tan et al., 2015). This enables the transfer of e^- form the CB of BFO to the NM. Hence, it extended the photogenerated $e^-{-}h^+$ pairs lifetime, which increased the production of reactive oxidizing species. Especially, the Pd was more active than the Ag and Pt in improving the separation efficiency of $e^-{-}h^+$ pairs due to its higher work function. The potentials of metallic NM with respect to the standard hydrogen electrode (E_m) can be estimated using the following equations.

$$E_m = \phi_m - E^e \tag{4.10}$$

where ϕ_m is the work function with respect to vacuum level (eV) and E^e is the energy of free electron relative to the hydrogen scale (around 4.5 eV) (Chang et al., 2018; Kumar et al., 2013). The band potential of BFO can be estimated using the Mulliken electronegativity theory (Fan et al., 2016; Saravanakumar et al., 2017).

$$E_{VB} = X_{BFO} - E^e + 0.5E_g \tag{4.11}$$

$$E_{CB} = E_{VB} - E_g \tag{4.12}$$

where E_{VB} was the VB edge potential (eV), E_{CB} was the CB edge potential (eV), E^e was the free electron energy on hydrogen scale (around 4.5 eV), E_g was the band gap energy of BFO and X_{BFO} was the absolute electronegativity of the BFO, which was around 6.04 eV (Fan et al., 2016; Xu et al., 2016). According to the above equations, with the potential scale relative to the standard hydrogen scale (NHE), the ϕ_m of the NM can be compared with the band structure of the pure BFO as follows: E_{CB} (0.29 eV) < E_{Ag} (0.99 eV) < E_{Pt} (1.1 eV) < E_{Pd} (1.12 eV) < E_{VB} (2.79 eV). In the case of Pd, the higher value of E_{Pd} than the E_{CB} accelerate the transfer of e^- from BFO to the Pd. As a result more photogenerated h^+ might be accumulated at the interface and this situation enhanced the oxidizing ability of OH^- ions and H_2O molecules to generate the •OH radicals. Thus, Pd-BFO nanocomposite displays a higher photocatalytic activity compared with Pt-BFO and Ag-BFO nanocomposites. Similarly, when the higher energy potential of metallic Pt was compared with the Ag makes Pt-BFO nanocomposites more effective for e^- capture under the same conditions. The Pt-BFO nanocomposites was more efficient than the Ag-BFO nanocomposite to serve as an e^- acceptor, which led to the improved photocatalytic activity.

Moreover, it is also extremely important to understand the fate of the photogenerated e^- during the photodegradation reaction. The photogenerated e^- in the BFO were trapped by absorbed O_2 molecules to produce the H_2O_2 owing to the greater *CB* edge potential than those of the standard redox potential *Eo* (O_2/H_2O_2) (0.682 eV vs NHE) (Chang et al., 2018; Sin et al., 2014). The H_2O_2 is a very reactive agent, which has the ability to breakdown the organic molecules into smaller compounds. In the meantime, the photogenerated h^+ in the *VB* of BFO react with the –OH ion on the surface of BFO nanocomposite to produce •OH radicals E_o (•OH/H_2O) (+2.68 eV vs NHE) (Xu et al. 2016; Di et al. 2017). In summary, the photogenerated •OH radicals and H_2O_2 molecules were the key oxidizing agent to degrade the MG dye.

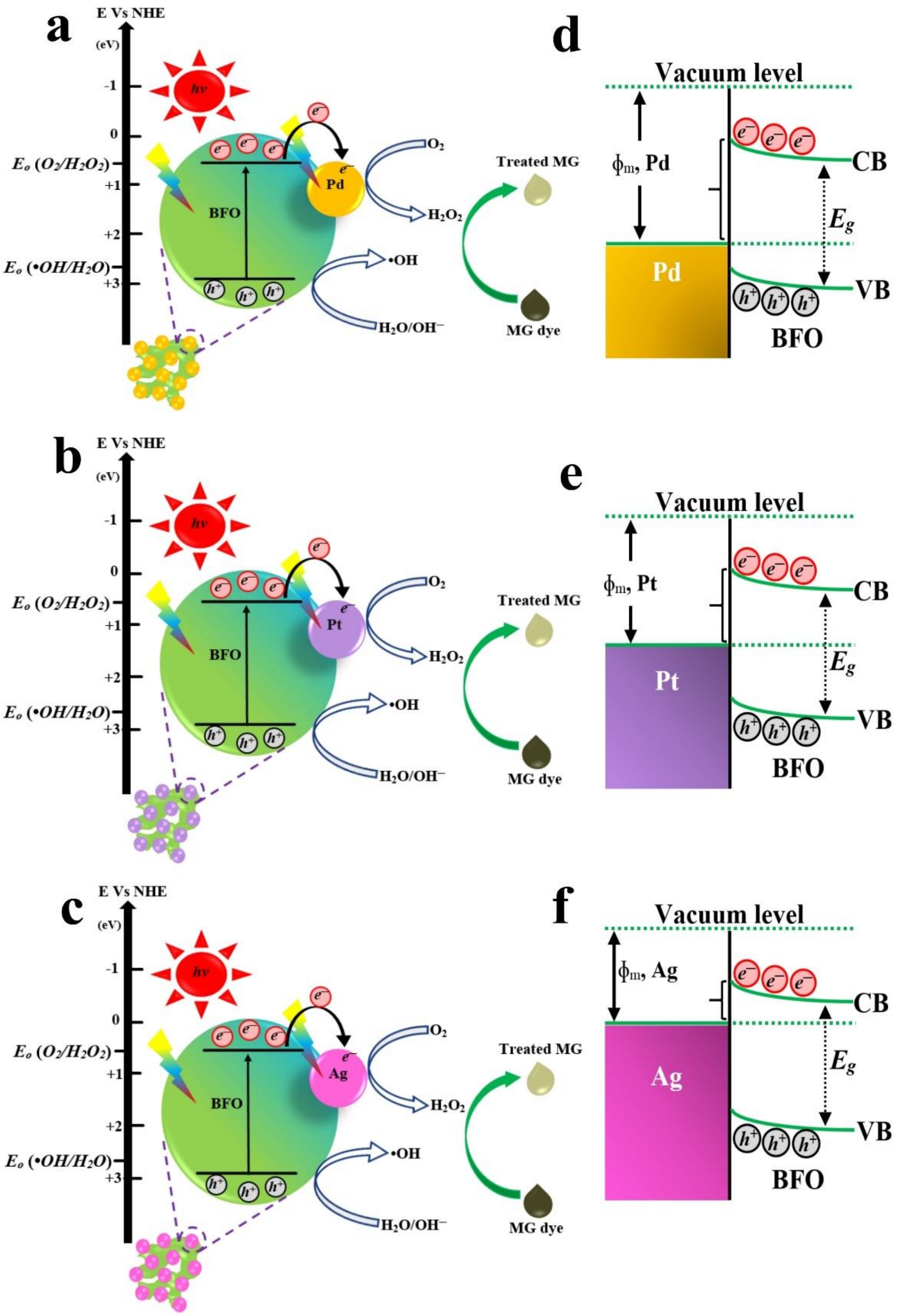

Figure 4.25: Schematic illustration of proposed photodegradation mechanism and band bending at the interface between NM and BFO under visible light irradiation **a** and **d** Pd-BFO, **b** and **e** Pt-BFO and **c** and **f** Ag-BFO nanocomposite.

4.4. Effect of the operating parameters

4.4.1 Effect of light intensity

The light intensity is the most vital operating parameter in the photocatalysis process. As it directly affects the rate of photocatalytic reaction and energy utilization ratio (Liping et al., 2007). Therefore, the influence of different light intensities on the photodegradation of MG dye was studied in the range between 25−105 W over 2 wt% Pd-BFO nanocomposites. The photocatalytic experiments were performed using constant photocatalyst dosage of 1 g/L, initial MG dye concentration of 10 mg/L and at natural solution pH.

Figure 4.26 displays the photocatalytic activities of Pd-BFO nanocomposites towards the MG dye degradation under different light intensities. The results exhibited that the enhanced light power has a positive impact on the photodegradation of MG dye. The results exhibited that around 96.4% MG degradation was recorded under the irradiation of 105W lamp, while only 50.3% and 65.1% MG was degraded under the 25W and 55W lamps, respectively.

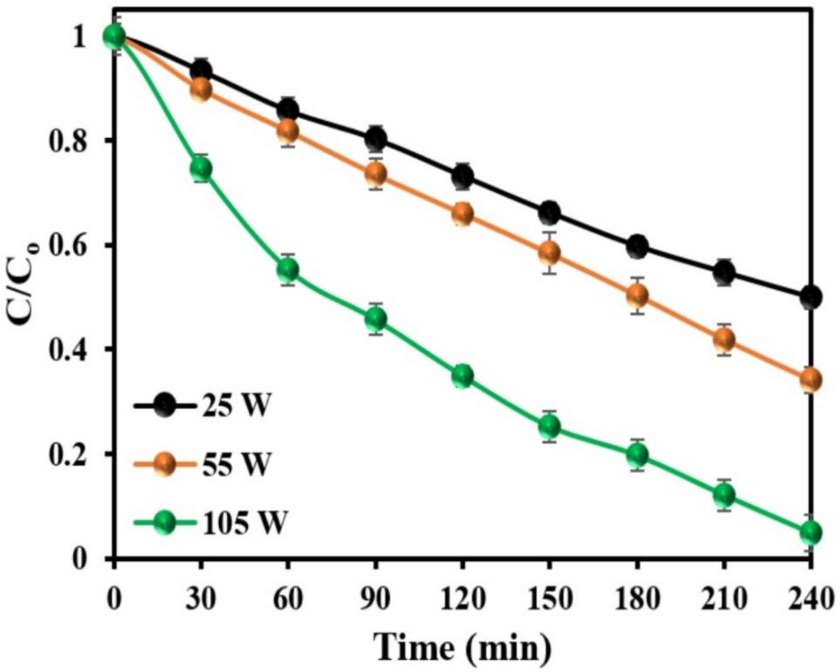

Figure 4.26: Effect of light intensity on the photodegradation of MG dye over Pd-BFO nanocomposite under visible light irradiation ([MG] = 10.0 mg/L; photocatalyst dosage = 1.0 g/L; pH = 5.45).

The photodegradation reaction was generally initiated by the light irradiation equal to the E_g value of the semiconductor and followed by the redox reaction to produce the active species (Chong et al., 2015; Rauf & Ashraf, 2009). With the improvement in power of light, the Pd-BFO nanocomposites can absorb additional photons and induced excess e^-–h^+ pairs to partake in the redox reaction. As a result, the MG photodegradation improved with the enhancement of light power.

Previously, Behnajady et al., (2006) also witnessed the similar linear relationship among the intensity of light and extent of phenol and methyl orange (MO) dye degradation. Chen et al., (2017) synthesized Ag_3PO_4/Ag/$BiVO_4$ nanocomposites and checked its photocatalytic performance towards the tetracycline degradation using different light intensities of visible light. Their findings stated that the highest photodegradation of tetracycline was obtained using 300 W than those of the 150 W, 100W and 50 W. Similar kind of photocatalytic trend was commonly presented in the literature (Lam et al., 2018; Mirmasoomi et al., 2017; Sobana et al., 2015; Xue et al., 2016).

4.4.2 Effect of photocatalyst dosage

In industrial application, the control of photocatalyst dosage is extremely important as it can directly affect the photodegradation of organic contaminants (Wen et al., 2018). Therefore, the effect of 2 wt% Pd-BFO nanocomposite dosage on the MG dye degradation was investigated in the range from 0.5 g/L to 2.5 g/L under visible light irradiation. The photocatalytic experiments were executed using light intensity of 105 W, initial MG dye concentration of 10 mg/L and at natural solution pH.

Figure 4.27 depicts the MG dye degradation activity using various catalyst loadings of 2 wt% Pd-BFO nanocomposite. The photodegradation of MG dye improved from 62.45% to 100% as increasing the Pd-BFO nanocomposite dosage from 0.5 g/L to 1.5 g/L. However, with the further increasing in the photocatalyst dosage the MG dye degradation efficiency decreased to 83.2%.

The possible reason for improved photodegradation could be the enhancement in the quantity of active sites, which led to higher photocatalytic activities (Lam et al., 2018; Wen et al., 2018). Ng et al., (2016) stated that the rise in the photocatalyst dosage improved the degradation performance by enhancing the number of reactive oxygen species in the photocatalytic system. However, when the photocatalyst dosage was higher than 1.5 g/L, the photodegradation was again inhibited due to the enhanced turbidity and reduced the light penetration in the solution. This phenomenon can be described, as the number of photons in the system was constant when the light irradiation source was stable. Hence, there was a best amount of photocatalyst dosage, which can be utilized the maximum amount of photo-energy (Deng et al., 2018; Saravanakumar et al., 2016).

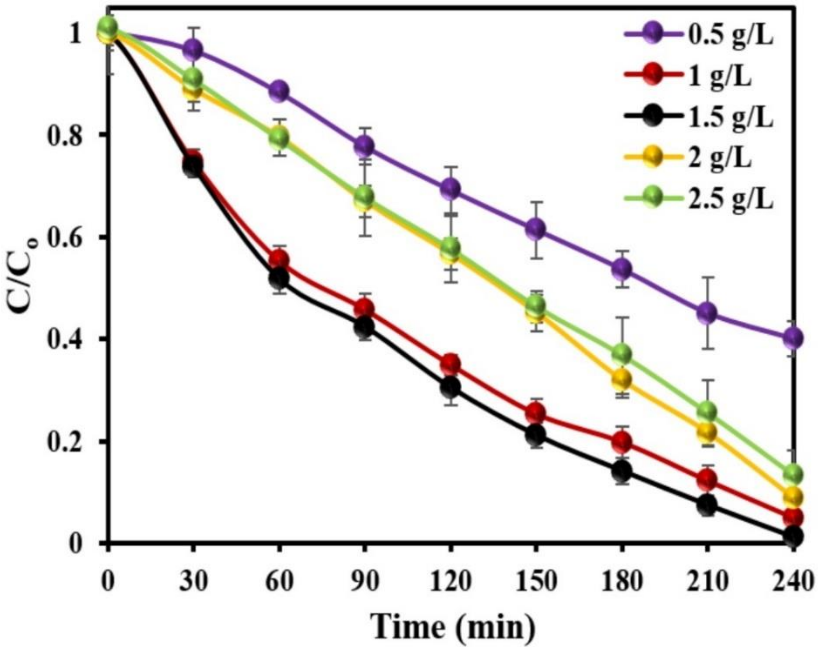

Figure 4.27: Effect of catalyst dosage on the photodegradation of MG dye using Pd-BFO nanocomposites under visible light irradiation (Light intensity = 105 W; [MG] = 10.0 mg/L; pH = 5.45).

Soltanabadi et al., (2018) stated that the phenol degradation performance was enhanced with enhancing the Pd-TiO_2 nanocomposites loading until it reached the optimum catalyst loading level. However, with further increasing the Pd-TiO_2 catalyst loading contents beyond the optimum amount caused a decrease in the photodegradation activity. Hence, in present research, the 1.5 g/L photocatalyst dosage was chosen to be the optimum amount.

4.4.3 Effect of initial MG dye concentration

The initial concentration of organic pollutants changed extensively in the natural environment. It was important to examine the effect of initial MG dye concentration on the photocatalytic activities of the Pd-BFO nanocomposites. The effect of initial MG dye concentrations was also investigated in the range from 5mg/L to 80 mg/L over 2 wt% Pd-BFO nanocomposites under visible light irradiation. The photocatalytic experiment was performed using a constant light intensity of 105 W, photocatalyst dosage of 1.5 g/L, initial MG dye concentration of 10 mg/L and at natural solution pH.

Figure 4.28 depicts the MG dye degradation using various initial concentrations. It can be clearly seen that the Pd-BFO nanocomposites exhibited the highest photocatalytic activity for 5 mg/L MG dye solution than those of the remaining initial concentrations (10−80 mg/L). With the initial concentration of 5 mg/L, the photodegradation performance reached 100% after 180 min of visible light irradiation. When the initial concentration increased to 20 mg/L, the 70.8% degradation activity was achieved after 240 min of light irradiation. On the other hand, only around 40.7% and 19.8% MG dye degradations were obtained when the initial MG concentration further increased to 40 and 80 mg/L, respectively.

The photocatalytic activity was not only related to the generation of reactive oxygen species but also depended on the capabilities of reactive species to attack the organic pollutant molecules. At the lower MG initial concentration, the quantity of active sites were excessively available to generate the •OH radicals, which led to the higher photocatalytic activity (Wen et al., 2018; Xiao et al., 2017). Nonetheless, when the initial concentration was enhanced, the excess MG dye molecules would be in competition with O_2 and OH^- to adsorbed onto the surface of Pd-BFO molecules, which decreased the generation of •OH radicals for the MG dye degradation (Chong et al., 2015). Another possible reason might be that the higher initial MG dye concentration can prevent light to pass through the MG solution because of the attenuation of light at higher concentration (Jiang et al., 2019; Wen et al., 2018). Excess amount of intermediates products were also formed at the higher MG dye concentration. These intermediates would contest with the MG dye for interaction with the active sites on the surface of Pd-BFO nanocomposites, which resulted a reduction of the MG dye degradation efficiencies (Wen et al., 2018). Similar findings were also reported in the literature (Wang et al., 2016; Seifvand et al., 2016).

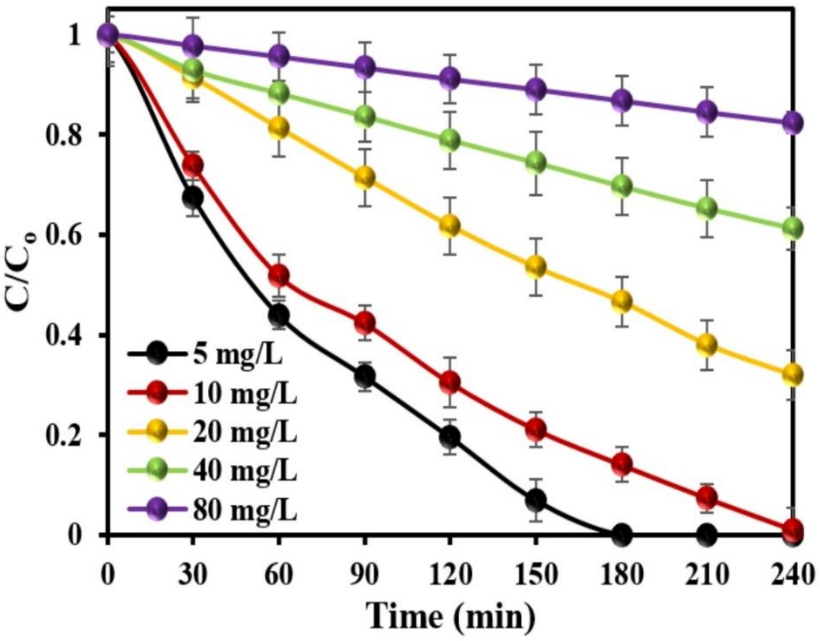

Figure 4.28: Effect of initial MG concentration on the photodegradation of MG dye using Pd-BFO nanocomposites under visible light irradiation (Light intensity = 105 W; catalyst loading = 1.5 g/L; pH = 5.45).

Sobana et al., (2015) studied the effect of the initial concentration of direct blue 53 in the range between 10−90 mg/L using a constant loading of Ag-TiO_2 as photocatalyst (1.0 g/L). The results stated that the degradation efficacy declined with the enhancement in the initial direct blue 53 dye concentration. They explained that this decrease can be attributed to an excess quantity of dye molecules adsorbed on the surface of Ag-TiO_2, which reduced the access of photon molecules to reach the photocatalyst surface. Hence, the photocatalytic activities declined as the initial concentration of direct blue 53 were increased. Jassal et al., (2015) performed the photocatalytic experiments using Ag-ZnO nanocomposites towards the photodegradation of MG dye with the initial concentration ranged between 5−30 mg/L. Their findings also suggested that the photocatalytic activities declined with the increase in the MG dye initial concentration, which was attributed to the less number of active species generation to take part in the photocatalytic activities.

4.4.4 Effect of solution pH

Solution pH commonly played an vital part in photodegradation process as it strongly affects the generation of the main reactive species, ionization state of the pollutants and electric properties of photocatalyst (Kamranifar et al., 2019; Wu et al., 2019). The solution pH effects were studied in the range between pH 3 to pH 9 towards the photodegradation of MG dye over 2 wt% Pd-BFO nanocomposite under visible light irradiation. The desired solution pH before the reaction was adjusted using 0.1 M HCl and NaOH solution. The photocatalytic experiment was performed using a constant light intensity of 105 W, photocatalyst dosage of 1.5 g/L and initial MG dye concentration of 5 mg/L.

Figure 4.29 displays the photodegradation efficiencies of MG dye at different solution pHs. The natural pH value of MG dye is pH 5.45. It can be witnessed that the MG photodegradation performance improved with the rise in pH value from 3 to 7. At pH 7.0, 100% MG dye photodegradation was recorded after 150 min of visible light irradiation. Nonetheless, with the additional increase in solution pH (pH 9) led to a decrease in the photodegradation activity. At pH 9.0, the MG dye degradation performance reached 100% after 240 min of visible light irradiation.

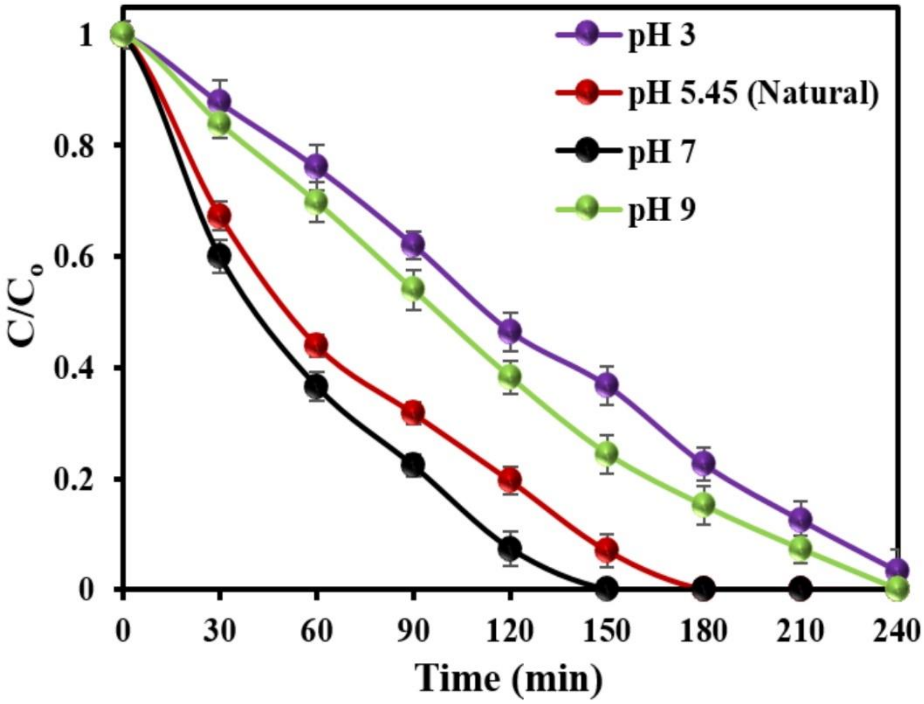

Figure 4.29: Effect of solution pH on the photodegradation of MG dye over Pd-BFO nanocomposites under visible light irradiation. (Light intensity = 105 W; [MG] = 5.0 mg/L; photocatalyst dosage = 1.5 g/L).

The effect of pH on dye degradation was mainly credited to the charge variations among the catalyst surface and MG dye molecules (Habibi-yangjeh et al., 2019). The pH_{pzc} for BFO is around pH 7.0, and the MG is a cationic dye (Mohamed et al., 2016; Soltani & Entezari, 2013). The initial pH can effect the electrical properties of MG dye and BFO, which affected the adsorption of MG dye on the surface of the photocatalyst. At pH < 7.0, the BFO surface and MG dye molecules would be positively charged, suggesting the electrostatic repulsion among the BFO and MG molecules, which reduced the photocatalytic activities (Habibi-yangjeh et al., 2019; Mohamed et al., 2016). Additionally, when the solution pH was changed with HCl, the Cl^- anion also tend to adsorbed on the surface of photocatalyst (Ai et al., 2015; Chen et al., 2017). These Cl^- anions were highly unstable and have capability to scavenge the h^+ and •OH radicals. Similar outcomes were also presented by other researchers (Ajmal et al., 2014; Eskandarloo et al., 2014).

On the other hand, at higher solution pH value (pH 9), OH^- ions were generated in the reaction mixture which would be repelled by the negatively charged photocatalyst surface and thus, reduced the photodegradation activity. Furthermore, the NaOH was applied to adjust the higher values of pH. It was reported in the literature that the increase in the Na^+ ions concentration from a certain level might also compete with the substrate molecules on the surface of the photocatalyst (Ai et al., 2015; Dariani et al., 2016). Therefore, the highest MG degradation was observed at pH 7.0.

Dariani et al., (2016) studied the solution pH effects towards the methylene blue (MB) degradation using TiO_2 nanoparticles. The photocatalytic efficiency was decreased dramatically at pH 11.0 after 300 min of visible light irradiation. This decrease in the photocatalytic efficiency was due to the negatively charged photocatalyst surface, which repelled the dye molecules from the photocatalytic reaction. Mosleh et al., (2016) studied the photodegradation of MG and safranin O (SO) dyes under strong acidic conditions over HKUST-1 metal organic framework (MOF) and mesoporous silica (SBA-15) loaded HKUST-1-SBA-15 nanocomposites. To be more accurate, the degradation efficiencies of MG and SO dyes were lowest at pH 3, and start increasing when the pH was enhanced from pH 3 to pH 4 under the same photocatalytic reaction conditions (dye initial concentration of 10 mg/L and photocatalyst dosage of 1 g/L). The decrease in the acidic medium was described by the presence of Cl^- ions and repulsion between the positively charged dye molecules and photocatalyst surface.

4.4.5 Effect of different anions

It is a well-known that the real wastewater contains different inorganic anions. These inorganic anions might affect the photocatalytic degradation efficiency of the substrate. Therefore, considering this factor, the effect of Cl^-, $H_2PO_4^-$, HCO_3^-, and CO_3^{2-} anions on the degradation of MG dye using 2 wt% Pd-BFO nanocomposites were investigated. A common cation Na^+ was applied in all of the experiments; thus, only the anions exerts their effect on the photocatalytic reactions. The experiments were performed using light intensity of 105 W, photocatalyst dosage of 1.5 g/L, initial MG dye concentration of 5 mg/L and solution pH of 7.0.

Figure 4.30 depicts the results of MG dye degradation in the existence of several anions with a concentration of 10 mM. In the presence of CO_3^{2-} and HCO_3^-, the MG dye degradation efficiency was reduced to some degrees, which might be due to their ability to scavenge the •OH radicals (Cui et al., 2014; Kango et al., 2013). These CO_3^{2-} and HCO_3^- consume most of the •OH radicals produced at the surface of the photocatalyst, resulting a decline in the reactive species. Thus, the MG dye degradation efficiency was hindered.

$$CO_3^{2-} + \bullet OH \longrightarrow CO_3^{\bullet -} + OH^- \quad (4.3)$$

$$HCO_3^- + \bullet OH \longrightarrow CO_3^{\bullet -} + H_2O \quad (4.4)$$

$$CO_3^{\bullet -} + \bullet OH \longrightarrow HCO_3^- \quad (4.5)$$

$H_2PO_4^-$ ions also had potential to scavenge •OH radicals to produced $H_2PO_4\bullet$ reactive radical, resulting in the decreased photocatalytic activity of MG dye (Kumar et al., 2018; Li-xiang et al., 2018).

$$H_2PO_4^- + \bullet OH \longrightarrow H_2PO_4\bullet + OH^- \quad (4.6)$$

Moreover, the addition of Cl^- ions in the reaction mixture greatly decreased the photocatalytic activity. This might be because of the h^+ and •OH radicals traping ability of Cl^- ions as displayed in the following equations (Ajmal et al., 2014; Eskandarloo et al., 2014).

$$Cl^- + h^+ \longrightarrow Cl^\bullet \quad (4.7)$$

$$\bullet OH + Cl^- \longrightarrow -OH + Cl^\bullet \quad (4.8)$$

$$Cl^\bullet + Cl^\bullet \longrightarrow Cl_2 \quad (4.9)$$

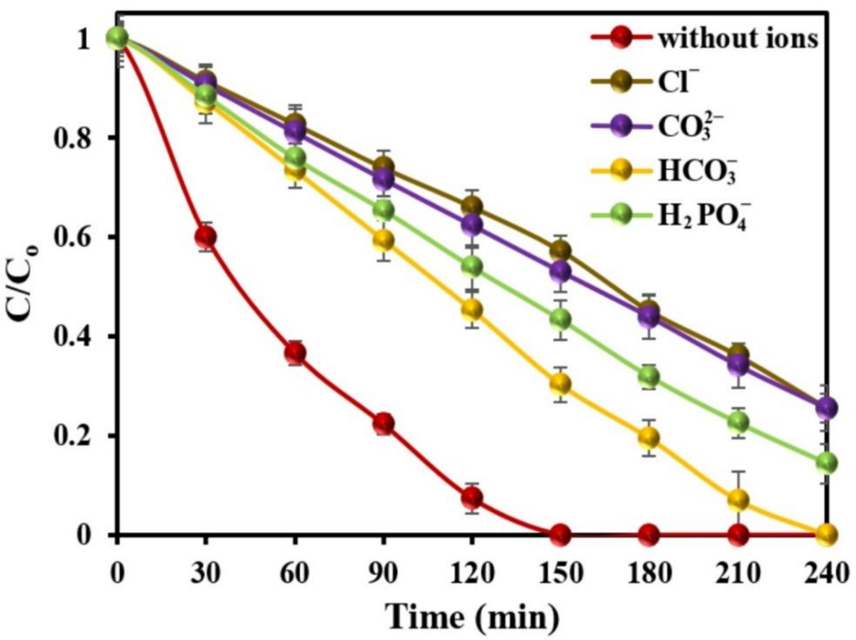

Figure 4.30: Effect of different anions on the photodegradation of MG dye using Pd-BFO nanocomposites under visible-light irradiation. (Light intensity = 105 W; [MG] = 5.0 mg/L; catalyst loading = 1.5 g/L; solution pH = 7.0).

Kumar et al., (2018) checked the inorganic anions effects on the photodegradation of ibuprofen over g-$C_3N_4/TiO_2/Fe_3O_4$@SiO_2 nanocomposite under visible light irradiation. The results stated that the inorganic anions were in competition with the ibuprofen molecules for the adsorption, which decreased the photodegradation performance of g-$C_3N_4/TiO_2/Fe_3O_4$@SiO_2 nanocomposites. Gao et al., (2016) applied $BiPO_4/BiOBr$ as photocatalyst to verify the effects of different inorganic anions towards the degradation of RhB dye. The results stated that all the applied anions such as Cl^-, HCO_3^- and NO_3^- had the negative effects on the photocatalytic activities. They also explained that the decrease in the photocatalytic activities was due to the radical scavenging abilities of the inorganic anions.

4.4.6 Effect of humic acid

Humic acids are complex organic substances produced by the disintegration of plants and animals remains in the soil and are presents in rivers, lakes etc. as water-soluble compounds. These humic substances have the ability to scavenge reactive oxygen species, which led to a decline in the photocatalytic performance (Lou et al., 2015; Palacio et al., 2017; Zhang et al., 2008). Therefore, the effect of humic acid was studied on the MG dye degradation ganged between 0 mg/L to 10 mg/L over 2 wt% Pd-BFO nanocomposites. The photocatalytic reactions were performed using light intensity of 105 W; photocatalyst dosage of 1.5 g/L; initial MG dye concentration of 5 mg/L and solution pH of 7.0.

Figure 4.31 displays the photocatalytic activities results of 2 wt% Pd-BFO nanocomposites towards the degradation of MG dye in the presence of humic acid. The results presented that the humic acid has a negative impact on the MG dye degradation. With the humic acid concentration of 2 mg/L, the degradation efficiency reached 100% after 180 min of light irradiation. When the humic acid concentration was increased from 2 mg/L to 7 mg/L, the 100% MG was photodegraded within 240 min of light irradiation. On the other hand, when 10 mg/L humic acid was inserted in the reaction mixture, around 95% MG dye degradation was achieved.

The decline in the photocatalytic activities can be credited to the radical trapping ability of the humic acid and its competition with MG dye for active sites. It is a renowned fact that the photodegradation performance are highly depended on the production and proper utilization of reactive oxygen species. The humic acid had a high tendency to scavenge the h^+ and •OH radicals, which led to a declined photodegradation (Li & Hu, 2016; Rioja et al., 2016). Additionally, when the initial concentration of humic acid was increased, the excess MG dye molecules would be in competition with the humic acid to be adsorbed onto the surface of Pd-BFO molecules, which declined the generation of •OH radicals for the MG dye photodegradation (Deng et al., 2016; Repousi et al., 2017).

Rioja et al., (2016) performed the photocatalytic experiments using TiO_2 towards the degradation of lofibric acid in the company of humic acid with the concentration in the range between 1−5 mg/L. Their results clearly stated that the photocatalytic activities were decreased in the existence of humic acid, which was accredited to the competition for both active sites and reactive species. Palacio et al., (2017) hydrothermally synthesized Ce/TiO_2 and checked their photocatalytic activities in the presence of different concentrations of humic acids towards the degradation of phenol. They stated that the rate constant of phenol degradation was decreased even at the lower concentration of humic acid (1.0 mg/L). This decline in the photocatalytic activity was due to the radical scavenging ability of humic acids. Similar results were also observed during different organic pollutants degradation under visible light irradiation (Lin & Lin, 2007; Lou et al., 2015; Repousi et al., 2017).

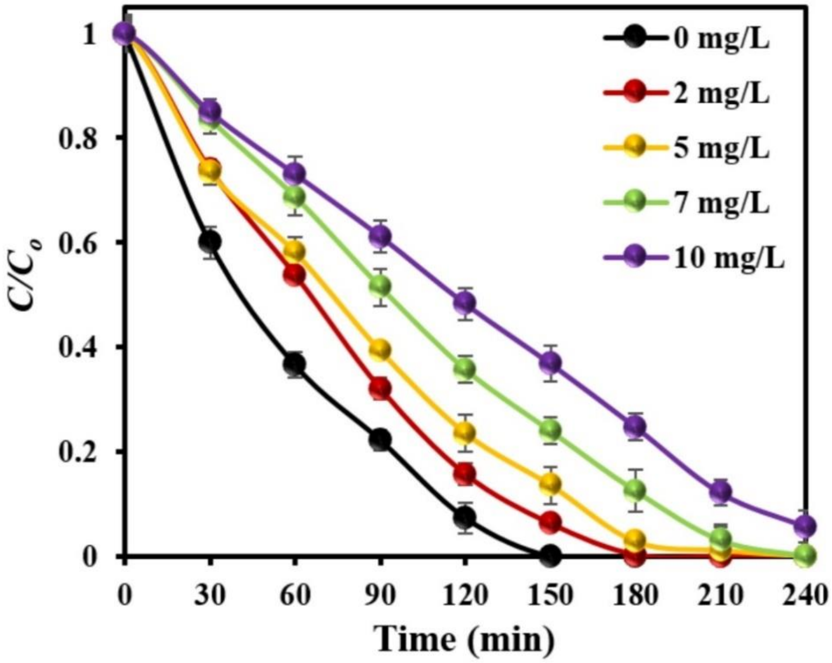

Figure 4.31: Effect of humic acid on the photodegradation of MG dye using Pd-BFO nanocomposites under visible-light irradiation (Light intensity = 105 W; [MG] = 5.0 mg/L; photocatalyst dosage = 1.5 g/L; pH = 7.0).

4.4.7 Mineralization study on MG dye

The complete mineralization of organic pollutants is an extremely important factor in the wastewater treatment process. In order to study the mineralization extent of MG dye, COD experiment at optimum conditions was performed. The mineralization experiment was performed using photocatalyst dosage of 1.5 g/L, initial MG dye concentration of 5 mg/L, solution pH of 7.0 under 105 W visible light irradiation. Figure 4.32 depicts the kinetic profiles on the MG dye photodegradation and COD removal. The results showed that the COD concentration gradually declined during the photodegradation of MG dye. 100% COD removal was recorded after 180 min of visible light irradiation. The COD removal took an extended time than the degradation efficiency, which suggested that there were still some intermediate compounds existing in the photodegradation system. Hence, longer light irradiation time would be required for the complete mineralization. Similar trend between the mineralization studies and dyes photodegradation was also presented by numerous reports (Ao et al., 2018; Bansal et al., 2016; Garg et al., 2015; Zuniga-benitez & Penuela, 2016).

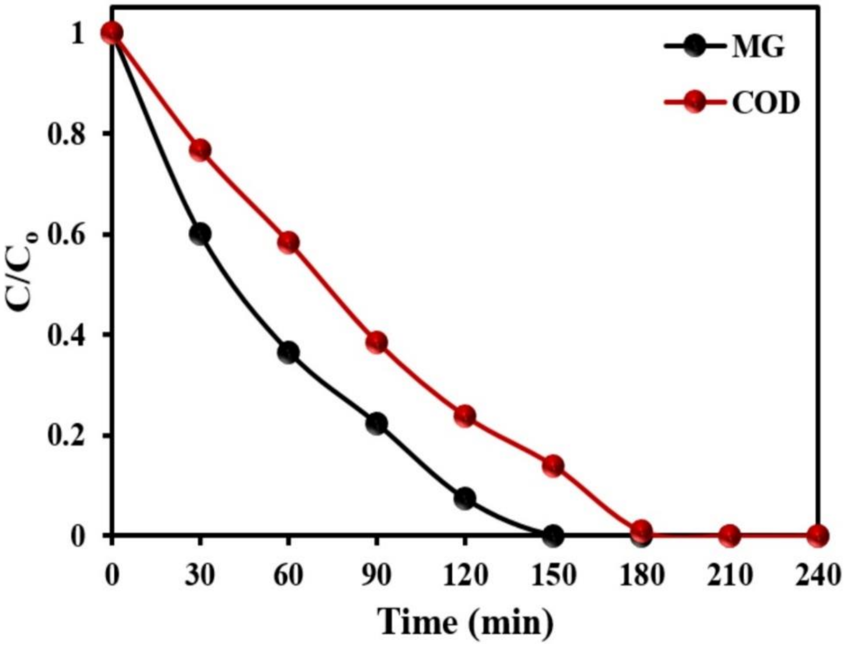

Figure 4.32: Parallel observation of MG and COD concentration profile against the reaction time over Pd-BFO nanocomposites (Light intensity = 105 W; [MG] = 5.0 mg/L; photocatalyst dosage = 1.5 g/L; pH = 7.0).

4.4.8 Comparison with different photocatalysts

The photocatalytic performance of 2 wt% Pd-BFO nanocomposite was compare with the commercial TiO_2 sample. The comparison was performed using photocatalyst dosage of 1.5 g/L, initial MG dye concentration of 5 mg/L, solution pH of 7.0 under 105 W visible light irradiation. Figure 4.33 displays that the Pd-BFO nanocomposite achieved a complete MG dye degradation after 150 min of visible light irradiation, which was much greater than the commercial TiO_2. The commercial TiO_2 shows 100% degradation efficiency after 240 min of light irradiation.

The enhancement in the photocatalytic performance of the Pd-loaded BFO nanocomposite can be credited to its effective migration of photogenerated $e^{-}-h^{+}$ pairs as well as structural properties. As stated in the photocatalytic mechanism section, the NM-BFO nanocomposites have the heterojunction, which can efficiently separate the $e^{-}-h^{+}$ pairs and enhance the e^{-} and h^{+} lifetime. In the case of commercial TiO_2, the photogenerated $e^{-}-h^{+}$ pairs have a high recombination efficiency as stated in the literatures (Edelmannova et al., 2018; Chen et al., 2018). As a result, the migration of the $e^{-}-h^{+}$ pairs to the photocatalyst surface was lower, which resulted in the lesser •OH radicals generation during photodegradation reaction.

In the present study, Pd-loaded BFO nanocomposite showed higher photocatalytic performance compared with the commercial TiO_2. A comparison study was performed among the photocatalytic performance of the synthesized nanocomposite with those available in the literature. Table 4.2 depicts the comparison in the photocatalytic activities between the 2 wt% Pd-BFO nanocomposites and other available photocatalysts utilized towards the photodegradation of MG dye. It was witnessed that the degradation performance in the present study was higher than those the other reposts available in the literature. The higher photodegradation performance of Pd-BFO nanocomposite can be attributed to the heterojunction between the metallic Pd and BFO nanoparticles, which held in the production of higher number of reactive oxygen species.

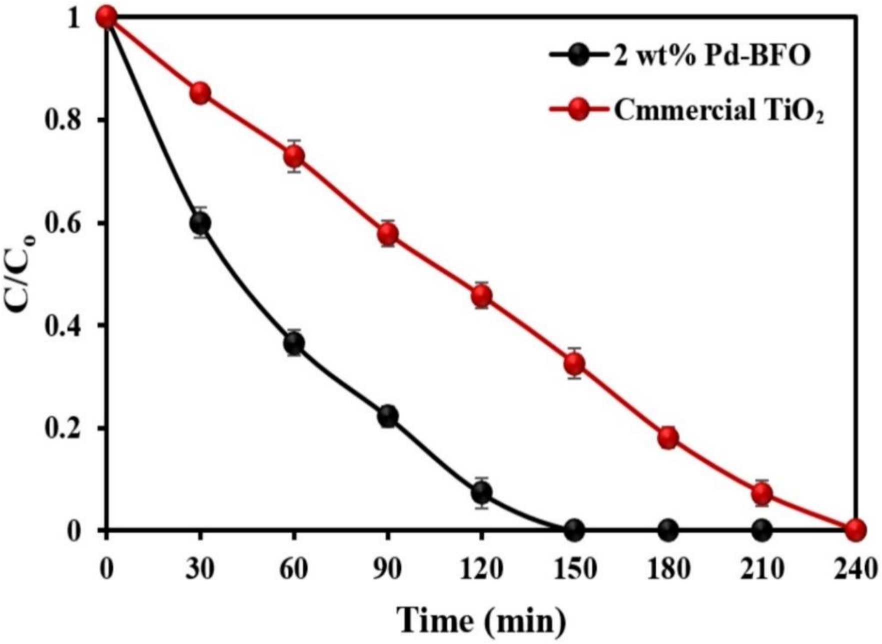

Figure 4.33: Photodegradation performance of 2 wt% Pd-BFO nanocomposite and commercial TiO_2 (Light intensity = 105 W; [MG] = 5.0 mg/L; photocatalyst dosage = 1.5 g/L; pH = 7.0).

4.4.8 Reusability test on the Pd-BFO photocatalysts

High photoactivity and recyclability of any photocatalyst played an integral role in practical applications. To investigate the recyclability of 2 wt% Pd-BFO nanocomposite, the nanocomposite was recycled for several times. The experiment was performed using photocatalyst dosage of 1.5 g/L, initial MG dye concentration of 5 mg/L and solution pH of 7.0. The Pd-BFO nanocomposite was recovered from the dye solution with the help of a simple magnetic bar after 150 min visible light irradiation. The nanocomposite was then washed with distilled water, dried at 120 °C for 3 h and again inserted to fresh MG solution for the continuous runs. Figure 4.34 depicts that the Pd-BFO nanocomposite still maintains higher photodegradation even after the sixth cycle. The photodegradation performance of the Pd-BFO nanocomposite was slightly reduced from 100% to 92.8% after six cycling runs. It was important to mention that the decrease in the photodegradation can be due to the loss of small quantity of the recycled nanocomposite. The leaching of different ions such as Fe^{3+} and Pd^0 were also estimated for each cycle using an ICP-MS technique. The results indicated no leaching for Fe^{3+} ions, which was also consistent with the literature report available on BFO (Soltani & Entezari, 2014; Yin et al., 2016). However, the small number of metallic Pd^o were detected in the range from 0.0327 ppm to 0.0237 ppm during the six recycling experiments, which was still lower than the reported literatures (Soni & Kotadia, 2014; Wang et al., 2017). This slight loss in the metallic Pd^0 could also be one of the causes for decreased photodegradation activity as less number of Pd^0 nanoparticles on the

BFO surface than the optimum amount would lead to the reduced $e^{-}-h^{+}$ pairs separation efficiency.

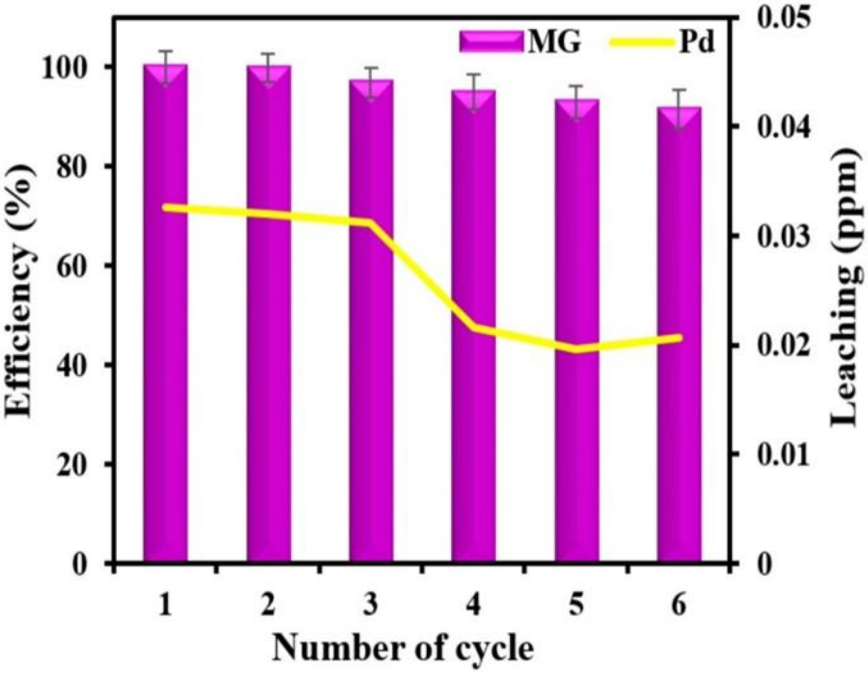

Figure 4.34: Degradation efficiencies and leakage of Pd^0 ions using 2 wt% Pd-BFO nanocomposite over six consecutive recycling runs.

Table 4.2: Tabulated comparison for the photodegradation of MG dye using UV-visible light photocatalysts.

Photocatalyst	**Morphology**	**Catalyst loading (g/L)**	**Concentration of MG dye (mg/L)**	**Volume of MG dye (mL)**	**Light power (W)**	**Time (min)**	**Degradation (%)**	**Reference**
PANI/ZnO	Nanorods	4	5	100	Direct sunlight	300	94.8	(Eskizeybek et al., 2012)
V-ZnO	Irregular	0.5	10	100	300	240	72.4%	(Khezami et al., 2016)
BiOI/Ag_3VO_4	Microsphere	0.5	10	50	500	210	92.0	(Wang et al., 2015)
CdS	Irregular	2	5	100	85	150	89.2	(Kaur et al., 2018)
rG/Al_2O_3	Bean-shaped	1	5	100	Direct sunlight	210	84.7	(Pathania et al., 2016)
Pd-BFO	Coral-like	1	5	100	105	150	100	Current study

4.5 Photocatalytic degradation of phenol by Pd-BFO photocatalyst under visible light

4.5.1 Effect of initial phenol concentration

Considering that the degradation of organic dyes often involves the photosensitization effect, the photocatalytic activity of 2 wt% Pd-BFO nanocomposite was also investigated by the degradation of another colorless organic compound. Thus, phenol was chosen as another model pollutant, as it is considered to be an environmental risk due to its strong corrosive nature as well as it is highly stable to the light irradiation and biodegradation (Gou et al., 2018; Liu & Cai, 2018). Figure 3.35 depicts the photodegradation of phenol using the different phenol initial concentrations ranged between 5−80 mg/L. The photocatalytic tests were performed using the catalyst loading of 1 g/L and at natural solution pH. It can be seen that with the increase in initial phenol concentration the photodegradation performance declined. After 210 min of light irradiation, phenol was completely degraded with a 5 mg/L initial. Increasing the phenol concentration to 80 mg/L, only around 14.8% degradation efficiency was recorded.

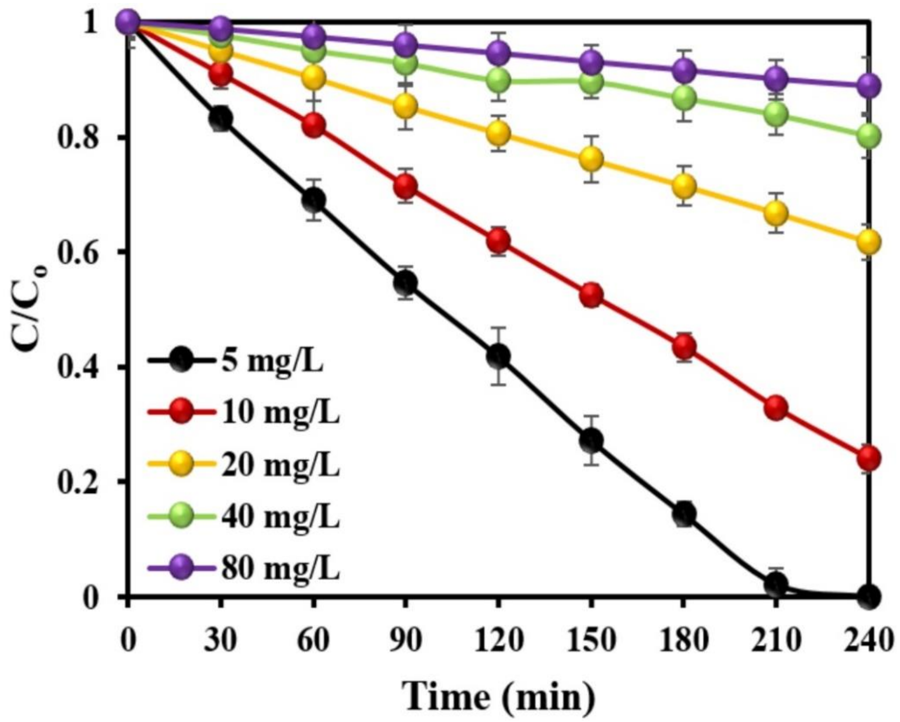

Figure 4.35: Effect of initial phenol concentration on the photodegradation of phenol using Pd-BFO nanocomposites under visible light irradiation (Light intensity = 105 W; photocatalyst dosage = 1.0 g/L; pH = 5.4).

The reason for the declined photodegradation performance of phenol can be described in the MG dye initial concentration (Section 4.4.3). The highest photodegradation activity was obtained at the lowest 5 mg/L initial concentration, which can be attributed to the excess accessibility of the active sites for adsorption by the phenol. With increasing the phenol concentration, a declined in the degradation was recorded possibly because of the excess concentration of phenol in the solution. Similar findings for phenol degradation was also observed in the literature reports (Sampaio et al., 2014; Saravanakumar & Muthuraj, 2017; Shet & Shetty, 2016; Ye et al., 2015).

4.5.2 Effect of solution pH

In the present study, the effect of various solution pH of phenol were studied using 2 wt% Pd-BFO nanocomposite in the ranged between pH 3 and pH 9. The solution pH before the experiment were fixed with the help of 0.1 M HCl and 0.1 M NaOH solutions. The photodegradation was performed using the photocatalyst dosage of 1.0 g/L and initial phenol concentration of 5 mg/L. Figure 4.36 presents the solution pH effects on the photodegradation of phenol. It can be seen that the photodegradation performance enhanced with the rise in pH values from 3 to 7, whereas additional increasing the solution pH led to the decrease in the photoactivity (pH 9). At pH 7, 100% phenol photodegradation was attained after 180 min irradiation of light.

The obtained results can be explained based on pH_{pzc} value of BFO and pKa of phenol, which was around 7.0 and 9.9, respectively (Bai et al., 2019; Soltani & Entezari, 2014). At the lower pH values, the phenol molecules were mainly in the non-dissociated form and the Pd-BFO surface was positively charged, suggesting lower phenol adsorption on the Pd-BFO nanocomposite surface, which led to a declined in the photocatalytic activity (Habibi-yangjeh et al., 2019; Kamranifar et al., 2019). Moreover, when the pH was fixed using HCl, the Cl^- ions may also tends to adsorbed on the Pd-BFO surface (Jallouli et al., 2018). The Cl^- ions have a high tendency to scavenge the h^+ and •OH radicals and converted into the Cl_2 molecules.

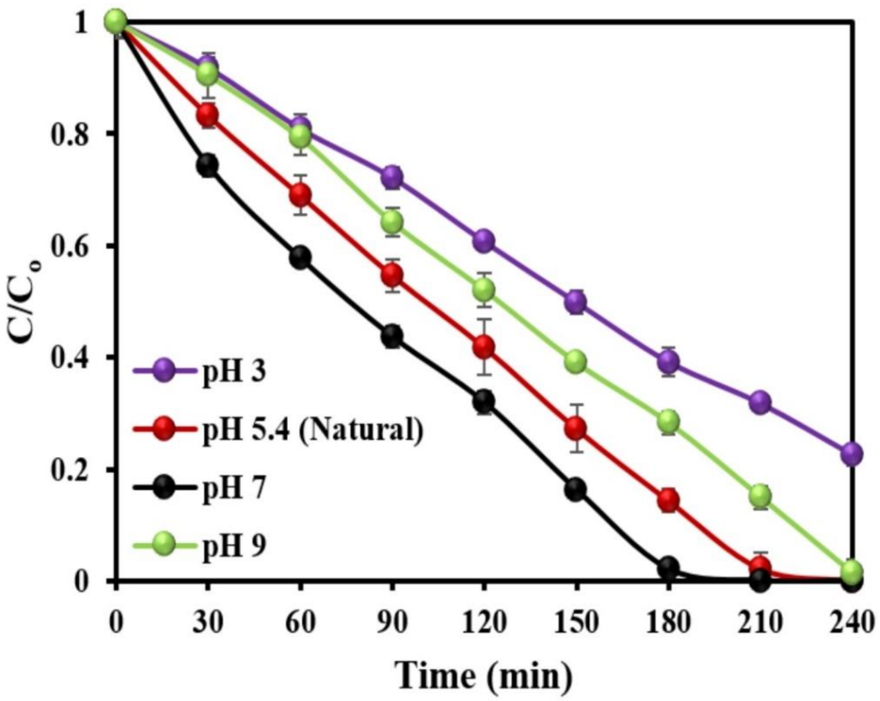

Figure 4.36: Effect of solution pH on the photodegradation of phenol using Pd-BFO nanocomposites under visible light irradiation. (Light intensity = 105 W; [Phenol] = 5.0 mg/L; photocatalyst dosage = 1.0 g/L).

On the other hand at higher pH, the surface of the Pd-BFO nanocomposite had negative charge, which developed electrostatic repulsion among the phenol molecules and Pd-BFO nanocomposite (Bai et al., 2019; Kumar et al., 2018). Furthermore, the existence of Na^+ ions in the reaction mixture also started a competition for adsorption on the active sites with the phenol molecules reduced the photodegradation at higher solution pH values (Singh et al., 2019; Lei et al., 2019). Yusoff et al., (2015) investigated the solution pH ranged between pH 1 to pH 12 on the photodegradation of phenol using Ag-ZnO nanocomposite. The solution pH was adjusted using the dilute solution of HCl and NaOH. Their findings suggested that the photocatalytic activities were lowest under the acidic conditions. The lower activity under the acidic conditions was described by the presence of Cl^- ions and lower adsorption of phenol on the surface of photocatalyst.

4.5.3 Comparison of different photocatalysts

The photocatalytic activity of 2 wt% Pd-BFO nanocomposite was also compared with the commercial TiO_2 towards the photodegradation of phenol under visible light irradiation and the results were presented in the Figure 4.37. The experiment were performed using the initial phenol concentration of 5 mg/L, photocatalyst dosage of 1 g/L and solution pH of 7.0. The 2 wt% Pd-BFO presented 100% phenol photodegradation after 180 min of light irradiation, which was much greater than the commercial TiO_2 (50.6%). The higher photocatalytic activity can be credited to the formation of heterojunction between the Pd and BFO, which not only boosted the separation efficiency of $e^- - h^+$ pair, but also possessed great redox ability for significant photocatalytic reaction.

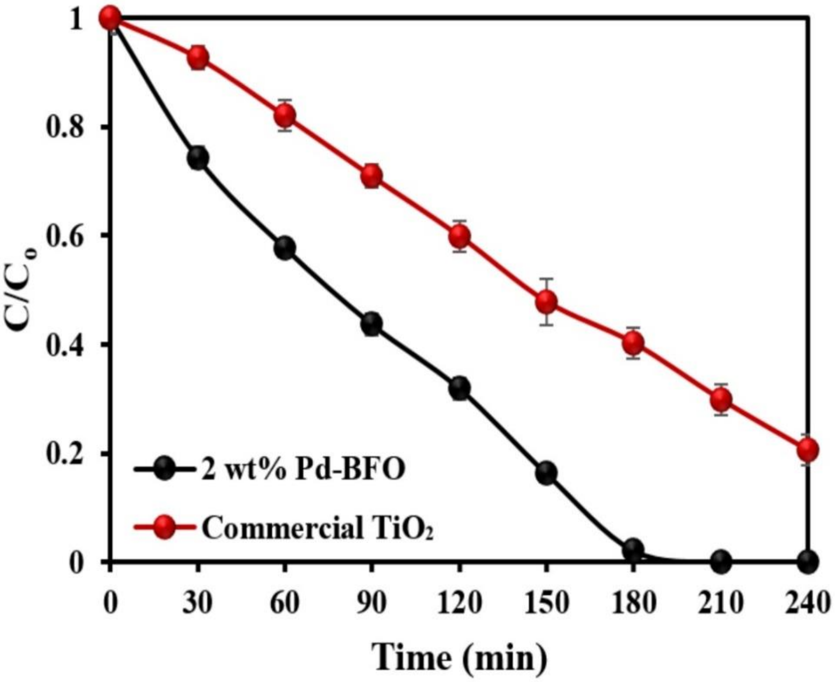

Figure 4.37: Photocatalytic activities of 2 wt% Pd-BFO nanocomposite and commercial TiO_2 (Light intensity = 105 W; [Phenol] = 5.0 mg/L; photocatalyst dosage = 1.0 g/L; pH = 7.0).

4.6 Identification of phenol intermediates and its mineralization study

4.6.1 HPLC analysis for phenol degradation

To further investigate the phenol degradation pathway over 2 wt% Pd-BFO nanocomposite under visible-light irradiation, the intermediate products were also identified using HPLC analysis. The experiment was performed using photocatalyst dosage of 1.0 g/L, initial phenol concentration of 5 mg/L and solution pH of 7.0. Figure 4.38 presents the HPLC profiles during phenol degradation as a function of time. In the start of the reaction, phenol displayed a distinctive bend at retention time (RT) of 5.6 min; which became smaller as the time of light irradiation prolonged and ultimately vanished after 240 min, presenting the outstanding photoactivity of Pd-BFO nanocomposite. In addition to the aforementioned compound, muconic acid at RT 1.4 min, pyrogallol at RT 1.7 min, resorcinol at RT 2.6 min, and benzoquinone at RT 3.3 min were the main generated intermediate products, when correlated with the standard chemicals. The recorded RT for the phenol and intermediate products were well consistent to the reported literatures (Gorska et al., 2009; Z. Guo et al., 2006; Sin et al., 2014; Sobczynski et al., 2004). All the peak intensities in the HPLC profile were decreased with the prolonged time irradiation, which suggested the complete photodegradation of phenol and the intermediate chemicals.

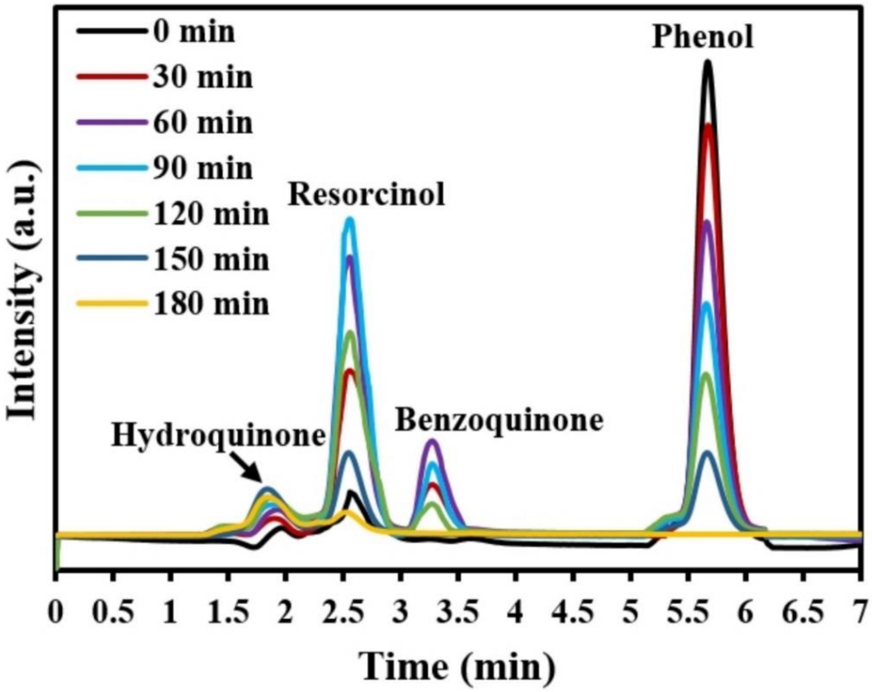

Figure 4.38: Time-dependent HPLC chromatogram of phenol aqueous solution over the Pd-BFO nanocomposite (Light intensity = 105 W; [Phenol] = 5.0 mg/L; catalyst loading = 1.0 g/L; solution pH = 7.0).

The HPLC findings suggested that the phenol degradation pathway involved complex multistage processes as exhibited in Figure 4.39. Initially, the phenol was adsorbed on the surface of Pd-BFO nanocomposite, which was then activated by the oxidation reaction with the •OH radicals based on the radical scavenger findings in Section 4.3.1. The –OH group of phenol tended to donate an *e*− and regarded as a powerful group for *ortho-para* aiming aromatic ring (Al-hamdi et al., 2016; Liu et al., 2013). Hence, the phenol would readily be reacted with the •OH radicals to generate various intermediates for example hydroquinone, catechol, resorcinol and benzoquinone (Al-sabahi et al., 2016; Turki et al., 2015).

Liu et al., (2013) stated that the •OH radicals can swap the –H possibly at two C3 and C5 locations and generate resorcinol intermediates. The resorcinol intermediates were then further oxidized to *1,4-benzoquinone* and *1,2-benzoquinone*. The hydroquinone, resorcinol and benzoquinone intermediated were well matched with the RT obtained in Figure 4.38. The *1,2-benzoquinone* was a conjugated ketone, which could be oxidized to muconic acid as a result of the covalent C–C bond breakage among the two carbonyls. In the meantime, the C=C bond of *1,4-benzoquinone* was also oxidized into muconic acid. The muconic acid was then undergoing into further photocatalytic degradation to yield other aliphatic acids such as maleic, oxalic, formic acids and eventually mineralized into the H_2O and CO_2 (Villasenor et al., 2002; Liu et al., 2019; Wang et al., 2005). Additionally, the initial solution pH in this study shifted from pH 5.6 to pH 4.5, revealing that the acidic compounds with the smaller molecular weight were produced during the photodegradation of phenol.

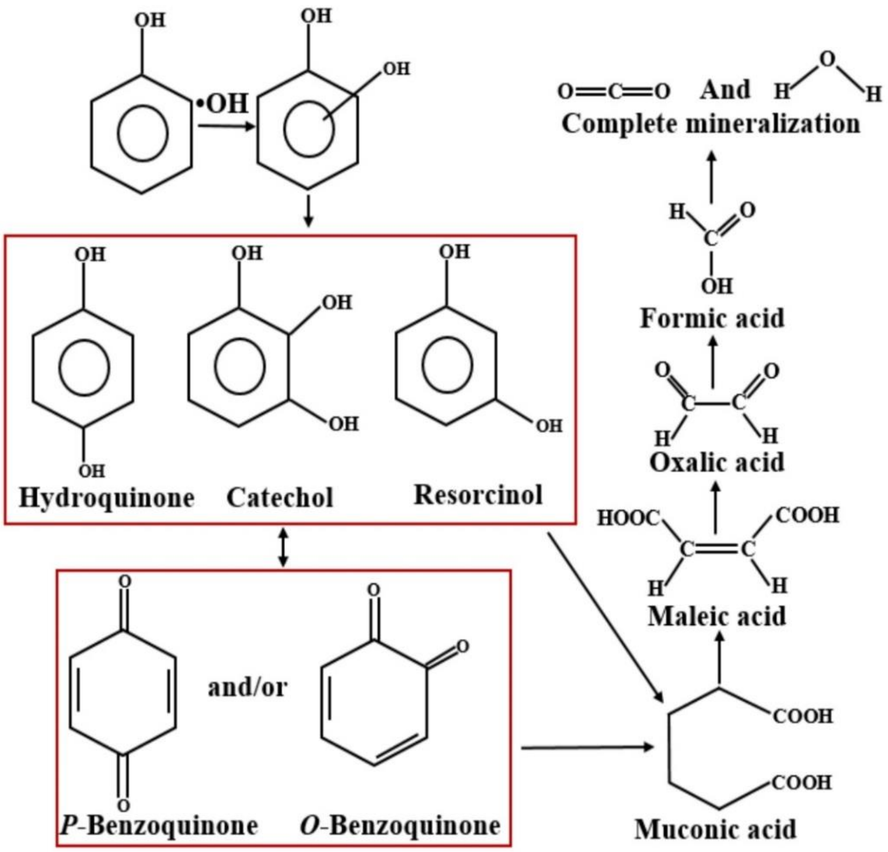

Figure 4.39: Phenol degradation with reaction pathway during the photodegradation reaction.

4.6.2 Mineralization of phenol

The COD analysis was performed to study the mineralization extent of the phenol over 2 wt% Pd-BFO nanocomposite under the irradiation of visible light. The experiment was executed using photocatalyst dosage of 1 g/L, phenol concentration of 5 mg/L and solution pH of 7.0. The COD removal of phenol was presented in Figure 4.40. It was witnessed that the COD removal was gradually increased during the photodegradation of phenol. The COD removal efficiency was 100% after 210 min of light irradiation. It was detected that the COD removal took a bit longer time than the photodegradation. The difference among the COD and photodegradation suggested that there were still some intermediates present in the reaction mixture as also proved by the HPLC findings. Hence, more time was need for the complete mineralization.

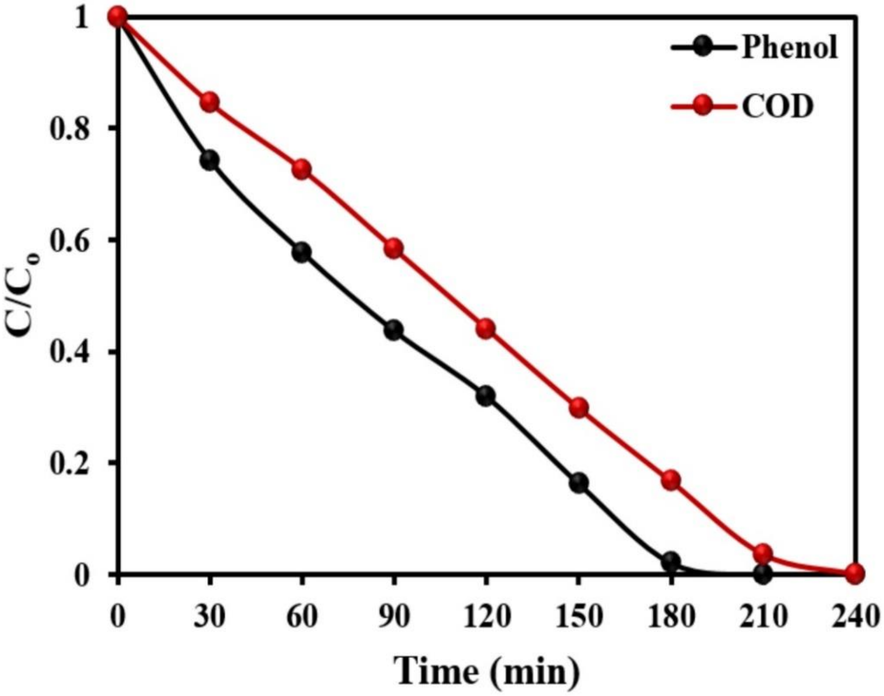

Figure 4.40: Parallel observation of phenol and COD concentration profile against the reaction time over Pd-BFO nanocomposites (Light intensity = 105 W; [Phenol] = 5.0 mg/L; photocatalyst dosage = 1.0 g/L; pH = 7.0).

4.7 Kinetic study

4.7.1 Determination of kinetic order

In heterogeneous photocatalysis, the rate of a chemical reaction is directly proportional to the adsorption of the reactants and desorption of the products from the surface of the photocatalyst. Gaya, (2014) stated that the integral differential rate equations provided integral rate laws, which can be exhibited by the degradation of contaminants that go through the photocatalytic process. In other words, the rate of reaction equations involved the concentration, where $-r_A$ is the rate of reactants consumption as presented in equation (4.10).

$$-r_A = \frac{d[A]}{dt} = k\,[\text{reactants concentration}]^n \qquad (4.10)$$

Where k, n and t are the rate constant, order of the reaction and the reaction time (min), respectively. The kinetic order for the photodegradation of MG dye and phenol was performed. Table 4.3 presents the rate equation related to the 0th-, 1st-, 2nd- and 3rd-order reaction relating the single reactant.

Table 4.3: Order of reaction and rate law for the photoreaction relating a single reactant (Gaya, 2014).

Reaction orders	**Rate law**	**Integrated equations**	**Reaction rate (units)**
0th-order	$-r = kC^o$	$C = -C + kt$	$\{k\} = \frac{mol}{L.\min}$
1st-order	$-r = kC^1$	$\ln \frac{C_o}{C} = kt$	$\{k\} = \frac{1}{\min}$
2nd-order	$-r = kC^2$	$\frac{1}{C} = kt + \frac{1}{C_o}$	$\{k\} = \frac{L}{mol.\min}$
3rd-order	$-r = kC^3$	$\frac{1}{C^2} = kt + \frac{1}{C^2{}_o}$	$\{k\} = (\frac{L}{mol})^2.(\frac{1}{\min})$

where $-r$, k, C, C_o and t are the reaction rate, observed rate constant, concentration of pollutants at time t (mg/L), initial concentration (mg/L) and reaction time (min), respectively.

Then, the equations stated in Table 4.4 were applied to determine the degree of each order. Table 4.5 depicts the various order of reaction values for the MG dye degradation. It can be seen that the values of R^2 for 0th-order reaction were ranged among 0.8568−0.9632, rate of reaction for 1st-order were ranged among 0.9276−0.9964, 2nd-order were ranged among 0.4904−0.7404 and 3rd-order were ranged among 0.3448−0.7015. Hence, these results clearly suggested that the best fitted visible light photodegradation of MG dye using Pd-BFO nanocomposite was the first-order reaction model. Moreover, Table 4.5 presents the determined reaction orders for phenol degradation using Pd-BFO nanocomposite. The values of R^2 for 0th-order reaction were ranged among 0.724−0.966, rate of reaction for 1st-order were ranged among 0.944−0.9987, 2nd-order were ranged among 0.3598−0.8571 and 3rd-order were ranged among 0.3052−0.712. Once again, the 1st-order reaction was proven the finest fitted model for phenol degradation using Pd-BFO nanocomposite. Various literature reports also applied the 1st-order reaction kinetics on the degradation of organic contaminants using BFO based photocatalysts (Bhoi & Mishra, 2018; Li et al., 2012; Pang et al., 2019; Zhang et al., 2017).

4.7.2 Kinetic modeling

The MG dye and phenol degradation reaction over coral-like Pd-BFO nanocomposite are known to be a heterogeneous photocatalytic reaction. According to the literature reports, the first order-kinetic reaction is commonly accommodated by the Langmuir-Hinshelwood (L-H) kinetic model (Chin et al., 2018; Soltani & Entezari, 2013). Fitting the MG dye and phenol degradation kinetics resulted in the first-order reaction, which suggested that the L-H model can be useful for the MG/phenol degradation kinetics over Pd-BFO nanocomposite. The L-H expression that illuminates the kinetics of heterogeneous photocatalytic reaction is given by equation (4.11).

$$r = -\frac{dc}{dt} = \frac{kKC}{1 + KC} \tag{4.11}$$

where, r is the rate of reaction of MG dye and phenol degradation ($mgL^{-1}min^{-1}$), C is MG dye and phenol concentration (mgL^{-1}), t is the irradiation time, k is the reaction rate constant ($mgL^{-1}min^{-1}$) and K is the adsorption equilibrium of MG dye and phenol ($1/mgL^{-1}$).

The basic assumptions in the L-H model are the adsorption of the substrate on the photocatalyst surface and then undergoes a bimolecular reaction. The L-H model consists of three steps, the first one is adsorption of the reactants followed by the surface reaction and lastly is desorption of the products. The above-stated equation can be integrated and rearranged as equation (4.12).

$$\ln\frac{C_o}{C} + K(C_o - C) = kKt \tag{4.12}$$

When the substrate concentration was in millimole (mMol) the term $(Co-C) < 1$, the K can be neglected, and the MG dye/phenol can follow the 1st-order equation as given below (Equation 4.13) (Kumar et al., 2008; Zhou et al., 2017).

$$\ln\frac{C_o}{C} = kKt = k_{app}t \tag{4.13}$$

where, k_{app} (1/min) is the apparent rate constant for the 1st-order equation.

In the present study, the above stated L-H model was utilized and the photocatalytic rate constants were estimated based on graphical method with the help of 1st-order differential equation. The photocatalytic degradation of MG and phenol at various solution pHs were performed using the initial substrate concentration of 5 mg/L, photocatalyst dosage of 1 g/L for phenol and 1.5 g/L for MG dye and the results are shown in Table 4.6. The rate constant k can be estimated from the slope of the chart among the time vs. $ln(Co/C)$.

Table 4.4: Calculation of the rate and order of reaction for various initial MG solution pHs under visible light irradiation.

Reaction order	**Solution pH of MG dye**							
	pH 3		**pH 5.45 (Natural)**		**pH 7**		**pH 9**	
	k	**R^2**	***k***	**R^2**	***k***	**R^2**	***k***	**R^2**
Zero-order ($\frac{mol}{L.\text{min}}$)	-0.0191	0.8568	-0.0246	0.9532	-0.0262	0.9632	-0.0209	0.9454
First-order ($\frac{1}{\text{min}}$)	0.0125	0.9964	0.0165	0.9498	0.0207	0.9376	0.0121	0.9894
Second-order ($\frac{L}{mol.\text{min}}$)	0.0177	0.4904	0.018	0.7015	0.0229	0.7404	0.0108	0.707
Third-order $\{(\frac{L}{mol})^2.(\frac{1}{\text{min}})\}$	0.1047	0.3448	0.018	0.7015	0.0771	0.5861	0.0108	0.707

Table 4.5: Calculation of the rate and order of reaction for various initial phenol solution pHs under visible light.

Reaction order	**Solution pH of phenol**							
	pH 3		**pH 5.4 (Natural)**		**pH 7**		**pH 9**	
	k	***R^2***	***k***	***R^2***	***k***	***R^2***	***k***	***R^2***
Zero-order ($\frac{mol}{L.\min}$)	-0.016	0.966	-0.0198	0.8047	-0.0191	0.804	-0.02	0.724
First-order ($\frac{1}{\min}$)	0.0061	0.9983	0.0153	0.9877	0.0181	0.944	0.014	0.9987
Second-order ($\frac{L}{mol.\min}$)	0.0027	0.8571	0.0303	0.4399	0.0397	0.4634	0.0363	0.3598
Third-order $\{(\frac{L}{mol})^2.(\frac{1}{\min})\}$	0.0027	0.712	0.2828	0.349	0.4001	0.3867	0.5296	0.3052

Table 4.6. R^2 and k values under various MG dye and phenol solutions pH using 1st-order kinetics.

Solution pH	**MG dye**		**Phenol**	
	k	R^2	k	R^2
3	0.0125	0.9964	0.0061	0.9983
5.4	0.0165	0.9498	0.0153	0.9877
7	0.0207	0.9376	0.0181	0.944
9	0.0121	0.9894	0.014	0.9987

It can be witnessed that when the solution pH was enhanced from 3.0 to 7.0, the *k* values first increased until a certain value and with a further rise in the solution pH to 9.0, it decreased. Similar kind of observations were also commonly presented in the literature (Habibi-yangjeh et al., 2019; Singh et al., 2019; Yang et al., 2019). It can also be witnessed that the MG dye and phenol degradation had a good correlation coefficient values in the range between 0.9376−0.9964 and 0.944−0.9987, respectively, suggesting that the photodegradation rates followed the L−H kinetic model. Hussain et al., (2018) studied the kinetics of the visible light active pure BFO nanoparticle for the photocatalytic degradation of aniline. Their rate plot gives a straight linear line, which confirmed the well fitted L−H kinetic model. Chaiwichian et al., (2017) studied the kinetic analysis on the degradation of MB and RhB dyes using $BiFeO_3/Bi_2WO_6$ nanocomposites. They establish that the photodegradation kinetics for MB and RhB dyes also followed the L−H model.

4.8 Electrical energy consumption

Besides the higher photoactivity, there were several important factors should be considered in the aqueous wastewater treatment, such as operating cost, safety, regulations, and etc (Rahman et al., 2017). Among all these factors, the cost is the utmost important factor. As the photocatalysis is an electric-energy intensive process, electrical energy consumption can present a main portion of the operating cost. Bolton et al., (2001) proposed a useful concept of E_{EO} for pseudo-first-order kinetic reactions to calculate the electrical energy consumed during the photocatalytic process. The E_{EO} can be defined as the electrical energy required in kilowatt per hour (kWh) to degrade a pollutant by one order of degree in 1 m^3 wastewater. Typically, E_{EO} values can be estimated by the following equation (Konstantina et al., 2018; Murgolo et al., 2017).

$$E_{EO} = \frac{P \times t \times 1000}{V \times 60 \times (\log \frac{C_i}{C_f})} \tag{4.14}$$

$$\log(\frac{C_i}{C_f}) = k \times t \tag{4.15}$$

where, E_{EO} is the electrical energy per order (kWh m^{-3} order^{-1}), P is the electric power entering the photocatalytic system (kW), t is the light irradiation time (min), V is the volume (L) of wastewater, k is the pseudo first order rate constant (min^{-1}), C_i and C_f are the initial and final concentration of pollutants (mg/L). From equations (4.14) and (4.15), the E_{EO} can be written as follow:

$$E_{EO} = \frac{38.4 \times P}{V \times k} \tag{4.16}$$

The experiments were executed using the similar solution pH and initial concentration of organic pollutants for pure BFO, Pd-BFO and commercial TiO_2 under the irradiation of visible light. By considering the total energy entering the photocatalytic system was consistent for each photocatalyst during the degradation reaction, the estimated E_{EO} values are listed in Table 4.7. These values exhibited that the Pd-BFO nanocomposite decreased the E_{EO} values for the photodegradation of MG dye and phenol compared with the pure BFO as well as commercial TiO_2. The obtained E_{EO} values for photodegradation of MG dye and phenol using Pd-BFO nanocomposite were 1947.82 and 2115.38 $kWhm^{-3}\,order^{-1}$, respectively. The higher E_{EO} value for phenol than those of the MG dye was due to its more stable molecular structure. A few reports in the literature had also applied this useful figure of merit for different organic pollutants to make a cost comparison. For instance, Lv et al., (2012) investigated the degradation of methyl orange using CdS-TiO_2 and Au-CdS-TiO_2, where E_{EO} value was lowered from 57900 to 11552 $kWhm^{-3}\,order^{-1}$ after loading Au nanoparticles on CdS-ZnO surface. Li et al., (2015) had also studied the degradation of various organic pollutants methyl orange, amoxicillin and 3-chlorophenol by TiO_2 photocatalyst. These organic pollutants were effectively degraded with E_{EO} values ranged between 73100 to 25200 $kWhm^{-3}order^{-1}$ depending upon the initial concentration. It can be seen that the calculated E_{EO} values of Pd-BFO nanocomposite in the current study were considerably lower than those presented in the literature, which further confirmed the Pd-BFO nanocomposite was a potential cost-effective photocatalyst for the degradation of aqueous organic pollutants.

Table 4.7: E_{EO} values of phenol and MG dye degradation systems using various photocatalysts.

Pollutant	**Photocatalyst**	**k (min^{-1})**	**E_{EO} ($kWhm^{-3}$ $order^{-1}$)**
MG dye	Pure BFO	0.0069	5843.47
	Pd-BFO	0.0207	1947.82
	Commercial TiO_2	0.0078	5169.23
Phenol	Pure BFO	0.0059	6833.89
	Pd-BFO	0.0182	2115.38
	Commercial TiO_2	0.0064	6300

4.9 Sunlight photocatalytic degradation of MG dye and phenol by Pd-BFO photocatalysts

In the present study, the MG dye and phenol were also degraded under direct sunlight irradiation. Figure 4.41 depicts the photodegradation efficiencies of pure BFO, 2 wt% Pd-BFO nanocomposite and commercial TiO_2 for 6 min of direct sunlight irradiation. The results suggested that the photolysis of MG dye and phenol under sunlight irradiation were almost negligible. Nonetheless, in the presence of the applied photocatalysts, a great deal of the organic pollutants were degraded quickly. The order of the obtained photocatalytic activity were 2 wt% Pd-BFO > commercial TiO_2 > pure BFO.

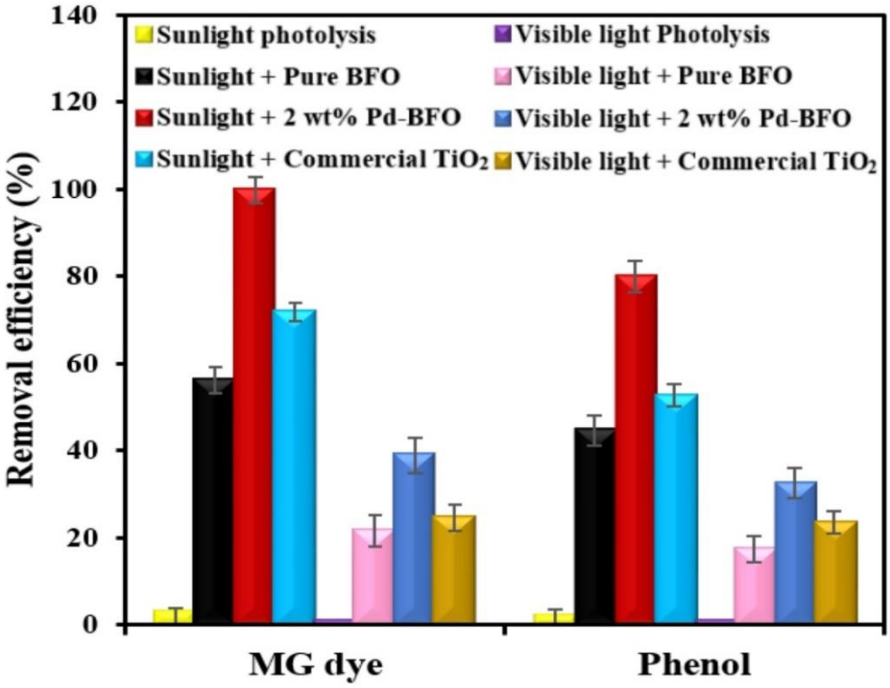

Figure 4.41: Photodegradation of MG dye and phenol under direct sunlight irradiation (irradiation time = 7 min) and visible light irradiation (irradiation time = 30 min) over numerous photocatalysts ([MG dye/Phenol] = 5 mg/L; photocatalyst dosage = 1.5 g/L; $pH_{MG\ dye}$ = 7.0 and pH_{Phenol} = 7.0).

It was also witnessed that the photocatalytic performances of every photocatalysts under the irradiation of direct sunlight were several times higher than those irradiated under visible light. The extremely high photocatalytic efficiencies can be explained in terms of light intensity measured using a digital lux meter. The direct sunlight irradiation possesses the light intensity of 9.0×10^4 lux, which was several times higher than the applied visible light (7.04×10^3 lux). The higher intensity of sunlight light had a higher possibility of collision among the photons and photocatalyst active sites, which ultimately improved the photocatalytic efficiency. A linear relationship between the light intensity and photocatalytic efficiencies were also presented in literatures (Lin et al., 2015; Li et al., 2015; Bora and Mewada, 2017).

The chemical structure of organic pollutants also played a vital part in their photodegradation. As discussed in photocatalytic mechanism section 4.3.3, the photodegradation process was started by the •OH radical attacking on the organic pollutants. In the case of the MG dye, Magdalane et al., (2017) stated that the •OH radicals initially reacted with the MG dye and break the C−N bond of MG dye. On the other hand, the •OH radicals attacked the C-H bond of the phenol aromatic ring and converted into the hydroquinone, catechol and resorcinol intermediates as recorded in the HPLC analysis. According to the Dominguez et al., (2014) higher energy is required to break the aromatic ring than the simple C−N bond. Hence, the breaking of C−N bond in MG dye was much easier compared with the C-H bond in phenol molecules. 100% MG dye was degraded within 7 min of sunlight irradiation, while photodegradation of phenol was around 81.3% under the similar irradiation time.

4.10 Real textile wastewater degradation by using Pd-BFO photocatalysts

Textile industry generates a large volume of wastewater containing dyes, non-biodegradable organics and other textile processing chemicals, which make it difficult to treat. The colored textile wastewater mainly consists of high COD, suspended solids, surfactants, chlorinated aromatic compounds and heavy metals, for example chromium and copper (Jorfi et al., 2016; Vafaee et al., 2017). Hence, to understand the composition of textile wastewater, it is extremely important to characterize the wastewater before treatment. Table 4.8 depicts the characterization of the as-received real textile wastewater. From the table, it can be seen that the textile wastewater consisted of high COD, biological oxygen demand (BOD_5), turbidity, total suspended solids (TSS), colour, ammoniacal nitrogen (NH_3-N) and pH. The concentration of COD, BOD_5, turbidity, TSS, colour NH_3-N were 2266 mg/L, 316 mg/L, 92.45 NTU, 1074 mg/L, 725 Pt-Co and 3.92 mg/L respectively, while the pH was 12.96.

Table 4.8. Summary of the calculated real textile wastewater quality parameters before and after Pd-BFO nanocomposite treatment.

Parameter	**As-received wastewater**	**After 240 min visible-light**	**Removal efficiency (%)**
COD (mg/L)	2266	320	85.87
(BOD_5) (mg/L)	316	44	86.07
Turbidity (NTU)	92.45	13.7	85.18
Colour (Pt-Co)	725	98	86.48
TSS (mg/L)	1074	170	84.14
NH_3─N (mg/L)	3.92	0.8	79.59
pH	12.96	7.08	─

Adequate mineralization of textile wastewater to CO_2, H_2O and mineral ions should be achieved using photocatalytic process before releasing it to the environment. Figure 4.42 depicts the COD, BOD_5 and BOD_5/COD ratios of the real textile wastewater after 240 min of Pd-BFO nanocomposites photocatalytic treatment. The final concentration of both COD and BOD_5 were reduced about 85.87% and 86.45%, respectively. The low initial BOD_5/COD ratio of 0.14

presented that real textile wastewater was non-biodegradable in nature and it was important to consider some advanced treatment process. In the present study, the Pd-BFO nanocomposites photodegradation of the textile wastewater improved the biodegradability index to 0.98. Therefore, the purified water showed obvious improvement in the biodegradability as confirmed from the enhancement on the final BOD_5/COD ratio.

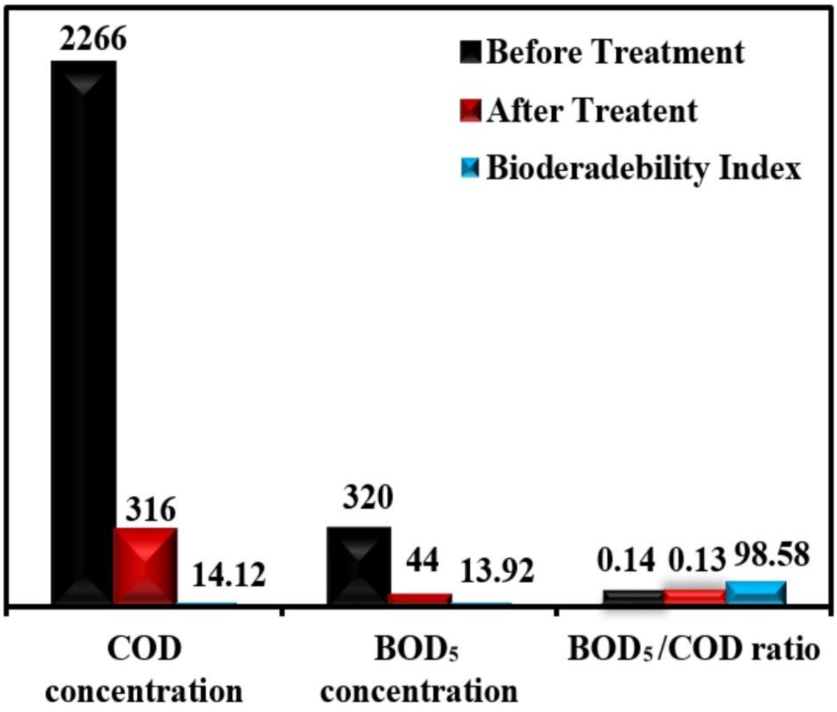

Figure 4.42: COD, BOD_5, and BOD_5/COD ratio of the real textile wastewater before and after photodegradation reaction using 2 wt% Pd-BFO nanocomposite.

Table 4.8 shows after photocatalytic treatment values of other investigated quality parameters of real textile wastewater. It was witnessed that the NH_3-N, colour, TSS and turbidity degradation efficiencies were 79.59%, 86.48%, 84.14% and 85.18%, respectively. It can be credited to the presence of mixtures of dye and different other contaminants such as Cl^- ions as well as dissolved organic matters in real textile wastewater. Different inorganic ions and functional groups of dyes can change the photocatalytic mechanism, which caused in a complex degradation reaction (Chakrabarti & Dutta, 2004). The final pH of the treated wastewater was decreased from pH 12.96 to pH 7.08. Stylidi et al., (2004) stated that the decrease in the pH upon the photodegradation of dyes wastewater was due to the production of different aliphatic acids such as formic, lactic, maleic, acetic and others resulted from the opening of the aromatic ring. In the current study, the decrease in the pH value upon the real textile wastewater treatment might also be connected with the discharge of the short aliphatic acids. Therefore, the synthesized Pd-BFO nanocomposite were undoubtedly useful for the treatment of real textile wastewater.

Chapter 5

Conclusion and future recommendations

5.1 Conclusion

Herein, 3D coral-like NM-doped BFO nanocomposite have been successfully synthesized via two-steps hydrothermal technique. The synthesized NM-BFO nanocomposite were characterized using XRD, FESEM, EDX, EDX mapping, TEM, XPS, UV-Vis DRS, FTIR, PL and M-H loop analyses. The diffraction peak of XRD analysis at 22.6°, 32.2°, 32.4°, 39.9°, 45.8°, 51.9°, 52.4°, 56.7°, 58.1°, 67.2°, 67.8°, 71.1° and 71.5° indicated that the as-synthesized NM-BFO nanocomposite exhibited a rhombohedral perovskite structure with high crystallinity. The FESEM and TEM analyses proved that the NM were homogeneously dispersed on the coral-like BFO structure with the particle size diameter ranged between 110−130 nm. Moreover, the presence of each NM on the surface of coral-like BFO was identified by EDX analysis. The XPS analysis for the 2 wt% Pd-BFO nanocomposite demonstrated that the Pd nanoparticles were present in the metallic form (Pd^0) on the surface of coral-like BFO, which was also consistent with the XRD analysis. The synthesized NM-BFO nanocomposite decreased the band gap values of BFO in the range of 2.05−2.27 eV (from 2.50 eV for pure BFO), which was very helpful for the improved light absorption abilities. Compared to the pure BFO, the PL intensities of NM-BFO nanocomposite showed a dramatically declined. As for Pd-BFO nanocomposite, the PL intensity was the lowermost, which suggested the highest $e^{-}-h^{+}$ pairs separation efficiency.

The photocatalytic activities of the NM-BFO nanocomposite were investigated by the degradation of MG dye and phenol under visible light irradiation. The results suggested that the 2 wt% NM-BFO nanocomposites displayed much improved photocatalytic activities compared with the pure BFO and commercial TiO_2. The photodegradation activities of 2 wt% NM-BFO nanocomposites were in the order of 2 wt% Pd-BFO > 2 wt% Pt-BFO > 2 wt% Ag-BFO. The photocatalytic activities of NM-BFO nanocomposite with various NM dopings were also investigated, and the results proposed that the 2 wt% Pd-doping, 0.5 wt% Pt-doping and 3 wt% Ag-doping showed the best photocatalytic activities. The increased photocatalytic activity could be credited to the appropriate amount of NM dopings that enhanced the e^{-} trapping ability, which was helpful for the generation and transfer of the photogenerated $e^{-}-h^{+}$ pairs at the interface. A detailed possible degradation mechanism was proposed with the help of photoelectrochemical measurements, radical scavenger studies and TA–PL experiments. The photoelectrochemical measurement results suggested that the 2 wt% Pd-BFO nanocomposite had the lowest $e^{-}-h^{+}$ pairs recombination rate among all the synthesized photocatalysts, which promotes its photocatalytic abilities. The radical scavengers study indicated that h^{+}, H_2O_2 and •OH radicals were the main active species for the Pd-BFO photocatalytic system. Among the 2 wt% NM-BFO nanocomposite, Pd-BFO nanocomposite presented the most suitable heterojunction, led to the highest $e^{-}-h^{+}$ pairs separation efficiency as well as an improvement to generate •OH radicals to some extent.

The effect of process parameters such as intensity of light, photocatalyst dosage, initial substrate concentration, solution pH, humic acid and different anion present in wastewater were also investigated. Under optimized conditions, 100% COD removal of MG dye was achieved using the initial concentration of 5 mg/L, pH 7 and photocatalyst dosage of 1.5 g/L after 180 min of visible light irradiation. The ferromagnetic properties of the NM-BFO nanocomposites were helpful in their separation from the aqueous medium during the recycling experiment. After the sixth cyclic run, the Pd-BFO nanocomposite was still able to degrade more than 95% MG dye, which demonstrates that the Pd-BFO nanocomposites have excellent reusability. Besides, the ICP-MS test detected only a small concentration of metallic Pd^{o} in the range from 0.0327 mg/L to 0.0237 mg/L during the six recycling experiments.

Several degradation intermediates, such as hydroquinone, resorcinol and benzoquinone were detected using HPLC on the phenol photodegradation. Based on these intermediates, a possible phenol degradation pathway was also proposed. The kinetic analysis of the degradation of the aqueous organics over Pd-BFO were well fitted by 1st-order kinetics characterized by the L-H model. The E_{EO} results for visible light degradation of MG dye and phenol showed that the Pd-BFO was beneficial in reducing electrical energy required for wastewater treatment than those of pure BFO and commercial TiO_2. Additionally, the Pd-BFO nanocomposite was applied under direct sunlight to degrade organic pollutants, and its photodegradation activity was again considerably higher to that those of pure BFO and commercial TiO_2 under similar conditions. Finally, using the optimized process conditions, the Pd-BFO nanocomposite was also applied for the photodegradation of real textile wastewater. The findings suggested that 85.87% COD removal was achieved after 4 h of visible light irradiation. The removal efficiencies of other quality parameters such as BOD_5, TSS, colour, turbidity, NH_3-H and pH were also found to be 86.45%, 84.14%, 86.48%, 85.15%, 79.59% and 7.08, respectively.

5.2 Future recommendations

After completion of the current research, there are still numerous important engineering characteristics which required attention in the future photocatalytic studies.

1. Given the outstanding photodegradation efficiencies of NM-BFO nanocomposite in the present research, other noble metals and bimetallic noble metals doping should be investigated to further enhanced the photodegradation efficiency of BFO under visible and direct sunlight irradiation.
2. The future work should also focus on the synthesis of semiconductor coupling between the BFO and metal-semiconductor co-coupling as it

can further enhance the light absorption ability in the visible light region leading to the improved $e^{-}-h^{+}$ pairs separation efficiency.

3. To further evaluate the photocatalytic performance, the toxicity removal using NM-BFO nanocomposite after the degradation of MG dye and phenol should be monitored in the treated solution.
4. Future studies should be also focused on the scale-up of continuous mode photoreactor for practical application.
5. The NM-BFO nanocomposite should be also investigated for other applications such as antibacterial work and air purification.

LIST OF REFERENCES

Abou, H., Essamlali, Y., Amadine, O., & Daanoun, K. (2017). Green synthesis of Ag/ZnO nanohybrid using sodium alginate gelation method. *Ceramics International*, *43*, 13786–13790.

Ai, C., Zhou, D., Wang, Q., Shao, X., & Lei, Y. (2015). Optimization of operating parameters for photocatalytic degradation of tetracycline using In_2S_3 under natural solar radiation. *Solar Energy*, *113*, 34–42.

Ajmal, A., Majeed, I., Malik, R. N., Idriss, H., & Nadeem, M. A. (2014). Principles and mechanisms of photocatalytic dye degradation on TiO_2 baed photocatalysts: a comparative overview. *RSC Advances.*, *4*, 37003–37026.

Al-hamdi, A. M., Sillanpaa, M., Bora, T., & Dutta, J. (2016). Efficient photocatalytic degradation of phenol in aqueous solution by SnO_2: Sb nanoparticles. *Applied Surface Science*, *370*, 229–236.

Al-sabahi, J., Bora, T., Al-abri, M., & Dutta, J. (2016). Controlled defects of zinc oxide nanorods for efficient visible light photocatalytic degradation. *Materials*, *9*, 238–248.

Alamelu, K., & Ali, J. B. M. (2018). TiO_2-Pt composite photocatalyst for photodegradation and chemical reduction of recalcitrant organic pollutants. *Journal of Environmental Chemical Engineering*, *6*, 5720–5731.

An, J., Zhang, G., Zheng, R., & Wang, P. (2016). Removing lignin model pollutants with $BiFeO_3$-gC_3N_4 compound as an efficient visible-light-heterogeneous Fenton-like catalyst. *Journal of Environmental Sciences*. *48*, 218−229.

An, J., Zhu, L., Wang, N., Song, Z., Yang, Z., Du, D., & Tang, H. (2013). Photo-fenton like degradation of tetrabromobisphenol A with graphene $BiFeO_3$ composite as a catalyst. *Chemical Engineering Journal*, *219*, 225–237.

Anirudhan, T. S., Shainy, F., & Christa, J. (2016). Synthesis and characterization of polyacrylic acid-grafted-carboxylic graphene/titanium nanotube composite for the effective removal of enrofloxacin from aqueous solutions: Adsorption and photocatalytic degradation studies. *Journal of Hazardous Materials*, *324*, 177–130.

Ao, D., Zhang, J., & Liu, H. (2018). Visible-light-driven photocatalytic degradation of pollutants over Cu-doped NH_2-MIL-125(Ti). *Journal of Photochemistry & Photobiology, A: Chemistry, 364*, 524–533.

APHA, AWWA, & WPCF. (2005). Standard Methods for the Examination of Water and Wastewater, twenty-first ed., American Public Health Association, Washington, D.C., USA.

Aravind, P., Selvaraj, H., Ferro, S., & Sundaram, M. (2016). An integrated (electro- and bio-oxidation) approach for remediation of industrial wastewater containing azo-dyes: Understanding the degradation mechanism and toxicity assessment. *Journal of Hazardous Materials*, *318,* 203–215.

Asghar, A., Raman, A. A. A., & Daud, W. M. A. W. (2015). Advanced oxidation processes for in-situ production of hydrogen peroxide/hydroxyl radical for textile wastewater treatment: A review. *Journal of Cleaner*

Production, *87*, 826–838.

Association, A. P. H., Association, A. W. W., Federation, W. P. C., & Federation, W. E. (1915). *Standard methods for the examination of water and wastewater* (Vol. 2). American Public Health Association.

Bai, S., Jiang, J., Zhang, Q., & Xiong, Y. (2015). Steering charge kinetics in photocatalysis: intersection of materials syntheses, charecterization techniques and theoratical simulations. *Chemical Society Reviews*, *44*, 2893−2939.

Bai, X., Yang, L., Hagfeldt, A., Johansson, E. M. J., & Jin, P. (2019). D35-TiO_2 nano-crystalline film as a high performance visible-light photocatalyst photocatalyst towards the degradation of bis-phenol A. *Chemical Engineering Journal*, *355*, 999–1010.

Bansal, P., Verma, A., Aggarwal, K., Singh, A., & Gupta, S. (2016). Investigations on the Degradation of an Antibiotic Cephalexin using Suspended and Supported TiO_2: Mineralization and Durability Studies. *The Canadian Journal of Chemical Engineering*, *94*, 1269–1276.

Behnajady, M. A., Modirshahla, N., & Hamzavi, R. (2006). Kinetic study on photocatalytic degradation of C. I. Acid Yellow 23 by ZnO photocatalyst. *Journal of Hazardous Materials*, *133,* 226–232.

Bel Hadjltaief, H., Omri, A., Ben Zina, M., Da Costa, P., & Galvez, M. E. (2015). Titanium dioxide supported on different porous materials as photocatalyst for the degradation of methyl green in wastewaters. *Advances in Materials Science and Engineering*, *2015,* 1−10.

Benyounes, A., Louisia, S., Axet, R., Mahfoud, Z., Kacimi, M., & Serp, P. (2015). Green alcohol oxidation on palladium catalysts supported on amphiphilic hybrid carbon nanotubes. *Catalysis Today*, *249*, 137–144.

Bethi, B., Sonawane, S. H., Bhanvase, B. A., & Gumfekar, S. P. (2016). Nanomaterials-based advanced oxidation processes for wastewater treatment: A review. *Chemical Engineering and Processing: Process Intensification*, *109*, 178–189.

Bharathkumar, S., Sakar, M., K., R. V., & Balakumar, S. (2015). Versatility of electrospinning in the fabrication of fibrous mat and mesh nanostructures of bismuth ferrite ($BiFeO_3$) and their magnetic and photocatalytic activities. *Phys. Chem. Chem. Phys.*, *17*, 17745–17754.

Bhattacharjee, A., Chakraborty, S., Mandol, K., Liu, L., & Choi, H. (2014). Optimization of process parameters during photocatalytic degradation of phenol in UV annular reactor, *Journal of Desalination and water treatment*, *54*, 2270–2279.

Bhoi, Y. P., & Mishra, B. G. (2018). Photocatalytic degradation of alachlor using type-II $CuS/BiFeO_3$ heterojunctions as novel photocatalyst under visible light irradiation. *Chemical Engineering Journal*, *344*, 391–401.

Bolton, J. R., Bircher, K. G., Tumas, W., & Tolman, C. A. (2001). Figures-of-merit for the technical development and application of advanced oxidation technologies for both electric and solar driven systems. *Pure and Applied Chemistry*, *73*, 627–637.

Bora, L. V., & Mewada, R. K. (2017). Visible/solar light active photocatalysts for organic effluent treatment: Fundamentals, mechanisms and parametric review. *Renewable and Sustainable Energy Reviews*, *76*, 1393–1421.

Boruah, P.K., Sharma, B., Karbhal, I., Shelke, M.V., Das, M.R., (2017). Ammonia-modified graphene sheets decorated with magnetic Fe_3O_4 nanoparticles for the photocatalytic and photo-Fenton degradation of phenolic compounds under sunlight irradiation, Journal of Hazardous Materials, 325, 90–100.

Boukhatem, H. Khalaf, H., Djouadi, L., Gonzalez, F.V., Navarro, R.M., Santaballa, J.A., Canle, M., (2017). Photocatalytic activity of mont-La(6%)-$Cu_{0.6}Cd_{0.4}S$ catalyst for phenol degradation under near UV visible light irradiation, *Applied Catalysis B: Environment, 211,* 114–125.

Borges, M. E., Sierra, M., Cuevas, E., García, R. D., & Esparza, P. (2016). Photocatalysis with solar energy: Sunlight-responsive photocatalyst based on TiO_2 loaded on a natural material for wastewater treatment. *Solar Energy*, *135*, 527–535.

Butler, E., Mulamba, O., Hung, Y., & Fu, Y. (2017). Impact of Wastewater Strength and Photocatalyst Loading on Decolourization of Acid Orange 7 by Co-Doped TiO_2. *Asian Journal of Chemistry*, *29*, 139–144.

Carra, I., Sánchez Pérez, J. A., Malato, S., Autin, O., Jefferson, B., & Jarvis, P. (2016). Performance of different advanced oxidation processes for tertiary wastewater treatment to remove the pesticide acetamiprid. *Journal of Chemical Technology and Biotechnology*, *91*, 72–81.

Caux, M., Fina, F., Irvine, J. T. S., Idriss, H., & Howe, R. (2017). Impact of the annealing temperature on Pt/g-C_3N_4 structure, activity and selectivity between photodegradation and water splitting. *Catalysis Today*, *287*, 182–

188.

Cavalcante, L. S., Sczancoski, J. C., Varela, J. A., Longo, E., Andr, J., & Rout, S. K. (2012). Photoluminescence Properties of Nanocrystals, *Journal of nanomaterials*, *2012*, 2012–2014.

Chaiwichian, S., Wetchakun, K., & Kangwansupamonkon, W. (2017). Novel visible-light-driven $BiFeO_3$-Bi_2WO_6 nanocomposites toward degradation of dyes. *Journal of Photochemistry & Photobiology, A: Chemistry*, *349*, 183–192.

Chakrabarti, S., & Dutta, B. K. (2004). Photocatalytic degradation of model textile dyes in wastewater using ZnO as semiconductor catalyst. *Journal of Hazardous Materials*, *112*, 269–278.

Chan, S. H. S., Wu, T. Y., Juan, J. C., & Teh, C. Y. (2011). Recent developments of metal oxide semiconductors as photocatalysts in advanced oxidation processes (AOPs) for treatment of dye waste-water. *Journal of Chemical Technology and Biotechnology*, *86*, 1130–1158.

Chandra, P., & Manoj, S. (2015). Raman spectroscopy and enhanced magnetic and dielectric properties of Pr and Ti codoped $BiFeO_3$ ceramics. *Journal of Materials Science: Materials in Electronics*, 530–538.

Chang, Y., Liu, Z., Shen, X., Zhu, B., Macharia, D. K., Chen, Z., & Zhang, L. (2018). Synthesis of Au nanoparticle-decorated carbon nitride nanorods with plasmon-enhanced photoabsorption and photocatalytic activity for removing various pollutants from water. *Journal of Hazardous Materials*, *344*, 1188–1197.

Chanu, T. I., Samanta, D., Tiwari, A., & Chatterjee, S. (2016). Effect of Reaction Parameters on Photoluminescence and Photocatalytic Activity of Zinc Sulfide Nanosphere Synthesized by Hydrothermal Route. *Applied Surface Science, 391,* 548–556.

Chauhan, S., Kumar, M., Chhoker, S., & Katyal, S. C. (2016). A comparative study on structural, vibrational, dielectric and magnetic properties of microcrystalline $BiFeO_3$, nanocrystalline $BiFeO_3$ and core--shell structured $BiFeO_3$@ SiO_2 nanoparticles. *Journal of Alloys and Compounds*, *666*, 454–467.

Chen, C. C., & Ting, F. (2017). Study on carbon quantum dots/$BiFeO_3$ heterostructures and their enhanced photocatalytic activities under visible light irradiation. *Journal of Materials Science: Materials in Electronics, 28*, 10019–10027.

Chen, F., Yang, Q., Li, X., Zeng, G., & Wang, D. (2017). Hierarchical assembly of graphene-bridged Ag_3PO_4/Ag/$BiVO_4$ (040) Z-scheme photocatalyst: An efficient, sustainable and heterogeneous catalyst with enhanced visible-light photoactivity towards tetracycline deg. *Applied Catalysis B, Environmental*, *200,* 330–342.

Chen, F., Yang, Q., Wang, Y., Yao, F., Ma, Y., & Huang, X. (2018). Efficient construction of bismuth vanadate-based Z-scheme photocatalyst for simultaneous Cr(VI) reduction and ciprofloxacin oxidation under visible light: Kinetics, degradation pathways and mechanism. *Chemical Engineering Journal*, *348*, 157–170.

Chen, H., Ku, Y., & Kuo, Y. (2007). Effect of Pt/TiO_2 characteristics on temporal behavior of o-cresol decomposition by visible light-induced photocatalysis. *Water Research*, *41*, 2069–2078.

Chen, J., Xiao, X., Wang, Y., & Ye, Z. (2019). Ag nanoparticles decorated WO_3/g-C_3N_4 2D/2D heterostructure with enhanced photocatalytic activity for organic pollutants degradation. *Applied Surface Science, 467–468*, 1000–1010.

Chen, W., Chan, A., Sun-waterhouse, D., Llorca, J., Idriss, H., & Waterhouse, G. I. N. (2018). Performance comparison of Ni/TiO_2 and Au/TiO_2 photocatalysts for H_2 production in different alcohol-water mixtures. *Journal of Catalysis, 367*, 27–42.

Chen, X., Wu, Z., Liu, D., & Gao, Z. (2017). Preparation of ZnO Photocatalyst for the Efficient and Rapid Photocatalytic Degradation of Azo Dyes. *Nanoscale Research Letters*, *12*, 4–13.

Cheng, S., Xu, Q., Hao, X., Wang, Z., Ma, N., & Du, P. (2017). Formation of nano-Ag/$BiFeO_3$ composite thin film with extraordinary high dielectric and effective ferromagnetic properties. *Journal of Materials Science: Materials in Electronics, 28*, 5652–5662.

Chin, Y.-H., Sin, J.-C., Lam, S.-M., & Mohamed, A. R. (2018). Preparation of - Nb_2O_5-decorated hierarchical porous ZnO microspheres with enhanced photocatalytic degradation of palm oil mill effluent. *Journal of Materials Science: Materials in Electronics*, *30*, 1739–1750.

Chong, M. N., Cho, Y. J., Poh, P. E., & Jin, B. (2015). Evaluation of Titanium dioxide photocatalytic technology for the treatment of reactive Black 5 dye in synthetic and real greywater effluents. *Journal of Cleaner Production*, *89*, 196–202.

Chowdhury, P., Nag, S., & Ray, A. K. (2017). Degradation of phenolic compounds through UV and visible-light-driven photocatalysis: technical and economic aspects. *Phenolic Compounds: Natural Sources, Importance and Applications*, 395.

Cui, H., Cao, Y., Jing, L., Luan, Y., & Li, N. (2014). Effects of Inorganic Acid Modification on Photocatalytic Performance of TiO_2 and Its Activity-Enhanced Mechanism Related to Adsorbed O_2. *ChemPlusChem*, *79*, 318–324.

Dariani, R. S., Esmaeili, A., Mortezaali, A., & Dehghanpour, S. (2016). Photocatalytic reaction and degradation of methylene blue on TiO_2 nano-sized particles. *Optik*, *127*(18), 7143–7154.

Das, S., & Srivastava, V. C. (2016). Microfluidic-based photocatalytic microreactor for environmental application: a review of fabrication substrates and techniques, and operating parameters. *Photochemical and Photobilogical Sciences*, *15*, 714–730.

Davididou, K, Hale, E., Lane, N., Chatzisymeon, E., Pichavant, A., & Hochepied, J. (2017). Photocatalytic treatment of saccharin and bisphenol-A in the presence of TiO_2 nanocomposites tuned by Sn (IV). *Catalysis Today*, *287*, 3–9.

Davididou, Konstantina, McRitchie, C., Antonopoulou, M., Konstantinou, I., & Chatzisymeon, E. (2018). Photocatalytic degradation of saccharin under UV-LED and blacklight irradiation Konstantina Davididou. *Journal of Chemical Technology and Biotechnology*, *93*, 269–276.

Deng, C., Gong, J., Zeng, G., Jiang, Y., Zhang, C., & Liu, H. (2016). Graphene–CdS nanocomposite inactivation performance toward Escherichia coli in the presence of humic acid under visible light irradiation. *Chemical Engineering Journal*, *284*, 41–53.

Deng, Y., Tang, L., Feng, C., Zeng, G., Wang, J., Zhou, Y., Feng, H. (2018). Construction of plasmonic Ag modified phosphorous-doped ultrathin g-C_3N_4 nanosheets/$BiVO_4$ photocatalyst with enhanced visible-near-infrared response ability for ciprofloxacin degradation. *Journal of Hazardous Materials*, *344*, 758–769.

Dhanalakshmi, R., Muneeswaran, M., Shalini, K., & Giridharan, N. V. (2016a). Enhanced photocatalytic activity of La-substituted $BiFeO_3$ nanostructures on the degradation of phenol red. *Materials Letters*, *165*, 205–209.

Di, L. J., Yang, H., Hu, G., Xian, T., Ma, J. Y., Jiang, J. L., Wei, Z. Q. (2014). Enhanced photocatalytic activity of $BiFeO_3$ particles by surface decoration with Ag nanoparticles. *Journal of Materials Science: Materials in Electronics*, *25*(6), 2463–2469.

Di, L., Yang, H., Xian, T., & Chen, X. (2017). Enhanced Photocatalytic Activity of $NaBH_4$ Reduced $BiFeO_3$ Nanoparticles for Rhodamine B Decolorization. *Materials*, *10*(10), 1118–1129.

Dominguez, S., Ribao, P., Rivero, M. J., & Ortiz, I. (2014). Influence of radiation and TiO_2 concentration on the hydroxyl radicals generation in a photocatalytic LED reactor. Application to dodecylbenzenesulfonate degradation. *Applied Catalysis B, Environmental*, *178*, 165–169.

Dong, F., Li, P., Zhong, J., Liu, X., Zhang, Y., Cen, W., & Huang, H. (2016).

Simultaneous Pd^{2+} doping and Pd metal deposition on $(BiO)_2CO_3$ microspheres for enhanced and stable visible light photocatalysis. *Applied Catalysis A: General, 510,* 161–170.

Dong, S., Liu, Y., Yang, S., Jiang, T., Yin, Y., & Li, X. (2013). Manipulation of morphologies and magnetic properties for $Bi_{4.2}K_{0.8}Fe_2O_9$ nanostructures. CrystEngComm, 15, 9057–9063.

Dugandžić, A. M., Tomašević, A. V., Radišić, M. M., Šekuljica, N., Mijin, D., & Petrović, S. D. (2017). Effect of inorganic ions, photosensitisers and scavengers on the photocatalytic degradation of nicosulfuron. *Journal of Photochemistry and Photobiology A: Chemistry, 336,* 146–155.

Edelmannova, M., Lin, K., Wu, C. S., Troppova, I., & Libor, C. (2018). Photocatalytic hydrogenation and reduction of CO_2 over CuO/TiO_2 photocatalysts. *Applied Surface Science*, *454*, 313–318.

Elhalil, A., Tounsadi, H., Elmoubarki, R., Mahjoubi, F.Z., Farnane, M., Sadiq, M., Abdennouri, M., Qourzal, S., Barka, N., (2016). Factorial experimental design for the optimization of catalytic degradation of malachite green dye in aqueous solution by Fenton process, *Water Resources and Industry, 15,* 41–48.

Eren, Z. (2012). Ultrasound as a basic and auxiliary process for dye remediation: a review. *Journal of Environmental Management*, *104*, 127–141.

Eskandarloo, H., Badiei, A., & Behnajady, M. A. (2014). Study of the Effect of Additives on the Photocatalytic Degradation of a Triphenylmethane Dye in the Presence of Immobilized TiO_2/NiO Nanoparticles: Artificial Neural Network Modeling. *Industrila and Engineering Chemistry Research*, *53,* 6881–6895.

Eskizeybek, V., Sarı, F., Gulce, H., Gulce, A., & Avcı, A. (2012). Preparation of the new polyaniline/ZnO nanocomposite and its photocatalytic activity for degradation of methylene blue and malachite green dyes under UV and natural sun lights irradiations. *Applied Catalysis B, Environmental*, *119–120*, 197–206.

Fan, T., Chen, C., & Tang, Z. (2016). Hydrothermal synthesis of novel $BiFeO_3/BiVO_4$ heterojunctions with enhanced photocatalytic activities under visible light irradiation. *RSC Advances*, *6*, 9994–10000.

Fan, T., Chen, C., Tang, Z., Ni, Y., & Lu, C. (2015). Synthesis and characterization of g-$C_3N_4/BiFeO_3$ composites with an enhanced visible light photocatalytic activity. *Materials Science in Semiconductor Processing*, *40*, 439–445.

Fatima, S., Ali, S. I., Iqbal, M. Z., & Rizwan, S. (2017). The high photocatalytic activity and reduced band gap energy of La and Mn co-doped $BiFeO_3$/graphene nanoplatelet (GNP) nanohybrids. *RSC Advances*, *7*, 35928–35937.

Fuwa, K., & Valle, B. L. (1963). The Physical Basis of Analytical Atomic Absorption Spectrometry. The Pertinence of the Beer-Lambert Law. *Analytical Chemistry*, *35*(8), 942–946.

Gao, M., Zhang, D., Pu, X., Ma, H., Su, C., Gao, X., & Dou, J. (2016). Surface decoration of BiOBr with $BiPO_4$ nanoparticles to build heterostructure photocatalysts with enhanced visible-light photocatalytic activity. *Separation and Purification Technology*, *170*, 183–189.

Gao, T., Chen, Z., Huang, Q., Niu, F., Huang, X., & Qin, L. (2015). A review: Preparation of bismuth ferrite nanoparticles and its applications in visible-light induced photocatalyses. *Reviews on Advanced Materials Science*, *40*, 97–109.

Gao, T., Chen, Z., Niu, F., Zhou, D., Huang, Q., Zhu, Y., Qin, L., Sun, X., & Huang, Y. (2015). Shape-controlled preparation of bismuth ferrite by hydrothermal method and their visible-light degradation properties. *Journal of Alloys and Compounds*. *648*, 564−570.

Gao, X., Tang, G., Peng, W., Guo, Q., & Luo, Y. (2019). Surprise in the phosphate modification of BiOCl with oxygen vacancy: In situ construction of hierarchical Z-scheme BiOCl-OV-$BiPO_4$ photocatalyst for the degradation of carbamazepine. *Chemical Engineering Journal*, *360*, 1320–1329.

Gao, Y., Lin, J., Zhang, Q., Yu, H., Ding, F., Xu, B., Sun, Y., & Xu, Z. (2017). Facile Synthesis of Heterostructured YVO_4/g-C_3N_4/Ag Photocatalysts with Enhanced Visible-Light Photocatalytic Performance. *Applied Catalysis B: Environmental*, *224*, 586–593.

Garg, A., Sangal, V. K., & Bajpai, P. K. (2015). Decolorization and degradation of Reactive Black 5 dye by photocatalysis: modeling , optimization and kinetic study. *Desalination and Water Treatment*, *3994*, 18003–18015.

Gaya, U. I. (2014). Kinetic Concepts of Heterogeneous Photocatalysis. *Heterogeneous Photocatalysis Using Inorganic Semiconductor Solids*, 43–71.

Gong, L., Zhou, Z., Wang, S., & Wang, B. (2013). Preparation and characterization of $BiFeO_3$@Ce-doped TiO_2 core-shell structured nanocomposites. *Materials Science in Semiconductor Processing, 16,* 288–294.

Gorska, P., Zaleska, A., & Hupka, J. (2009). Photodegradation of phenol by UV/TiO_2 and Vis/N, C-TiO_2 processes: Comparative mechanistic and kinetic studies. *Separation and Purification Technology, 68,* 90–96.

Gou, J., Li, X., Zhang, H., Guo, R., & Deng, X. (2018). Synthesis of silver/silver chloride/exfoliated graphite nano-photocatalyst and its enhanced visible light photocatalytic mechanism for degradation of organic pollutants. *Journal of Industrial and Engineering Chemistry, 59,* 99–107.

Gowrishankar, M., Babu, D. R., & Madeswaran, S. (2016). Effect of Gd–Ti co-substitution on structural, magnetic and electrical properties of multiferroic $BiFeO_3$. *Journal of Magnetism and Magnetic Materials, 418,* 54–61.

Gu, Y., Zhao, J., Zhang, W., Liu, S., Ge, S., Chen, W., & Zhang, Y. (2016). Improved ferromagnetism and ferroelectricity of La and Co co-doped $BiFeO_3$ ceramics with Fe vacancies. *Ceramics International, 42,* 8863–8868.

Guo, B., Deng, H., Zhai, X., Zhou, W., Meng, X., Weng, G., Chen, S., Yang, P., & Chu, J. (2017). Cr doping-induced structural phase transition, optical tuning and magnetic enhancement in $BiFeO_3$ thin films. *Materials Letters, 186,* 198–201.

Guo, N., Zeng, Y., Li, H., Xu, X., Yu, H., & Han, X. (2018). Novel mesoporous TiO_2@g-C_3N_4 hollow core@shell heterojunction with enhanced photocatalytic activity for water treatment and H_2 production under simulated sunlight. *Journal of Hazardous Materials*, *353*, 80–88.

Guo, R., Fang, L., Dong, W., Zheng, F., & Shen, M. (2010). Enhanced Photocatalytic Activity and Ferromagnetism in Gd Doped $BiFeO_3$ Nanoparticles. *The Journal of Physical Chemistry C*, *114*, 21390–21396.

Guo, Z., Ma, R., & Li, G. (2006). Degradation of phenol by nanomaterial TiO_2 in wastewater. *Chemical Engineering Journal*, *119*, 55–59.

Guy, N., & Ozacar, M. (2016). The influence of noble metals on photocatalytic activity of ZnO for Congo red degradation. *International Journal of Hydrogen Energy*, *41*, 20100-20112.

Guz, R., Moura, C. De, & Antônio, M. (2016). Factorial design application in photocatalytic wastewater degradation from TNT industry — red water. *Environmental Science and Pollution Research*, *24*, 6055–6060.

Habibi-yangjeh, A., Mousavi, M., & Nakata, K. (2019). Boosting visible-light photocatalytic performance of g-C_3N_4/Fe_3O_4 anchored with $CoMoO_4$ nanoparticles: Novel magnetically recoverable photocatalysts. *Journal of Photochemistry & Photobiology, A: Chemistry*, *368*, 120–136.

Han, Y., Ma, Y., Quan, C., Gao, N., Zhang, Q., Mao, W., Zhang, J., Yang, J., Li, X., & Huang, W. (2015). Substitution-driven structural, optical and magnetic transformation of Mn, Zn doped $BiFeO_3$. *Ceramics International*, *41*, 2476–2483.

Hao, C., Xiang, J., Hou, H., Lv, W., Lv, Y., & Hu, W. (2014). Photocatalytic performances of $BiFeO_3$ particles with the average size in nanometer, submicrometer, and micrometer. *Materials Research Bulletin*, *50*, 369–

373.

He, J., Guo, R., Fang, L., Dong, W., Zheng, F., & Shen, M. (2013). Characterization and visible light photocatalytic mechanism of size-controlled $BiFeO_3$ nanoparticles. *Materials Research Bulletin*, *48*, 3017–3024.

He, W., Wu, H., Wamer, W. G., Kim, H., Zheng, J., Jia, H., Zheng, Z., & Yin, J. (2014). Unraveling the Enhanced Photocatalytic Activity and Phototoxicity of ZnO/Metal Hybrid Nanostructures from Generation of Reactive Oxygen Species and Charge Carriers. *ACS Applied Materials & Interfaces*, *6*, 15527−15535.

Herrmann, J. (1999). Heterogeneous photocatalysis: fundamentals and applications to the removal of various types of aqueous pollutants, *Catalysis Today*, *53*, 115–129.

Hoong, K., Hui, C., Khan, M. R., & Kui, C. (2016). Photocatalytic degradation of recalcitrant POME waste by using silver doped titania: Photokinetics and scavenging studies, *Chemical Engineering Journal*, *286*, 282–290.

Hsieh, S. H., Chen, W. J., & Wu, C. T. (2015). Pt-TiO_2/Graphene photocatalysts for degradation of AO7 dye under visible light. *Applied Surface Science*, *340*, 9–17.

Huang, J., Tan, G., Yang, W., Zhang, L., Ren, H., & Xia, A. (2014). Microwave hydrothermal synthesis of $BiFeO_3$: Impact of different surfactants on the morphology and photocatalytic properties. *Materials Science in Semiconductor Processing*, *25*, 84–88.

Huang, M., Xu, C., Wu, Z., Huang, Y., Lin, J., & Wu, J. (2008). Photocatalytic discolorization of methyl orange solution by Pt modified TiO_2 loaded on natural zeolite. *Dyes and Pigments*, *77*, 327–334.

Hui, Pan, Lin, J., & Zhang, D. (2014). Graphene-based photocatalysts for oxygen evolution from water. *RSC Advances*, *5*, 6543–6552.

Humayun, M., Zada, A., Li, Z., Xie, M., Zhang, X., Qu, Y., Raziq, F., & Jing, L. (2016). Enhanced visible-light activities of porous $BiFeO_3$ by coupling with nanocrystalline TiO_2 and mechanism. *Applied Catalysis B: Environmental*, *180*, 219–226.

Huo, Y., Miao, M., Zhang, Y., Zhu, J., & Li, H. (2011). Aerosol-spraying preparation of a mesoporous hollow spherical $BiFeO_3$ visible photocatalyst with enhanced activity and durability. *Chemical Communications*, *47*, 2089–2091.

Hussain, I., Zhang, Y., Li, M., Huang, S., & Hayat, W. (2018). Heterogeneously degradation of aniline in aqueous solution using persulfate catalyzed by magnetic $BiFeO_3$ nanoparticles. *Catalysis Today*, *310*, 130–140.

Ilic, N. I., Bobic, J. D., Stojadinovic, B. S., Dzunuzovic, A. S., Vijatovic Petrovic, M. M., Dohcevic-Mitrovic, Z. D., & Stojanovic, B. D. (2016). Improving of the electrical and magnetic properties of $BiFeO_3$ by doping with yttrium. *Materials Research Bulletin*, *77*, 60–69.

Ilić, N. I., Džunuzović, A. S., Bobić, J. D., Stojadinović, B. S., Hammer, P., Vijatović Petrović, M. M., & Stojanović, B. D. (2015). Structure and properties of chemically synthesized $BiFeO_3$. Influence of fuel and complexing agent. *Ceramics International*, *41*, 69–77.

Jaffari, Z. H., Lam, S. M., Sin, J. C., & Mohamed, A. R. (2019). Constructing magnetic Pt-loaded $BiFeO_3$ nanocomposite for boosted visible light photocatalytic and antibacterial activities. *Environmental Science and Pollution Research*, *26*, 10204–10218.

Jaffari, Z. H., Lam, S., Sin, J., & Zeng, H. (2019). Boosting visible light photocatalytic and antibacterial performance by decoration of silver on magnetic spindle-like bismuth ferrite. *Materials Science in Semiconductor Processing*, *101*, 103–115.

Jain, A., Jayaraman, S., Singh, G., Srinivasanc, M.P., (2016). Single step peroxidase extraction and oxidation of highly concentrated ethanol and phenol aqueous solutions using supercritical carbon dioxide, *Journal of Supercritical Fluids 116,* 209–214.

Jallouli, N., Pastrana-martínez, L. M., Ribeiro, A. R., & Moreira, N. F. F. (2018). Heterogeneous photocatalytic degradation of ibuprofen in ultrapure water , municipal and pharmaceutical industry wastewaters using a TiO_2/ UV-LED system. *Chemical Engineering Journal*, *334*, 976–984.

Jassal, V., Shanker, U., Kaith, B. S., & Shankar, S. (2015). Green synthesis of potassium zinc hexacyanoferrate nanocubes and their potential application in photocatalytic degradation of organic dyes. *RSC Advances*, *5*, 26141–26149.

Jia, X., Cao, J., Lin, H., Zhang, M., Guo, X., & Chen, S. (2017). Transforming type-I to type-II heterostructure photocatalyst via energy band engineering: A case study of I-BiOCl/I-BiOBr. *Applied Catalysis B, Environmental, 204*, 505–514.

Jiang, Y., Chowdhury, S., & Balasubramanian, R. (2019). New insights into the role of nitrogen-bonding configurations in enhancing the photocatalytic activity of nitrogen-doped graphene aerogels. *Journal of Colloid And Interface Science*, *534,* 574–585.

Jin, L, Tang, X., Yang, B., Yang, J., Song, W., Dai, J., Zhu, X., & Sun, Y. (2016). $BiFeO_3$(00*l*)/$LaNiO_3$/Si thin film with enhanced polarization: an-all solution approach. RSC Advances, 6, 78629−78635.

Jorfi, S., Barzegar, G., Ahmadi, M., Darvishi, R., Soltani, C., Haghighifard, J., Takdastan, A., Saadi, R., & Abtahi, M. (2016). Enhanced coagulation-photocatalytic treatment of Acid red 73 dye and real textile wastewater using UVA/synthesized MgO nanoparticles. *Journal of Environmental Management*, *177*, 111–118.

Joseph, A. I. J., & Thiripuranthagan, S. (2015). Metal doped titanate photo catalysts for the mineralization of congo red under visible irradiation. *RSC Advances*, *5*, 9792–9805.

Kadi, M. W., McKinney, D., Mohamed, R. M., Mkhalid, I. A., & Sigmund, W. (2016). Fluorine doped zinc oxide nanowires: enhanced photocatalysts degrade malachite green dye under visible light conditions. *Ceramics International*, *42*, 4672–4678.

Kalinin, S. V, Suchomel, M. R., Davies, P. K., & Bonnell, D. A. (2002). Potential and Impedance Imaging of Polycrystalline $BiFeO_3$ Ceramics. *Journal of the American Ceramic Society*, *85*, 3011–3017.

Kalra, S. S., Mohan, S., Sinha, A., & Singh, G. (2011). Advanced oxidation processes for treatment of textile and dye wastewater: a review. In *2nd*

International conference on environmental science and development, *4*, 271–275.

Kamali, M., & Khodaparast, Z. (2015). Review on recent developments on pulp and paper mill wastewater treatment. *Ecotoxicology and Environmental Safety*, *114*, 326–342.

Kamranifar, M., Allahresani, A., & Naghizadeh, A. (2019). Synthesis and characterizations of a novel $CoFe_2O_4$@CuS magnetic nanocomposite and investigation of its efficiency for photocatalytic degradation of penicillin G antibiotic in simulated wastewater. *Journal of Hazardous Materials*, *366*(June 2018), 545–555.

Kango, S., Kalia, S., Celli, A., Njuguna, J., Habibi, Y., & Kumar, R. (2013). Surface modification of inorganic nanoparticles for development of organic – inorganic nanocomposites — A review. *Progress in Polymer Science*, *38*, 1232–1261.

Kaur, H., Navjot, Tovstolytkin, A., & Lotey, G. S. (2017). Coinage metal (Ag, Cu) decorated-synthesis, characterization and their photocatalysis properties. *Journal of Materials Science: Materials in Electronics*, *28*, 18236–18243.

Kaur, J., Gupta, K., Kumar, V., Bansal, S., & Singhal, S. (2016). Synergic effect of Ag decoration onto ZnO nanoparticles for the remediation of synthetic dye wastewater. *Ceramics International*, *42*, 2378–2385.

Kaur, M., Mehta, S. K., & Kumar, S. (2018). Visible light driven photocatalytic degradation of ofloxacin and malachite green dye using cadmium sulphide nanoparticles. *Journal of Environmental Chemical Engineering*, *6*, 3631–

3639.

Kim, H., Yoo, H., Hong, S., Lee, S., Lee, S., Park, B.S, Park, H., Lee, C., & Lee, J. (2015). Effects of inorganic oxidants on kinetics and mechanisms of WO3-mediated photocatalytic degradation. *Applied Catalysis B, Environmental*, *162*, 515–523.

Klubnuan, S., Suwanboon, S., & Amornpitoksuk, P. (2016). Effects of optical band gap energy , band tail energy and particle shape on photocatalytic activities of different ZnO nanostructures prepared by a hydrothermal method. *Optical Materials*, *53*, 134–141.

Koltsakidou, A., Antonopoulou, M., Evgenidou, E., Konstantinou, I., & Lambropoulou, D. A. (2017). Cytarabine degradation by simulated solar assisted photocatalysis using TiO_2. *Chemical Engineering Journal*, *316*, 823–831.

Koltsakidou, A., Antonopoulou, M., Evgenidou, E., Konstantinou, I., & Lambropoulou, D. A. (2017). Cytarabine degradation by simulated solar assisted photocatalysis using. *Chemical Engineering Journal*, *316*, 823–831.

Kong, J., Rui, Z., Wang, X., Ji, H., & Tong, Y. (2016). Visible-light decomposition of gaseous toluene over $BiFeO_3/(Bi/Fe)_2O_3$ heterojunctions with enhanced performance. *Chemical Engineering Journal*, *302*, 552–559.

Kong, L., Jiang, Z., Lai, H. H., Xiao, T., & Edwards, P. P. (2013). Does noble metal modification improve the photocatalytic activity of BiOCl? *Progress in Natural Science: Materials International*, *23*, 286–293.

Kuang, D., Tang, P., Wu, X., Yang, S., & Ding, X. (2016). Structural , optical and magnetic studies of (Y , Co) co-substituted $BiFeO_3$ thin films, *671*, 192–199.

Kumar, A., Khan, M., Zeng, X., & Lo, I. M. C. (2018). Development of g-$C_3N_4/TiO_2/Fe_3O_4@SiO_2$ heterojunction via sol-gel route: A magnetically recyclable direct contact Z-scheme nanophotocatalyst for enhanced photocatalytic removal of ibuprofen from real sewage effluent under visible light. *Chemical Engineering Journal*, *353*, 645–656.

Kumar, K. V., Porkodi, K., & Rocha, F. (2008). Langmuir – Hinshelwood kinetics – A theoretical study. *Catalysis Communications, 9*, 82–84.

Kumar, P., & Kar, M. (2014). Effect of structural transition on magnetic and optical properties of Ca and Ti co-substituted $BiFeO_3$ ceramics. *Journal of Alloys and Compounds, 584*, 566–572.

Kumar, S., Surendar, T., Baruah, A., & Shanker, V. (2013). Synthesis of novel and stable g-C_3N_4/Ag_3PO_4 hybrid nanocomposite photocatalyst and studied the photocatalytic activity under visible light irradiation. *Materials Chemistry A, 1,* 5333–5340.

Kumar, V., & Singh, S. (2016). Improved structure stability, optical and magnetic properties of Ca and Ti co-substituted $BiFeO_3$ nanoparticles. *Applied Surface Science, 386,* 78–83.

L. Khezami, Taha, K. K. ., Ghiloufi, I., & Mir, L. El. (2016). Adsorption and photocatalytic degradation of malachite green by vanadium doped zinc oxide nanoparticles. *Water Science and Technology, 73,* 881–889.

Lam, S.-M., Jaffari, Z. H., & Sin, J.-C. (2018). Hydrothermal synthesis of coral-like palladium-doped $BiFeO_3$ nanocomposites with enhanced photocatalytic and magnetic properties. *Materials Letters*, *224*, 1–4.

Lam, S. M., Low, X. Z. D., Wong, K. A., & Sin, J. C. (2018). Sequencing coagulation–photodegradation treatment of Malachite Green dye and textile wastewater through ZnO micro/nanoflowers. *Chemical Engineering Communications*, *205*, 1143–1156.

Lam, S.M., Quek, J.A., & Sin, J. (2018). Mechanistic investigation of visible light responsive Ag/ZnO micro/nanoflowers for enhanced photocatalytic performance and antibacterial activity. *Journal of Photochemistry & Photobiology, A: Chemistry*, *353*, 171–184.

Lam, S.M., Sin, J.C., & Mohamed, A. R. (2010). Parameter effect on photocatalytic degradation of phenol using TiO_2-P25/activated carbon (AC), *Koreon Journal of Chemical Engineering*, *27*, 1109–1116.

Lam, S.M., Sin, J.C., & Mohamed, A. R. (2017). Short Review A newly emerging visible light-responsive $BiFeO_3$ perovskite for photocatalytic applications: A mini review. *Materials Research Bulletin*, *90*, 15–30.

Lamo, M. B., Buering, M., & Bahnemann, D. (2015). Effect of flowrate, photocatalyst loading and illumination conditions on the photocatalytic disinfection of recombinant *Escherichia coli*. *Journal of Material Research Inovation*, *19*, 20–23.

Lang, X., Chen, X., & Zhao, J. (2014). Heterogeneous visible light photocatalysis for selective organic transformations. *Chemical Society Reviews*, *43*, 473–486.

Li-xiang, Z., An-chao, Z., Qi-feng, Z. H. U., Hua, W., & Chun-jing, Z. (2018). Effects of experimental parameters on Hg^0 removal over magnetic AgI-BiOI/$CoFe_2O_4$ photocatalysts using wet process. *Journal of Fuel Chemistry and Technology*, *46*, 365–374.

Li, D., Zhu, Q., Han, C., Yang, Y., Jiang, W., & Zhang, Z. (2015). Photocatalytic degradation of recalcitrant organic pollutants in water using a novel cylindrical multi-column photoreactor packed with TiO_2-coated silica gel beads. *Journal of Hazardous Materials, 285,* 398–408.

Li, P., Chen, Q., Lin, Y., Chang, G., & He, Y. (2016). Effects of crystallite structure and interface band alignment on the photocatalytic property of bismuth ferrite/(N-doped) graphene composites. *Journal of Alloys and Compounds*, *672*, 497–504.

Li, Shun, Lin, Y., Zhang, B., Wang, Y., & Nan, C. (2010). Controlled Fabrication of $BiFeO_3$ Uniform Microcrystals and Their Magnetic and Photocatalytic Behaviors. *The Journal Physical Chemistry C, 7*, 2903–2908.

Li, Shun, Zhang, J., Kibria, M. G., Mi, Z., Chaker, M., Ma, D., Rosei, F. (2013). Remarkably enhanced photocatalytic activity of laser ablated Au nanoparticle decorated $BiFeO_3$ nanowires under visible-light. *Chemical Communications (Cambridge, England)*, *49*, 5856–5858.

Li, Si, & Hu, J. (2016). Photolytic and photocatalytic degradation of tetracycline: Effect of humic acid on degradation kinetics and mechanisms. *Journal of Hazardous Materials*, *318*, 134–144.

Li, Xiaolong, Zhang, F., Ma, C., Deng, Y., Wang, Z., Elingarami, S., & He, N.

(2012). Controllable Synthesis of ZnO with Various Morphologies by Hydrothermal Method. *Journal of Nanoscience and Nanotechnology*, *12*, 2028–2036.

Li, Xiaoxuan, Fang, S., Ge, L., Han, C., Qiu, P., & Liu, W. (2015). Synthesis of flower-like Ag/AgCl-Bi_2MoO_6 plasmonic photocatalysts with enhanced visible-light photocatalytic performance. *Applied Catalysis B: Environmental*, *176–177*, 62–69.

Li, Z., Wang, J., Zhu, K., Ma, F., & Meng, A. (2015). Ag/g-C_3N_4 composite nanosheets: Synthesis and enhanced visible photocatalytic activities. *Materials Letters*, *145*, 167–170.

Lin, C., & Lin, K. (2007). Photocatalytic oxidation of toxic organohalides with TiO_2/UV: The effects of humic substances and organic mixtures. *Chemosphere*, *66*, 1872–1877.

Lin, Q., Li, L., Liang, S., Liu, M., Bi, J., & Wu, L. (2015). Efficient synthesis of monolayer carbon nitride 2D nanosheet with tunable concentration and enhanced visible-light photocatalytic activities. *Applied Catalysis B: Environmental*, *163*, 135–142.

Linsebigler, A. L., Lu, G., & Yates, J. T. (1995). Photocatalysis on TiO_2 Surfaces: Principles, Mechanisms, and Selected Results, *Chemical Reviews*, *95*, 735–758.

Liu, B., Mu, L., Han, B., Zhang, J., & Shi, H. (2017). Fabrication of TiO_2/Ag_2O heterostructure with enhanced photocatalytic and antibacterial activities under visible light irradiation. *Applied Surface Science*, *396*, 1596–1603.

Liu, W., Zhao, X., Wang, T., Zhao, D., & Ni, J. (2016). Adsorption of U (VI) by multilayer titanate nanotubes: Effects of inorganic cations , carbonate and natural organic matter. *Chemical Engineering Journal*, *286*, 427–435.

Liu, X.-M., Fu, S.-Y., & Huang, C.-J. (2005). Synthesis and magnetic characterization of novel $CoFe_2O_4$–$BiFeO_3$ nanocomposites. *Materials Science and Engineering: B*, *121*, 255–260.

Liu, X., & Cai, L. (2018). Novel indirect Z-scheme photocatalyst of Ag nanoparticles and polymer polypyrrole co-modified BiOBr for photocatalytic decomposition of organic pollutants. *Applied Surface Science*, *445*, 242–254.

Liu, Yanfang, Zhu, Y., Xu, J., Bai, X., Zong, R., & Zhu, Y. (2013). Degradation and mineralization mechanism of phenol by $BiPO_4$ photocatalysis assisted with H_2O_2. *Applied Catalysis B, Environmental*, *142–143*, 561–567.

Liu, Yi, Zuo, R., & Qi, S. (2013). Controllable preparation of $BiFeO_3$@carbon core/shell nanofibers with enhanced visible photocatalytic activity. *Journal of Molecular Catalysis A: Chemical*, *376*, 1–6.

Liu, Z., Qi, Y., & Lu, C. (2010). High efficient ultraviolet photocatalytic activity of $BiFeO_3$ nanoparticles synthesized by a chemical coprecipitation process. *Journal of Material Science: Material Electronics*, *21*, 380–384.

Lotey, G. S., & Verma, N. K. (2014). Synthesis and characterization of $BiFeO_3$ nanowires and their applications in dye-sensitized solar cells. *Materials Science in Semiconductor Processing*, *21*, 206–211.

Lou, X., Xiao, D., Fang, C., Wang, Z., Liu, J., Guo, Y., & Lu, S. (2015).

Comparison of UV/hydrogen peroxide and UV/peroxydisulfate processes for the degradation of humic acid in the presence of halide ions. *Environmental Science and Pollution Research*, *23*, 4778–4785.

Lourdes, M. De, Peralta, R., Sánchez-cantú, M., Puente-lópez, E., Rubio-rosas, E., & Tzompantzi, F. (2017). Evaluation of calcium oxide in Rhodamine 6G photodegradation. *Catalysis Today*, 305, 75–81.

Lu, L., Lv, M., Liu, G., & Xu, X. (2017). Photocatalytic hydrogen production over solid solutions between $BiFeO_3$ and $SrTiO_3$. *Applied Surface Science*, *391*, 535–541.

Luo, L., Shen, K., Xu, Q., Zhou, Q., Wei, W., & Gondal, M. A. (2013). Preparation of multiferroic Co substituted $BiFeO_3$ with enhanced coercive force and its application in sorption removal of dye molecules from aqueous solution. *Journal of Alloys and Compounds*, *558*, 73–76.

Lv, T., Pan, L., Liu, X., & Sun, Z. (2012). Visible-light photocatalytic degradation of methyl orange by CdS–TiO_2–Au composites synthesized via microwave-assisted reaction. *Electrochimica Acta*, *83*, 216–220.

Ma, S., Meng, J., Li, J., Zhang, Y., & Ni, L. (2014). Synthesis of catalytic polypropylene membranes enabling visible-light-driven photocatalytic degradation of dyes in water. *Journal of Membrane Science*, *453*, 221–229.

Mahmoodi, N. M. (2017). Photocatalytic degradation of textile dyes using ozonation and magnetic nickel ferrite nanoparticle. *Progress in Colour Colorant and Coatings*, *9*, 163–171.

Malato, S., Fernández-Ibáñez, P., Maldonado, M. I., Blanco, J., & Gernjak, W.

(2009). Decontamination and disinfection of water by solar photocatalysis: recent overview and trends. *Catalysis Today*, *147*, 1–59.

Maria Magdalane, C., Kaviyarasu, K., Judith Vijaya, J., Siddhardha, B., & Jeyaraj, B. (2017). Facile synthesis of heterostructured cerium oxide/yttrium oxide nanocomposite in UV light induced photocatalytic degradation and catalytic reduction: Synergistic effect of antimicrobial studies. *Journal of Photochemistry and Photobiology B: Biology*, *173*, 23–34.

Mathubala, G., Manikandan, A., Antony, S. A., & Ramar, P. (2016). Photocatalytic degradation of methylene blue dye and magneto- optical studies of magnetically recyclable spinel Ni_x $Mn_{1-x}Fe_2O_4$ (x = 0.0-1.0) nanoparticles. *Journal of Molecular Structure*, *1113*, 79–87.

Mehrjouei, M., Müller, S., & Möller, D. (2015). A review on photocatalytic ozonation used for the treatment of water and wastewater. *Chemical Engineering Journal*, *263*, 209–219.

Meng, W., Hu, R., Yang, J., Du, Y., Li, J., & Wang, H. (2016). Influence of lanthanum-doping on photocatalytic properties of $BiFeO_3$ for phenol degradation. *Chinese Journal of Catalysis*, *37*, 1283–1292.

Meng, X., & Zhang, Z. (2017). Pd-doped Bi_2MoO_6 plasmonic photocatalysts with enhanced visible light photocatalytic performance. *Applied Surface Science*, *392*, 169–180.

Michael, R. J. V., Sambandam, B., Muthukumar, T., Umapathy, M. J., & Manoharan, P. T. (2014). Spectroscopic dimensions of silver nanoparticles and clusters in ZnO matrix and their role in bioinspired antifouling and photocatalysis. *Phys. Chem. Chem. Phys*, *16*, 8541–8555.

Miranda-García, N., Suárez, S., Sánchez, B., Coronado, J. M., Malato, S., & Maldonado, M. I. (2011). Photocatalytic degradation of emerging contaminants in municipal wastewater treatment plant effluents using immobilized TiO_2 in a solar pilot plant. *Applied Catalysis B: Environmental*, *103*, 294–301.

Mirmasoomi, S. R., Ghazi, M. M., & Galedari, M. (2017). Photocatalytic degradation of diazinon under visible light using TiO_2/Fe_2O_3 nanocomposite synthesized by ultrasonic-assisted impregnation method. *Separation and Purification Technology*, *175*, 418–427.

Mohamed, R. M., McKinney, D., Kadi, M. W., Mkhalid, I. A., & Sigmund, W. (2016). Platinum/zinc oxide nanoparticles: enhanced photocatalysts degrade malachite green dye under visible light conditions. *Ceramics International*, *42*, 9375–9381.

Mohammad, A., Nazif, S., Taebi, A., & Shahghasemi, E. (2017). Treatment of phenol in petrochemical wastewater considering turbidity factor by backlight cascade photocatalytic reactor. *Journal of Photochemistry & Photobiology, A: Chemistry*, *348*, 161–167.

Monlau, F., Sambusiti, C., Barakat, A., Quéméneur, M., Trably, E., Steyer, J., & Carrère, H. (2014). Do furanic and phenolic compounds of lignocellulosic and algae biomass hydrolyzate inhibit anaerobic mixed cultures? A comprehensive review. *Biotechnology Advances*, *32*, 934–951.

Mosleh, S., Rahimi, M. R., Ghaedi, M., Dashtian, K., & Hajati, S. (2016). Photocatalytic degradation of binary mixture of toxic dyes by HKUST-1

MOF and HKUST-1-SBA-15 in a rotating packed bed reactor under blue LED illumination: central composite design. *RSC Advances*, *6*, 17204–17214.

Motahari, F., Mozdianfard, M. R., Soofivand, F., & Salavati-Niasari, M. (2014). NiO nanostructures: synthesis, characterization and photocatalyst application in dye wastewater treatment. *RSC Advances*, *4*, 27654−27663.

Murgolo, S., Yargeau, V., Gerbasi, R., Visentin, F., Habra, N. El, Ricco, G., Lacchetti, I., Carere, M., Curri, M.L., & Mascolo, G. (2017). A new supported TiO_2 film deposited on stainless steel for the photocatalytic degradation of contaminants of emerging concern. *Chemical Engineering Journal*, *318*, 103–111.

Muruganandham, M., Suri, R. P. S., Jafari, S., Sillanpaa, M., Lee, G.-J., Wu, J. J., & Swaminathan, M. (2014). Recent Developments in Homogeneous Advanced Oxidation Processes for Water and Wastewater Treatment. *International Journal of Photoenergy*, *2014*, 1−21.

Nanakkal, A. R., & Alexander, L. K. (2017). Graphene/$BiVO_4$/TiO_2 nanocomposite: tuning band gap energies for superior photocatalytic activity under visible light. *Journal of Materials Science*. *52*, 7997−8006.

Navjot, Tovstolytkin, A., & Lotey, G. S. (2017). Plasmonic Enhanced Photocatalytic Activity of Ag Nanospheres Decorated-$BiFeO_3$ Nanoparticles. *Catalysis Letters*, *147*, 1640–1645.

Ng, K. H., Cheng, Y. W., Khan, M. R., & Cheng, C. K. (2016). Optimization of photocatalytic degradation of palm oil mill effluent in UV/ZnO system based on response surface methodology. *Journal of Environmental*

Management, *184*, 487–493.

Ni, Z., Dong, F., Huang, H., & Zhang, Y. (2016). New insights into how Pd nanoparticles influence the photocatalytic oxidation and reduction ability of g-C_3N_4 nanosheets. *Catalysis Science & Technology*, *6*, 6448–6458.

Nischk, M., Mazierski, P., Gazda, M., & Zaleska, A. (2014). Ordered TiO_2 nanotubes: The effect of preparation parameters on the photocatalytic activity in air purification process. *Applied Catalysis B, Environmental*, *144*, 674–685.

Niu, F., Chen, D., Qin, L., Gao, T., Zhang, N., Wang, S., & Huang, Y. (2015). Synthesis of Pt/$BiFeO_3$ heterostructured photocatalysts for highly efficient visible-light photocatalytic performances. *Solar Energy Materials and Solar Cells*, *143*, 386–396.

Niu, F., Chen, D., Qin, L., Zhang, N., Wang, J., Chen, Z., & Huang, Y. (2015). Facile Synthesis of Highly Efficient p--n Heterojunction CuO/$BiFeO_3$ Composite Photocatalysts with Enhanced Visible-Light Photocatalytic Activity. *ChemCatChem*, *7*, 3279–3289.

Ohtani, B. (2010). Photocatalysis A to Z-What we know and what we do not know in a scientific sense. *Journal of Photochemistry and Photobiology C: Photochemistry Reviews*, *11*, 157–178.

Oller, I., Malato, S., & Sánchez-Pérez, J. A. (2011). Combination of Advanced Oxidation Processes and biological treatments for wastewater decontamination-A review. *Science of the Total Environment*, *409*, 4141–4166.

Kumar, G.S., & Rao, K.S.R.K. (2014). Zinc oxide based photocatalysis: tailoring surface-bulk structure and related interfacial charge carrier dynamics for better environmental application. *RSC Advances.* 5, 3306−3351.

Oskoei, V., Dehghani, M. H., Nazmara, S., Heibati, B., Asif, M., & Tyagi, I. (2016). Removal of humic acid from aqueous solution using UV/ZnO nano-photocatalysis and adsorption. *Journal of Molecular Liquids*, *213*, 374–380.

Oturan, M. A., & Aaron, J.-J. (2014). Advanced Oxidation Processes in Water/Wastewater Treatment: Principles and Applications. A Review. *Critical Reviews in Environmental Science and Technology*, *44*, 2577–2641.

Palacio, M., Rossi, L., Estefanía, M., Hermosilla, F., Rosso, J. A., Villabrille, P. I., & Martin, M. V. (2017). Selective photodegradation of phenol in the presence of a commercial humic acid. *Journal of Environmental Chemical Engineering*, *5,* 5540–5546.

Palai, R., Katiyar, R. S., Schmid, H., Tissot, P., Clark, S. J., Robertson, J., Redfern, S.A.T., Catalan, G., & Scott, J. F. (2008). β phase and $\gamma-\beta$ metal-insulator transition in multiferroic $BiFeO_3$. *Physical Review B, 77*, 14110–14121.

Pang, K., Zhang, Q., & Xu, Y. (2019). Hierarchical magnetic $BiFeO_3$ microcages: Controlling synthesis and visible-light photocatalytic activity. *Ceramics International*, *45*, 1554–1561.

Pathania, D., Katwal, R., Sharma, G., & Naushad, M. (2016). Novel guar gum/Al_2O_3 nanocomposite as an effective photocatalyst for the degradation of malachite green dye. *International Journal of Biological Macromolecules*, *87*, 366–374.

Patil, S. S., Tamboli, M. S., Patil, D. R., Kulkarni, M. V, Yoon, H., Kim, H., & Kale, B. B. (2016). Green approach for hierarchical nanostructured Ag-ZnO and their photocatalytic performance under sunlight. *Catalysis Today*, *260*, 126–134.

Pei, Y. L., & Zhang, C. (2013). Effect of ion doping in different sites on the morphology and photocatalytic activity of $BiFeO_3$ microcrystals. *Journal of Alloys and Compounds*, *570*, 57–60.

Pirok, B. W. J., Knip, J., Bommel, M. R. Van, & Schoenmakers, P. J. (2016). Characterization of Synthetic Dyes by Comprehensive Two-dimensional Liquid Chromatography combining Ion-exchange Chromatography and Fast Ion-Pair Reversed-Phase Chromatography. *Journal of Chromatography A*, *1436*, 141–146.

Ponraj, C., Vinitha, G., & Daniel, J. (2017). A review on the visible light active $BiFeO_3$ nanostructures as suitable photocatalyst in the degradation of different textile dyes. *Environmental Nanotechnology, Monitoring & Management*, *7*, 110–120.

Priac, A., Morin-Crini, N., Druart, C., Gavoille, S., Bradu, C., Lagarrigue, C., Torri, G., Winterton, P., & Crini, G. (2017). Alkylphenol and alkylphenol polyethoxylates in water and wastewater: A review of options for their elimination. *Arabian Journal of Chemistry*, *10*, S3749–S3773.

Prieto-Rodríguez, L., Oller, I., Klamerth, N., Agüera, A., Rodríguez, E. M., &

Malato, S. (2013). Application of solar AOPs and ozonation for elimination of micropollutants in municipal wastewater treatment plant effluents. *Water Research*, *47*, 1521–1528.

Prince, J., Tzompantzi, F., Mendoza-Damián, G., Hernández-Beltrán, F., & Valente, J. S. (2015). Photocatalytic degradation of phenol by semiconducting mixed oxides derived from Zn (Ga) Al layered double hydroxides. *Applied Catalysis B: Environmental*, *163*, 352–360.

Qu, X., Alvarez, P. J. J., & Li, Q. (2013). Applications of nanotechnology in water and wastewater treatment. *Water Research*, *47*, 3931–3946.

Quek, J.A., Lam, S.M., Sin, J.C., & Mohamed, A. R. (2018). Visible light responsive flower-like ZnO in photocatalytic antibacterial mechanism towards *Enterococcus faecalis* and *Micrococcus luteus*. *Journal of Photochemistry & Photobiology, B: Biology*, *187*, 66–75.

Rahman, A. F. A., Jalil, A. A., Triwahyono, S., Ripin, A., Aziz, F. F. A., Fatah, N. A. A., & Hassan, N. S. (2017). Strategies for introducing titania onto mesostructured silica nanoparticles targeting enhanced photocatalytic activity of visible-light-responsive Ti-MSN catalysts. *Journal of Cleaner Production*, *143*, 948–959.

Rahmatolahzadeh, R., Ebadi, M., & Motevalli, K. (2017). Preparation and characterization of Cu clusters and Cu–Ag alloy via galvanic replacement method for azo dyes degradation. *Journal of Materials Science: Materials in Electronics*, *28*, 6056–6063.

Ramezanalizadeh, H., & Manteghi, F. (2017). Immobilization of mixed cobalt/nickel metal-organic framework on a magnetic $BiFeO_3$: A highly efficient separable photocatalyst for degradation of water pollutions. *Journal of Photochemistry & Photobiology, A: Chemistry, 346*, 89–104.

Rauf, M. A., & Ashraf, S. S. (2009). Fundamental principles and application of heterogeneous photocatalytic degradation of dyes in solution. *Chemical Engineering Journal, 151*, 10–18.

Repousi, V., Petala, A., Frontistis, Z., Antonopoulou, M., Konstantinou, I., Kondarides, D. I., & Mantzavinos, D. (2017). Photocatalytic degradation of bisphenol A over Rh/TiO_2 suspensions in different water matrices. *Catalysis Today, 284,* 59–66.

Reza, K. M., Kurny, A., & Gulshan, F. (2015). Parameters affecting the photocatalytic degradation of dyes using TiO_2: a review. *Applied Water Science, 7,* 1569–1578.

Rezaei, A., Nabiyouni, G., & Ghanbari, D. (2016). Photo-catalyst and magnetic investigation of $BaFe_{12}O_{19}$–ZnO nanoparticles and nanocomposites. *Journal of Materials Science: Materials in Electronics. 27*, 11339−11352.

Ribao, P., Rivero, M. J., & Ortiz, I. (2016). TiO_2 structures doped with noble metals and/or graphene oxide to improve the photocatalytic degradation of dichloroacetic acid. *Environmental Science and Pollution Research. 24,* 12628−12637.

Rioja, N., Zorita, S., & Pe, F. J. (2016). Effect of water matrix on photocatalytic degradation and general kinetic modeling. *Applied Catalysis B: Environmental, 180,* 330–335.

Rizzo, L., Manaia, C., Merlin, C., Schwartz, T., Dagot, C., Ploy, M. C., & Fatta-

Kassinos, D. (2013). Urban wastewater treatment plants as hotspots for antibiotic resistant bacteria and genes spread into the environment: A review. *Science of the Total Environment*, *447*, 345–360.

Rasalingam, S., Kibombo, H.S., Wu, C.M., Peng, R., Baltrusaitis, J., Koodali, Rasalingam, S., Kibombo, H.S., Wu, C.M., Peng, R., Baltrusaitis, J., Koodali, R.T., (2014). Competitive role of structural properties of titania–silica mixed oxides and a mechanistic study of the photocatalytic degradation of phenol, *Applied Catalysis B: Environment, 148–149, 394–405.*

Saikia, L., Bhuyan, D., Saikia, M., Malakar, B., Dutta, D. K., & Sengupta, P. (2015). Photocatalytic performance of ZnO nanomaterials for self sensitized degradation of Malachite Green dye under solar light. *Applied Catalysis A, General*, *490*, 42–49.

Saputra, E., Muhammad, S., Sun, H.Q., An, H.M., Tadé, M.O., Wang, S.B., (2013). Different crystallographic one-dimensional MnO_2 nanomaterials and their superior performance in catalytic phenol degradation, Environmental Science and Technology, 47, 5882–5887.

Sakar, M., Balakumar, S., Saravanan, P., & Jaisankar, S. N. (2016). Electric field induced formation of one-dimensional bismuth ferrite ($BiFeO_3$) nanostructures in electrospinning process. *Materials & Design, 94,* 487−495.

Salehi, K., Bahmani, A., Shahmoradi, B., Pordel, M. A., Kohzadi, S., Gong, Y., Lee, S. (2017). Response surface methodology (RSM) optimization approach for degradation of Direct Blue 71 dye using CuO–ZnO nanocomposite. *International Journal of Environmental Science and Technology, 14,* 2067–2076.

Sampaio, M. J., Silva, C. G., Silva, A. M. T., & Faria, J. L. (2014). Kinetic modelling for the photocatalytic degradation of phenol by using TiO_2-coated glass raschig rings under simulated solar light. *Journal of Chemical Technology and Biotechnology*, *91*, 346–352.

Santiago, D. E., Ara, J., Do, J. M., Acosta-dacal, A. C., & Pérez-pe, J. (2014). Effect of inorganic ions on the photocatalytic treatment of agro-industrial wastewaters containing imazalil. *Applied Catalysis B: Environmental*, *157*, 284–292.

Saravanakumar, K., Karthik, R., Chen, S., Kumar, J. V., Prakash, K., & Muthuraj, V. (2017). Construction of novel $Pd/CeO_2/g\text{-}C_3N_4$ nanocomposites as efficient visible-light photocatalysts for hexavalent chromium detoxification. *Journal of Colloid And Interface Science, 504*, 514–526.

Saravanakumar, K., & Muthuraj, V. (2017). Fabrication of sphere like plasmonic Ag/SnO_2 photocatalyst for the degradation of phenol. *Optik - International Journal for Light and Electron Optics*, *131*, 754–763.

Saravanakumar, K., Ramjan, M. M., Suresh, P., & Muthuraj, V. (2016). Fabrication of highly efficient visible light driven Ag/CeO_2 photocatalyst for degradation of organic pollutants. *Journal of Alloys and Compounds, 664*, 149–160.

Sassaroli, A., & Fantini, S. (2004). Comment on the modified Beer-Lambert law for scattering media. *Physics in Medicine and Biology, 49*, N255.

Sati, P. C., Arora, M., Chauhan, S., Kumar, M., & Chhoker, S. (2014). Structural, magnetic, vibrational and impedance properties of Pr and Ti codoped $BiFeO_3$ multiferroic ceramics. *Ceramics International*, *40*, 7805–7816.

Schwartz, R. W. (1997). Chemical Solution Deposition of Perovskite Thin Films. *Chemistry of Materials*, *9*, 2325–2340.

Seifvand, N., Kowsari, E., (2016). Synthesis of mesoporous Pd-doped TiO_2 templated by a magnetic recyclable ionic liquid for efficient photocatalytic air treatment, *Industrial Engineering and Chemical Research*, *55*, 10533–10543.

Shahini, P., & Ashkarran, A. A. (2018). Immobilization of plasmonic Ag-Au NPs on the TiO_2 nanofibers as an efficient visible-light photocatalyst. *Colloids and Surfaces A: Physicochemical and Engineering Aspects*, *537*, 155–162.

Sharma, G., ALOthman, Z. A., Kumar, A., Sharma, S., Ponnusamy, S. K., & Naushad, M. (2017). Fabrication and characterization of a nanocomposite hydrogel for combined photocatalytic degradation of a mixture of malachite green and fast green dye. *Nanotechnology for Environmental Engineering*, *2*, 4.

Shet, A., & Shetty K, V. (2016). Solar light mediated photocatalytic degradation of phenol using Ag core –TiO_2 shell (Ag@TiO_2) nanoparticles in batch and fluidized bed reactor. *Solar Energy*, *127*, 67–78.

Sin, J.C., Lam, S.M., Satoshi, I., Lee, K., & Mohamed, A.R. (2014). Sunlight photocatalytic activity enhancement and mechanism of novel europiumdoped ZnO hierarchical micro/nanospheres for degradation of phenol. *Applied Catalysis B, Environmental*, *148–149*, 258–268.

Singh, H., & Yadav, K. L. (2014). Synthesis and study of structural, dielectric, magnetic and magnetoelectric characterization of $BiFeO_3$-$NiFe_2O_4$ nanocomposites prepared by chemical solution method. *Journal of Alloys and Compounds*, *585*, 805–810.

Singh, J., Kumari, P., & Basu, S. (2019). Degradation of toxic industrial dyes using SnO_2/g-C_3N_4 nanocomposites: Role of mass ratio on photocatalytic activity. *Journal of Photochemistry & Photobiology, A: Chemistry*, *371*, 136–143.

Singh, N., Rana, M. S., & Gupta, R. K. (2018). Modelling studies for photocatalytic degradation of organic dyes using TiO_2 nanofibers. *Environmental Science and Pollution Research*, *25*, 20466–20472.

Singhal, N., & Kumar, U. (2017). Noble metal modified TiO_2: selective photoreduction of CO_2 to hydrocarbons. *Molecular Catalysis*, *439*, 91–99.

Sobana, N., Subash, B., & Swaminathan, M. (2015). Effect of operational parameters on photodegradation of Direct Blue 53 by silver loaded-titania under ultraviolet and solar illumination. *Materials Science in Semiconductor Processing*, *36*, 149–155.

Sobczynski, A., Duczmal, L., & Zmudziski, W. (2004). Phenol destruction by photocatalysis on TiO2: an attempt to solve the reaction mechanism. *Journal of Molecular Catalysis A: Chemical*, *213*, 225–230.

Soltani, T, & Entezari, M. H. (2013). Ultraso nics Sonoch emistry Solar photocatalytic degradation of RB5 by ferrite bismuth nanoparticles synthesized via ultrasound. *Ultrasonics-Sonochemistry*, *20*, 1245–1253.

Soltani, Tayyebe, & Entezari, M. H. (2013). Sono-synthesis of bismuth ferrite nanoparticles with high photocatalytic activity in degradation of Rhodamine B under solar light irradiation. *Chemical Engineering Journal*, *223*, 145–154.

Soltani, Tayyebe, & Entezari, M. H. (2014). Solar-Fenton catalytic degradation of phenolic compounds by impure bismuth ferrite nanoparticles synthesized via ultrasound. *Chemical Engineering Journal*, *251*, 207–216.

Soltani, T., & Lee, B.-K. (2016a). Sono-synthesis of nanocrystallized $BiFeO_3$/reduced graphene oxide composites for visible photocatalytic degradation improvement of bisphenol A. *Chemical Engineering Journal*, *306*, 204–213.

Soltani, T., & Lee, B. (2016b). Novel and facile synthesis of Ba-doped BiFeO 3 nanoparticles and enhancement of their magnetic and photocatalytic activities for complete degradation of benzene in aqueous solution. *Journal of Hazardous Materials*, *316*, 122–133.

Somma, I. Di. (2015). Solar photocatalysis: Materials, reactors, some commercial, and pre-industrialized applications. A comprehensive approach, *Applid Catalysis B: Environmental*, *171*, 90–123.

Song, Y., Qi, J., Tian, J., Gao, S., & Cui, F. (2018). Construction of Ag/g-C_3N_4 photocatalysts with visible-light photocatalytic activity for sulfamethoxazole degradation. *Chemical Engineering Journal*, *341*, 547–555.

Soni, S. S., & Kotadia, D. A. (2014). Time-dependent stereoselective Heck reaction using mesoporous Pd/TiO_2 nanoparticles catalyst under sunlight. *Catalysis Science & Technology*, *4*, 510–515.

Stylidi, M., Kondarides, D. I., & Verykios, X. E. (2004). Visible light-induced photocatalytic degradation of Acid Orange 7 in aqueous TiO_2 suspensions. *Applied Catalysis B: Environmental*, *47*, 189–201.

Subha, N., Mahalakshmi, M., Myilsamy, M., Reddy, N. L., Shankar, M. V, Neppolian, B., & Murugesan, V. (2017). Influence of synthesis conditions on the photocatalytic activity of mesoporous Ni doped $SrTiO_3$/TiO_2 heterostructure for H_2 production under solar light irradiation. *Colloids and Surfaces A: Physicochemical and Engineering Aspects*, *522*, 193–206.

Sun, H., Liu, S., Liu, S., & Wang, S. (2014). A comparative study of reduced graphene oxide modified TiO_2, ZnO and Ta_2O_5 in visible light photocatalytic/photochemical oxidation of methylene blue. *Applied Catalysis B, Environmental*, *146*, 162–168.

Sun, M., Bi, Y., Yan, T., Zhang, Y., Wu, T., Shao, Y., & Du, B. (2018). Room-temperature fabrication of bismuth oxybromide/oxyiodide photocatalyst and efficient degradation of phenolic pollutants under visible light. *Journal of Hazardous Materials*, *358*, 20–32.

Tahir, K., Nazir, S., Ahmad, A., Li, B., Khan, A.U., Khan, Z.U.H., Khan, F.U., Khan, Q.U., Khan, A., & Rehman, A.U., (2017). Facile and green synthesis of phytochemicals capped platinum nanoparticles and in vitro their superior antibacterial activity. *Journal of Photochemistry & Photobiology B: Biology*, *166*, 246–251.

Tan, L., Ong, W., Chai, S., & Mohamed, A. R. (2016). Photocatalytic Reduction of CO_2 with H_2O Over Graphene Oxide–Supported Oxygen–Rich TiO_2 Hybrid Photocatalyst Under Visible Light Irradiation: Process and Kinetic Studies. *Chemical Engineering Journal*, *308*, 248–255.

Tan, L., Ong, W., Chai, S., & Rahman, A. (2015). Noble metal modified reduced graphene oxide/TiO_2 ternary nanostructures for efficient visible-light-driven photoreduction of carbon dioxide into methane. *Applied Catalysis B, Environmental*, *166–167*, 251–259.

Tanaka, H., & Misono, M. (2001). Advances in designing perovskite catalysts. *Current Opinion in Solid State and Material Science*, *5*, 381–387.

Tao, J., Gong, Z., Yao, G., Cheng, Y., Zhang, M., Lv, J., & Sun, Z. (2016). Enhanced optical and photocatalytic properties of Ag quantum dots-sensitized nanostructured TiO_2/ZnO heterojunctions. *Journal of Alloys and Compounds*, *688*, 605–612.

Thrall, M., Freer, R., Martin, C., Azough, F., Patterson, B., & Cernik, R. J. (2008). An in situ study of the formation of multiferroic bismuth ferrite using high resolution synchrotron X-ray powder diffraction. *Journal of the European Ceramic Society*, *28*, 2567–2572.

Tseng, W. J., & Lin, R.-D. (2014). $BiFeO_3$/α-Fe_2O_3 core/shell composite particles for fast and selective removal of methyl orange dye in water. *Journal of Colloid and Interface Science*, *428*, 95–100.

Turki, A., Guillard, C., Dappozze, F., Ksibi, Z., Berhault, G., & Kochkar, H. (2015). Phenol photocatalytic degradation over anisotropic TiO_2 nanomaterials: Kinetic study, adsorption isotherms and formal mechanisms. *Applied Catalysis B, Environmental*, *163*, 404–414.

Vafaee, M., Olya, M. E., Drean, J., & Hekmati, A. H. (2017). Synthesize, characterization and application of ZnO/W/Ag as a new nanophotocatalyst for dye removal of textile wastewater; kinetic and economic studies. *Journal of Taiwan Institute of Chemical Engineers, 80*, 379–390.

Valencia, S., Marín, J. M., Restrepo, G., & Frimmel, F. H. (2013). Application of excitation–emission fluorescence matrices and UV/Vis absorption to monitoring the photocatalytic degradation of commercial humic acid. *Science of the Total Environment*, *442*, 207–214.

Vanga, P. R., Mangalaraja, R. V, & Ashok, M. (2015). Effect of (Nd, Ni) co-doped on the multiferroic and photocatalytic properties of $BiFeO_3$. *Materials Research Bulletin*, *72,* 299–305.

Villasenor, J., Reyes, P., & Pecchi, G. (2002). Catalytic and photocatalytic ozonation of phenol on MnO2 supported catalysts. *Catalysis Today*, *76*, 121–131.

Wang, Y., Zhang, Y., Zhu, H., Liu, J., Lian, T., & Zhang, W. (2016). Geomatry stretegy for engineering the recommbination possibility of exciton in nanowires. *Nanoscale, 8*, 7318−7325.

Wang, B., Guo, X., Jin, G., & Guo, X. (2017). Visible-light-enhanced photocatalytic Sonogashira reaction over silicon carbide supported Pd nanoparticles. *Catalysis Communications*, *98,* 81–84.

Wang, H., Wu, D., Liu, C., Guan, J., Li, J., Huo, P., Liu, X., Wang, Q., & Yan, Y. (2018). Fabrication of Ag/In_2O_3/TiO_2/HNTs hybrid-structured and plasma effect photocatalysts for enhanced charges transfer and photocatalytic activity. *Journal of Industrial and Engineering Chemistry*, *67*, 164–174.

Wang, J., Wei, Y., Zhang, J., Ji, L., Huang, Y., & Chen, Z. (2014). Synthesis of pure-phase $BiFeO_3$ nanopowder by nitric acid-assisted gel. *Materials Letters*, *124*, 242–244.

Wang, L., Niu, C.-G., Wang, Y., Wang, Y., & Zeng, G.-M. (2016). The synthesis of $Ag/AgCl/BiFeO_3$ photocatalyst with enhanced visible photocatalytic activity. *Ceramics International*, *42*, 18605–18611.

Wang, M., Ioccozia, J., Sun, Bl., Lin, C., & Lin, Z. (2014). Inorganic-Modified Semiconductor TiO_2 Nanotube Arrays for Photocatalysis. *Energy & Environmental Science*. *7*, 2182−2202.

Wang, S., Guan, Y., Wang, L., Zhao, W., He, H., Xiao, J., & Sun, C. (2015). Fabrication of a novel bifunctional material of $BiOI/Ag_3VO_4$ with high adsorption – photocatalysis for efficient treatment of dye wastewater. *Applied Catalysis B, Environmental*, *168–169*, 448–457.

Wang, W., Li, N., Chi, Y., Li, Y., Yan, W., Li, X., & Shao, C. (2013). Electrospinning of magnetical bismuth ferrite nanofibers with photocatalytic activity. *Ceramics International*, *39*, 3511–3518.

Wang, W., Tadé, M. O., & Shao, Z. (2015). Research progress of perovskite materials in photocatalysis-and photovoltaics-related energy conversion and environmental treatment. *Chemical Society Reviews*, *44*, 5371–5408.

Wang, W., Zhou, Y., Ni, Y., Lu, C., & Xu, Z. (2015). Superiority and mechanism of Pt oriented-deposition in improving the photocatalytic activity of TiO_2 sphere with exposed {0 0 1} facet. *Materials Letters*, *145*, 180–183.

Wang, X., Mao, W., Zhang, J., Han, Y., Quan, C., Zhang, Q., & Huang, W. (2015). Facile fabrication of highly efficient g-C_3N_4/$BiFeO_3$ nanocomposites with enhanced visible light photocatalytic activities. *Journal of Colloid and Interface Science*, *448*, 17–23.

Wang, T., Zhao, H.P., Wang, H., Liu, B.T., Li, C.Q., (2016). Research on degradation product and reaction kinetics of membrane electro-bioreactor (MEBR) with catalytic electrodes for high concentration phenol wastewater treatment, *Chemosphere, 155,* 94–99.

Wei, J., Zhang, C., & Xu, Z. (2012). Low-temperature hydrothermal synthesis of $BiFeO_3$ microcrystals and their visible-light photocatalytic activity. *Materials Research Bulletin*, *47,* 3513–3517.

Wen, X., Niu, C., Zhang, L., Liang, C., Guo, H., & Zeng, G. (2018). Photocatalytic degradation of ciprofloxacin by a novel Z-scheme CeO_2–Ag/AgBr photocatalyst: Influencing factors, possible degradation pathways, and mechanism insight. *Journal of Catalysis*, *358*, 141–154.

Wenderich, K., & Mul, G. (2017). Methods, Mechanism, and Applications of Photodeposition in Photocatalysis: A Review. *Chemical Reviews, 116,* 14587–14619.

Wu, Y., Fang, Z., Shi, Y., Chen, H., Liu, Y., & Wang, Y. (2019). Activation of peroxymonosulfate by BiOCl@Fe_3O_4 catalyst for the degradation of atenolol: Kinetics, parameters, products and mechanism. *Chemosphere*, *216*, 248–257.

Xian, T., Yang, H., Dai, J. F., Wei, Z. Q., Ma, J. Y., & Feng, W. J. (2011). Photocatalytic properties of $BiFeO_3$ nanoparticles with different sizes. *Materials Letters*, *65*, 1573–1575.

Xiao, Y., Song, X., Liu, Z., Li, R., & Zhao, X. (2017). Photocatalytic removal of cefazolin using Ag_3PO_4/BiOBr under visible light and optimization of parameters by response surface methodology. *Journal of Industrial and Engineering Chemistry*, *45*, 248–256.

Xu, M., Han, L., & Dong, S. (2013). Facile Fabrication of Highly Efficient g-C_3N_4/Ag_2O Heterostructured Photocatalysts with Enhanced Visible-Light Photocatalytic Activity. *ACS Applied Materials & Interfaces*, *5*, 12533–12540.

Xu, X., Lin, Y., Li, P., Shu, L., & Nan, C. (2011). Synthesis and Photocatalytic Behaviors of High Surface Area $BiFeO_3$ Thin Films, *Journal of the American Ceramic Society*, *94*, 2296–2299.

Xue, Q., Liu, Y., Zhou, Q., Utsumi, M., Zhang, Z., & Sugiura, N. (2016). Photocatalytic degradation of geosmin by Pd nanoparticle modified WO_3 catalyst under simulated solar light. *Chemical Engineering Journal*, *283*, 614–621.

Yan, H., Deng, H., Ding, N., He, J., Peng, L., Sun, L., Yang, P., & Chu, J. (2013). Influence of transition elements doping on structural, optical and magnetic properties of $BiFeO_3$ films fabricated by magnetron sputtering. *Materials Letters*, *111*, 123–125.

Yang, Lei, Xu, L., Bai, X., & Jin, P. (2019). Enhanced visible-light activation of persulfate by Ti^{3+} self-doped TiO_2/graphene nanocomposite for the rapid and efficient degradation of micropollutants in water. *Journal of Hazardous Materials*, *365*, 107–117.

Yang, Liping, & Liu, Z. (2007). Study on light intensity in the process of photocatalytic degradation of indoor gaseous formaldehyde for saving energy. *Energy Conversion and Managment*, *48*, 882–889.

Yang, X., Ke, X., Yang, D.J., Liu, J.W., Guo, C., Frost, R., Su, H.Q., Zhu, H.Y., (2010). Effect of ethanol washing of titania clay mineral composites on photocatalysis for phenol decomposition, *Applied Clay Science, 49,* 44–50.

Yamashita, T., Hayes, P., (2008). Analysis of XPS spectra of Fe^{2+} and Fe^{3+} ions in oxide materials, *Applied Surface Science, 254,* 2441–2449.

Yang, X., Zhang, Y., Xu, G., Wei, X., Ren, Z., Shen, G., & Han, G. (2013). Phase and morphology evolution of bismuth ferrites via hydrothermal reaction route. *Materials Research Bulletin*, *48*, 1694–1699.

Ye, J., Li, X., Hong, J., Chen, J., & Fan, Q. (2015). Photocatalytic degradation of phenol over ZnO nanosheets immobilized on montmorillonite. *Materials Science in Semiconductor Processing*, *39*, 17–22.

Yin, J., Liao, G., Zhou, J., Huang, C., Ling, Y., Lu, P., & Li, L. (2016). High performance of magnetic $BiFeO_3$ nanoparticle-mediated photocatalytic ozonation for wastewater decontamination. *Separation and Purification Technology*, *168*, 134–140.

Yu, Q., Fang, S., & Wang, X. (2017). The g-C_3N_4 Nanosheets Separated by PS for Photocatalytic Degradation of Dye. *Journal of Nano Research*, *49*, 215–224.

Yusoff, N., Ong, S., Ho, L., Wong, Y., & Khalik, W. (2015). Degradation of phenol through solar-photocatalytic treatment by zinc oxide in aqueous solution. *Desalination and Water Treatment*, *54*, 1621–1628.

Zaki, M. I., Ramadan, W., Katrib, A., & Rabee, A. I. M. (2014). Surface chemical and photocatalytic consequences of Ca-doping of $BiFeO_3$ as probed by XPS and H_2O_2 decomposition studies. *Applied Surface Science*, *317*, 929–934.

Zavaliche, F., Yang, S. Y., Zhao, T., Chu, Y. H., Cruz, M. P., Eom, C. B., & Ramesh, R. (2007). Multiferroic $BiFeO_3$ films: domain structure and polarization dynamics. *Phase Transitions: A Mutinational Journal*, *77*, 37–41.

Zhang, G., Song, A., Duan, Y., & Zheng, S. (2018). Enhanced photocatalytic activity of TiO_2/zeolite composite for abatement of pollutants. *Microporous and Mesoporous Materials*, *255*, 61–68.

Zhang, Jingtao, Suo, X., Liu, X., Liu, B., Xue, Y., Mu, L., & Shi, H. (2016). PdO loaded WO_3 composite with $Na_2W_4O_{13}$ flake: A 2-D heterostructure composite material. *Materials Letters*, *184*, 25–28.

Zhang, Jingtao, Suo, X., Zhang, J., Han, B., Li, P., Xue, Y., & Shi, H. (2016). One-pot synthesis of Au/TiO_2 heteronanostructure composites with SPR effect and its antibacterial activity. *Materials Letters*, *162*, 235–237.

Zhang, Jun, Gondal, M. a., Wei, W., Zhang, T., Xu, Q., & Shen, K. (2012). Preparation of room temperature ferromagnetic $BiFeO_3$ and its application as an highly efficient magnetic separable adsorbent for removal of Rhodamine B from aqueous solution. *Journal of Alloys and Compounds*, *530*, 107–110.

Zhang, Y.F., Selvaraj, R., Sillanpaa, M., Kim, Y., Tai, C.W., (2014). The influence of operating parameters on heterogeneous photocatalytic mineralization of phenol over $BiPO_4$, *Chemical Engineering Journal, 245, 117–123.*

Zhang, H., L.H. Guo, L.H., Zhao, L.X., Wan, B., Yang, H., (2015). Switching oxygen reduction pathway by exfoliating graphitic carbon nitride for enhanced photocatalytic phenol degradation, *Journal of Physical and Chemical Letters*, *6,* 958–963.

Zhang, Lihong, Li, P., Gong, Z., & Li, X. (2008). Photocatalytic degradation of polycyclic aromatic hydrocarbons on soil surfaces using TiO_2 under UV light. *Journal of Hazardous Materials*, *158,* 478–484.

Zhang, Linlin, Zhu, D., He, H., Wang, Q., Xing, L., & Xue, X. (2017). Enhanced piezo/solar-photocatalytic activity of Ag/ZnO nanotetrapods arising from the coupling of surface plasmon resonance and piezophototronic effect. *Journal of Physical and Chemistry of Solids*, *102,* 27–33.

Zhang, Q., Tengb, J., Zoua, G., Peng, Q., Dub, Q., Jiao, T., & Xianga, J. (2016). Efficient Phosphate sequestration for water purification by Unique Sandwichlike MXene/Magnetic Iron Oxide Nanocomposites. *Nanoscale*, *8*, 7085–7093.

Zhang, W., Jia, B., Wang, Q., & Dionysiou, D. (2015). Visible-light sensitization of TiO_2 photocatalysts via wet chemical N-doping for the degradation of dissolved organic compounds in wastewater treatment: a review. *Journal of Nanoparticle Research*, *17*, 221-239.

Zhang, X., Wang, B., Wang, X., Xiao, X., Dai, Z., Wu, W., Zheng, J., Ren, F., & Jiang, C. (2015). Preparation of M@ $BiFeO_3$ Nanocomposites (M= Ag, Au) Bowl Arrays with Enhanced Visible Light Photocatalytic Activity. *Journal of the American Ceramic Society*, *98*, 2255–2263.

Zhang, Yuchi, Xing, Z., Zou, J., Li, Z., Wu, X., & Shen, L. (2017). 3D urchin-like black TiO_{2-x}/carbon nanotube heterostructures as efficient visible-light-driven photocatalysts. *RCS Advances*, *7*, 453–460.

Zhang, Yunfan, Selvaraj, R., Sillanpaa, M., Kim, Y., & Tai, C. (2014). The influence of operating parameters on heterogeneous photocatalytic mineralization of phenol over $BiPO_4$. *Chemical Engineering Journal*, *245*, 117–123.

Zhao, M., Zhu, Y., Zhang, Y., Zhang, T., Qiu, D., Lia, G., Hu, C., Wang, Q., Zhang, F., & Li, M. (2017). Resistive switching and related magnetization switching in Pt/$BiFeO_3$/Nb:$SrTiO_3$ heterostructures. *RCS Advances*, *7*, 23287–23292.

Zhao, Q., Li, X., Liu, Y., & Zhu, A. (2015). Visible-light driven generation of reactive radicals over $BiFeO_3$/TiO_2/nanotube array: experimental evidence and energetic mechanism. *Journal of Nanoparticle Research*, *17*, 1–9.

Zheng, F., Cui, B., Wu, X., Meng, G., Liu, H., & Si, J. (2016). Immobilization of laccase onto chitosan beads to enhance its capability to degrade synthetic dyes. *International Biodeterioration & Biodegradation*, *110,* 69–78.

Zhou, N., Puente, V.L., Wang, Q., Polaverapu, L., & Xu, Q.H., (2015). Plasmonic-enhanced light harvesting: applicationsin enhanced photocatalysis, photodynamic therapy, and photovoltics. *RCS Advances, 5*, 29076–29097.

Zhou, Z., Chen, L., Wang, Z., Guo, L., Huang, Z., & Cen, K. (2017). Experimental and modeling investigation of oxy-coal combustion based on Langmuir-Hinshelwood kinetics and direct calculation of char morphology. *Fuel*, *208*, 702–713.

Zhu, H., Kang, L., Liu, M., & Ouyang, J. (2016). Single-crystal oxide substrate dependent electrical properties of sputtered $BiFeO_3$ thin films. *Materials Letters*, *174*, 57–60.

Zou, J., Jiang, J., Zhang, Y., Ma, J., & Wan, Q. (2012). A comparative study of the optical, magnetic and electrocatalytic properties of nano $BiFeO_3$ with different morphologies. *Materials Letters, 72,* 134–136.

Zuniga-benitez, H., & Penuela, G. A. (2016). Methylparaben removal using heterogeneous photocatalysis: effect of operational parameters and mineralization/biodegradability studies. *Environmental Science and Pollution Research, 24,* 6022–6030.

Zuo, F., Wang, L., & Feng, P. (2013). Self-doped Ti 3D@TiO_2 visible light photocatalyst: Influence of synthetic parameters on the H_2 production activity. *International Journal of Hydrogen Energy*, *39*, 711–717.

APPENDIX

APPENDIX A-1

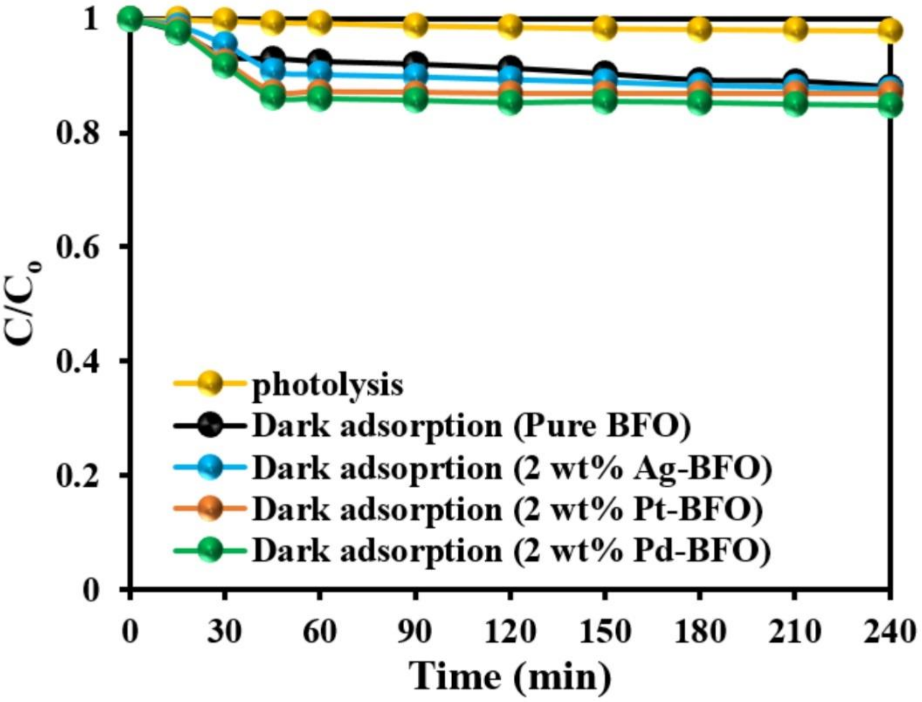

Figure A-1: Dark adsorptions and photolysis of MG dye using pure BFO and 2 wt% NM-BFO nanocomposites ([MG] = 10.0 mg/L; catalyst loading = 1.0 g/L; solution pH = 5.45).

LIST OF PUBLICATIONS

JOURNALS

Jaffari, Z. H., Lam, S. M., Sin, J. C., Zeng, H., & Mohamed, A.R. (2019). Magnetically recoverable Pd-loaded $BiFeO_3$ nanocomposite with enhanced visible light photocatalytic performance for pollutant, bacterial and fungal elimination. *Separation and Purification Technology*, https://doi.org/10.1016/j.seppur.2019.116195.

Jaffari, Z. H., Lam, S. M., Sin, J. C., & Mohamed, A. R. (2019). Constructing magnetic Pt-loaded $BiFeO_3$ nanocomposite for boosted visible light photocatalytic and antibacterial activities. *Environmental Science and Pollution Research, 26*, 10204–10218.

Jaffari, Z. H., Lam, S., Sin, J., & Zeng, H. (2019). Boosting visible light photocatalytic and antibacterial performance by decoration of silver on magnetic spindle-like bismuth ferrite. *Materials Science in Semiconductor Processing, 101*, 103–115.

Lam, S.M., Jaffari, Z.H., & Sin, J.C. (2018). Hydrothermal synthesis of coral-like Palladium-doped $BiFeO_3$ nanocomposites with enhanced photocatalytic and magnetic properties, *Materials Letters, 224*, 1−4.

BOOK CHAPTER

Lam, S.M., Kee, M.W., Wong, K.A., Jaffari, Z.H., Chai, H.Y., Sin, J.C., A Newly Emerging MXene Nanomaterial for Environmental Application, *MXene: Foundation and Applications, 51*, 20−60.

CONFRENCE PROCEDINGS

Jaffari, Z. H., Lam, S. M., & Sin, J. C. (2019). Photocatalytic degradation of organic pollutants using magnetic Pd-doped $BiFeO_3$ nanocomposites under visible light irradiation, *AIP Confrence Procedings*, 2157, 020041. (ISGST-2019)

Lam, S.M., Jaffari, Z. H., Sin, J. C., & Mohamed, A. R. (2018). Sindly $BiFeO_3$ nanoparticles for photodegradation of organic pollutants under a compact fluorescent lamp, *IOP Confrence series: Earth and Environmental Secience, 151*, 012021. (ICEST-2018)